INVESTIGATION OF ELECTRODE SURFACES IN SOLID OXIDE FUEL CELLS USING RAMAN MAPPING AND ENHANCED SPECTROSCOPY TECHNIQUES

A Dissertation
Presented to
The Academic Faculty

By

Kevin Blinn

In Partial Fulfillment
Of the Requirements for the Degree
Doctor of Philosophy in Materials Science and Engineering

Georgia Institute of Technology

December 2012

INVESTIGATION OF ELECTRODE SURFACES IN SOLID OXIDE FUEL CELLS USING RAMAN MAPPING AND ENHANCED SPECTROSCOPY TECHNIQUES

Approved by:

Dr. Meilin Liu, Advisor
School of Materials Science & Engineering
Georgia Institute of Technology

Dr. Kenneth H. Sandhage
School of Materials Science & Engineering
Georgia Institute of Technology

Dr. Preet Singh
School of Materials Science & Engineering
Georgia Institute of Technology

Dr. Gleb Yushin
School of Materials Science & Engineering
Georgia Institute of Technology

Dr. Lawrence A. Bottomley
School of Chemistry and Biochemistry
Georgia Institute of Technology

Date Approved: November 6, 2012

There are relatively few experiments in atomic physics these days that don’t involve the use of a laser.

--Eric Allin Cornell, Nobel Laureate physicist

ACKNOWLEDGMENTS

First and foremost, I would like to thank my parents. They provided me with a loving environment in which to grow up and the constant encouragement and support I needed to take on challenges. Without the hard work and sacrifice they put in to raising me, I would not have possessed the “right stuff” to even begin this particular journey. I am forever in their debt.

Next, I give special thanks to my advisor, Dr. Meilin Liu, for the encouragement, guidance, and overall support he generously gave me during my doctoral study. His thoughtful suggestions and unyielding patience contributed largely to the success of this work. I would also like to thank the rest of my Ph. D thesis committee, Dr. Larry Bottomley, Dr. Kenneth Sandhage, Dr. Preet Singh, and Dr. Gleb Yushin, for their suggestions as well as their valuable time put into reviewing my dissertation.

A considerable portion of the work supporting my thesis would not have been possible without excellent suggestions and help from my colleagues, past and present: Dr. Harry Abernathy, Xiaxi Li, Dr. Mingfei Liu, Dr. Lei Yang, Dr. Jung-Pil Lee, Dr. Wentao Qin, Dr. Yingcui Fang, and Dr. Yongman Choi deserve my utmost thanks. I would also like to mention past and present lab mates who also provided invaluable friendship and perspective over the course of this journey: Dr. Matt Lynch, Samson Lai, Dr. Dong Ding, Dr. Min-Kyu Song, Ben Rainwater, Gordon Waller, and Cynthia Cromer. I also wish to acknowledge my NASA advisor, Dr. Serene Farmer, as well as John Setlock and Diana Santiago-DeJesus, for their great help during my time at NASA Glenn Research Center.

My deepest gratitude goes to my wife Katherine. She has been with me since nearly the beginning of my Ph. D. journey, and since then, she has given me the love and support I needed to stay with it until the end. She has the patience of a saint. I would also like to thank her parents, Trent and Debbie, for their support and treating me like one of their own. Finally, I would be remiss if I did not mention “the boys,” Leo and Sebastian, for their furry companionship, particularly during the preparation of this document.

This work was supported in part by the HeteroFoaM Center, an Energy Frontier Research Center funded by the U.S. Department of Energy Office of Basic Energy Sciences, under Award Number DE-SC00001061, and by the NASA Graduate Student Researchers Program under Grant Number NNX10AL43H.

TABLE OF CONTENTS

LIST OF TABLES

LIST OF FIGURES

NOMENCLATURE

Symbols

A	Active cell area
A_g	Symmetrical singly degenerate vibrational mode
B_g	Less symmetrical singly degenerate vibrational mode
E_N	Nernst potential
$E_j(\upsilon)$	Electric field as a function of frequency
E_{2g}	Doubly degenerate vibrational mode
F	Faraday's constant
F_{2g}	Triply degenerate vibrational mode
G	Enhancement factor
ΔG^o	Standard Gibbs free energy
I	Current
j	Current density
n	Number of electrons required in oxidation of a fuel molecule
U_{fuel}	Fuel utilization
z	Number of electrons involved in reaction
Z	Impedance
$\boldsymbol{\alpha_{ij}}$	Polarizability tensor
β	Charge transfer coefficient
η	Overpotential
λ	Wavelength
μ_i	Induced dipole
υ	Frequency
ω	Angular frequency
cm^{-1} (or Δcm^{-1})	Wavenumber of Raman shift

Acronyms and Abbreviations

AFM	Atomic force microscopy
BSC	Bi-electrode supported cell
3Ba-4Yb	Mixed barium and ytterbium oxides
BZCYYb	Barium zirconium cerium yttrium ytterbium oxide
BZY	Yttrium-doped barium zirconate
BZYb	Ytterbium-doped barium zirconate
DC	Direct current
DFT	Density functional theory
GDC	Gadolinium-doped ceria
IR	Infra red
LSC	Lanthanum strontium cobalt oxide
LSCF	Lanthanum strontium cobalt iron oxide
LSM	Lanthanum strontium manganese oxide
SEM	Scanning electron microscopy
SERS	Surface enhanced Raman scattering (or spectroscopy)
SHINERS	Shell-isolated nanoparticle-enhanced Raman spectroscopy
SDC	Samarium-doped ceria
SOFC	Solid oxide fuel cell
SSC	Samarium strontium cobalt oxide
SSR	Solid state reaction
TPB	Triple phase boundary
TEM	Transmission electron microscopy
UAV	Unmanned air vehicle
XRD	X-ray diffractometry
YSZ	Yttria-stabilized zirconia

SUMMARY

Solid oxide fuel cells (SOFCs) potentially represent a cleaner and more efficient method for harnessing fossil fuel energy than conventional combustion. Unfortunately, the challenge with making SOFCs mainstream lies in reducing operating costs, increasing performance, and staving off their rapid degradation. High cathode polarization remains a bottleneck for lowering operation temperature. On the anode side, supplying SOFCs with hydrocarbon-based fuels poses many problems for systems using state-of-the-art material specifications such as composites of Ni and yttria-stabilized zirconia (YSZ).

Various novel materials and surface modifications have been found to mitigate degradation issues in particular, but more information towards a more profound understanding the role of these materials in the coking and sulfur tolerance of SOFC anodes is one major scientific objective within the field. In this work, advanced Raman spectroscopic techniques were applied In order to support this objective. Raman spectroscopy was used for the tracking of the evolution of water, carbon, sulfur, and oxygen species as well as new phases at SOFC electrode surfaces following or during exposure to various temperatures, fuel gases, and electrochemical stimuli. Specifically, water and OH groups were successfully detected on Ba-containing oxides under different temperature and electrochemical conditions, carbon deposition on Ni anodes was mapped and monitored in real time, and mapping was used to support a surface-based hypothesis about sulfur poisoning. This information, coupled with performance data and other characterizations, would help to clarify the mechanisms of anode contamination reactions. Knowledge gained from this work would also help to connect electrode

modifications with performance enhancement and poisoning tolerance, offering insights vital to design of better electrodes.

In addition, lack of adequate signal from certain species, which is one of Raman spectroscopy's limitations, was addressed in the course of this work. Surface enhanced Raman scattering (SERS) techniques were used in both *in situ* and *ex situ* analyses to increase signal yield from gas species and phases that are found only in trace amounts on electrode surfaces. Sputtered silver nano-islands and $Ag@SiO_2$ core-shell nanoparticles were applied in order to achieve the signal enhancement. Using these treatments, direct detection of adsorbed oxygen species at the cathode and adsorbed hydrocarbons at the anode was made possible.

Finally, a more practical thrust of this work was the application of this study methodology and the knowledge gained from it to cells with NASA's bi-electrode supported cell (BSC) architecture. Particularly, the BSC architecture offered a convenient platform for studying state-of-the-art anode modification since the electrodes were applied by infiltration of porous scaffolds, and the composition of the anodes could be easily changed. These types of cells also offer great prospects for superior specific power density due to their low weight. Ultimately, the goal of this thrust was progress towards achieving optimum performance of SOFCs operating under jet fuel. Towards this end, a cell with a modified Ni-YSZ anode was successfully operated in a 70% CH_4 / 30 % H_2 / 30 ppm H_2S with reduced sulfur poisoning and relative stability. This anode modification also allowed for peak H_2 and CH_4 fuel utilizations of ~81% and ~34%, respectively.

CHAPTER 1: INTRODUCTION

1.1 Research Motivation

Fossil fuels comprise the most utilized type of resource in producing the world's electricity. Fuels such as coal, natural gas, and oil are currently used to generate electrical energy through combustion methods. These processes take the chemical energy of coal and convert it to thermal energy, which is in turn converted into mechanical energy in order to finally generate electrical energy. The "wheel-to-well" efficiency of this series of energy transformation processes is heavily limited. The lost efficiency from this series of energy transformations eventually leads to a quicker depletion of these scarce resources, and nature does not replace these fuels quickly enough. This ever-increasing scarcity of the world's natural fuel resources is quite evident with the rising trend in prices for natural gas, petroleum, and coal. This rising trend is illustrated below in Figure 1.1, which shows the prices for several types of energy from 1970-2009.[1] It should be noted that the economic recession likely accounts for the price decreases seen between 2007 and 2009. One other reason that fossil fuel combustion may not necessarily be a sustainable source of energy is that it is generally not a "clean" type of process. Byproducts, which include CO_2, NO_x, and SO_x, are potentially damaging to the environment due to the pollution they cause.

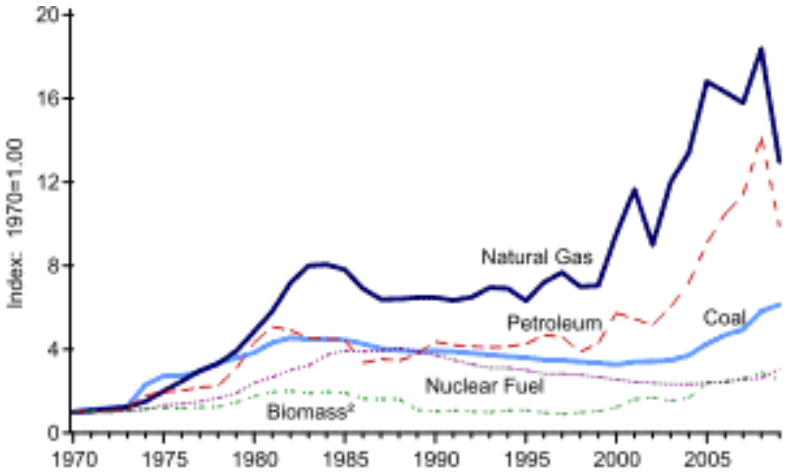

Figure 1.1. Indexed prices by energy type between the 1970 and 2009. Reproduced from the 2010 U.S. DOE Annual Energy Review.[1]

Despite the lack of sustainability in the fossil fuel energy paradigm, the fact remains that fossil fuels are a favored source of electricity, particularly in the United States. As Figure 1.2 shows, natural gas and coal accounted for well over two-thirds of electricity generation for all economic sectors of the United States in 2010.[1] It may be several decades before the technologies of alternative energy sources (e.g. nuclear, solar, wind) have advanced enough to gain traction within the economy and the proper infrastructures are in place to best utilize these sources. Therefore, a more efficient way of using the current preferred sources of energy should be found in order to maintain the standard of living to which the population is accustomed while slowing down the consumption of scarce resources. Solid oxide fuel cells (SOFCs) provide a viable alternative in this regard.

Unfortunately, at this stage, SOFC technology has its own problems that still require solving before it can attain commercial viability. Addressing these issues requires

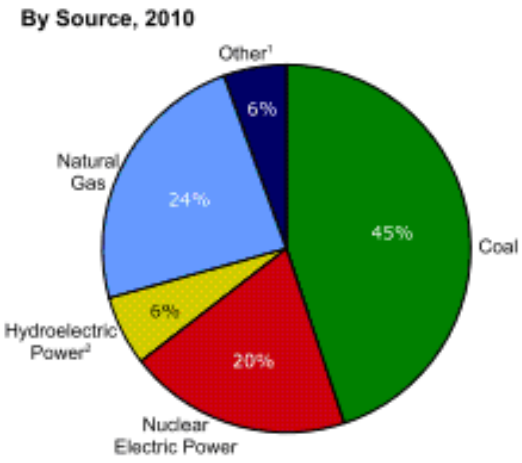

Figure 1.2. Contributions to electricity production for all economic sectors of the U.S. by different fuel sources. Reproduced from the 2010 U.S. DOE Annual Energy Review.[1]

access to fundamental chemical information that is not available through the conventional electrochemical methods used to characterize SOFCs. Therefore, other approaches to studying SOFC are warranted; one such approach is Raman spectroscopy.

1.2. Research objectives

The work presented in this dissertation involves the development of Raman spectroscopy as a tool to study the various reaction mechanisms and behavior of state-of-the-art SOFC electrodes and use the information gained to improve electrodes. Specifically, the objectives of the research are:

1) Development and utilization of an experimental setup that allows improved *in situ* Raman spectroscopic mapping and monitoring of the surface of SOFC electrodes
2) Knowledge of where and how carbon and sulfur deposit on SOFC anodes during coking and sulfur poisoning types of degradation

3) Understanding of the role that water plays in coking and sulfur poisoning tolerance of anodes that incorporate Ba-containing oxides
4) Improvement of Raman signal from surface species relevant to cathode and anode reactions through surface enhanced Raman scattering (SERS) methods
5) Implementation of the knowledge gained from previous study towards improving the coking and sulfur poisoning tolerance of a Ni-YSZ anode

Meeting the objectives outlined above would hopefully offer insights towards a more rational design of SOFC electrodes by suitable material selection and optimization of operating conditions. This type of fundamental information would be a valuable contribution to the field and certainly help drive SOFC towards mainstream commercialization. In addition, the research presented herein might demonstrate potential test platforms for characterizing catalysis and transformation processes in other energy storage and conversion systems such as Li-ion batteries and pseudocapacitors.

1.3. Dissertation structure

The first part of Chapter 2 provides fundamental background information on solid oxide fuel cells, including how they function as well as some of their common constituent materials and configurations. It also focuses on the performance and degradation issues surrounding SOFC electrodes. The latter part of Chapter 2 presents an overview of Raman spectroscopy, its underlying physics, and how the technique can be applied toward SOFC systems.

Chapter 3 outlines all of the technical approaches used in the current work. This information consists of the Raman experimental setup, sample fabrication details, electrochemical testing details, and other characterizations used to validate the findings from the research.

Chapter 4 discusses the characterization of Ba-containing oxides by both *ex situ* and *in situ* Raman spectroscopy that is used in order to gain insights into the connection between the materials' water uptake properties and the degradation tolerance enhancement that they grant to SOFC anodes.

Chapter 5 details Raman monitoring and mapping experiments used to characterize coking and sulfur poisoning on geometrically-defined Ni-YSZ anodes.

Chapter 6 explores methodologies for applying surface-enhanced Raman scattering (SERS) to Raman studies of electrodes in order to boost signal from elusive surface species such as adsorbed oxygen at the cathode and adsorbed hydrocarbons at the anode.

Chapter 7 demonstrates the implementation of oxide modifications to Ni-YSZ anodes with a novel structure. Results from electrochemical testing and Raman spectroscopy are coupled and used in conjunction with other characterization methods to gain a complete picture of the effectiveness of these modifications.

Finally, Chapter 8 lists the conclusions garnered from this research and suggests possible future directions for gaining even deeper understanding of SOFC electrodes as well as other energy-related materials systems using the Raman spectroscopy-based techniques outlined in this dissertation.

CHAPTER 2: BACKGROUND

2.1. Fundamentals of solid oxide fuel cells (SOFCs)

Fuel cells directly convert chemical energy of fuels into electrical energy by electrochemical reactions between fuel and oxidant gases. These reactions result in high fuel-to-electricity efficiencies upwards of 60%, and they produce much cleaner emissions than combustion, making fuel cells much more environmentally friendly[2-4]. Solid oxide fuel cells (SOFCs), in particular, have versatile energy applications. Their high operating temperatures convey numerous advantages, such as low internal resistance and usable exhaust heat for driving secondary energy generation systems. SOFCs also allow for the use of cheaper catalysts than other types of fuel cells, and more importantly, they have the flexibility to directly utilize carbonaceous fuels such as CO, coal syngas, alkane gases (e.g. CH_4 and C_3H_8), and renewable biofuels.[2, 5-11] With increasing amounts of research into SOFC technology, this alternative energy source grows ever closer to becoming a mainstream route for stationary power generation.

A solid oxide fuel cell provides a direct current, and therefore electrical energy, to an external load by two sets of electrochemical reactions working in concert with one another. In the typical hydrogen fuel cell, hydrogen fuel is fed to the porous anode, which catalyzes the fuel's reaction with oxygen anions conducted to it by the thin electrolyte. The reaction produces water and electrons; this can be summarized by the following equation:

$$H_2 + O^{2-} \rightarrow 2e^- + H_2O \qquad (2\text{-}1)$$

These electrons are conducted through an external load by a current collector, which is a role that is filled by the interconnect in a planar cell like the one in Figure 1.3.

Meanwhile, on the cathode side of the cell, oxygen in the air is adsorbed, after which it is reduced to an ionic state by the flowing electrons in the current from the anode side with the help of the catalytic cathode material, as shown in this equation:

$$\frac{1}{2}O_2 + 2e^- \rightarrow O^{2-} \tag{2-2}$$

The resulting oxygen anion is then conducted through the electrolyte to complete the cycle. The total cell reaction can thus be treated simply as the formation of water where 4 electrons are transferred when whole fuel and oxidant molecules are considered, as in this equation:

$$2H_2 + O_2 \rightarrow 2H_2O \tag{2-3}$$

When no current is flowing through the cell, or when the cell is in thermodynamic equilibrium, the theoretical potential across the cell is determined by the following equation:

$$E_N = \frac{RT}{4F} \ln \frac{P_{O2,cathode}}{P_{O2,anode}} \tag{2-4}$$

This equation is known as the Nernst equation, where E_N is the theoretical Nernst potential, R is the gas constant (8.314 kJ / K*mol), T is the temperature of the system in K, F is Faraday's constant (~96,500 C / mol), and P_{O2} is the partial pressure of oxygen at each cell electrode environment. The factor of 4 in the denominator represents the transfer of 4 electrons. A typical cathode environment for a cell is air, so a typical $P_{O2,cathode}$ is fixed at 0.21 atm, while $P_{O2,anode}$ is itself determined by the composition of the fuel gas and the thermodynamic equilibrium between the fuel's constituents.

Therefore, for a fuel composed of humidified H_2, $P_{O2,anode}$ would be determined by the following equation:

$$P_{O2,anode} = \left(\frac{P_{H2O}}{P_{H2}} \right)^2 \exp\left(\frac{\Delta G^\circ}{RT} \right) \tag{2-5}$$

P_{H2O} and P_{H2} are the respective partial pressures of H_2O and H_2 in the anode environment, while ΔG^o is the standard Gibbs free energy change for the reaction in Equation (1-3). The value of ΔG^o is a function of temperature.

By combining (1-4) with (1-5), cancelling the exponential, and rearranging the terms, the Nernst equation can be written as:

$$E_N = \frac{-\Delta G^\circ}{4F} + \frac{RT}{4F} \ln \frac{P_{O2,cathode} P_{H2}^2}{P_{H2O}^2} \tag{2-6}$$

As an example, a cell held at 800°C (1073 K) with air as the oxidant and a fuel composition of 97% H_2 and 3% H_2O would have a theoretical E_N of 1.11 V, since ΔG^o is about -380 kJ / mol at that temperature. The actual observed open circuit voltage (OCV) of the cell would end up being slightly lower than that value. Some reasons for that might include local variations in gas partial pressures and leaks in the cell system.

As demonstrated above, water is the sole "waste" product of fuel cells running on H_2, making them a relatively clean energy option. In addition, the water, in the form of steam, could potentially be used to drive a secondary power generation mechanism to aid in the recovery of lost energy from heating, increasing the overall system efficiency. On the other hand, use of CO and hydrocarbon-containing fuels produces carbon dioxide as exhaust on the anode side, albeit in a cleaner manner than combustion.

Figure 1.3 below shows an example of a typical single anode-supported SOFC. A typical SOFC system might be composed of a La-containing perovskite cathode (e.g.

$La_{0.85}Sr_{0.15}MnO_{3-\delta}$ or $La_{0.6}Sr_{0.4}Co_{0.2}Fe_{0.8}O_{3-\delta}$), an yttria-stabilized zirconia (YSZ) electrolyte, a Ni-YSZ cermet anode, and chromite ceramic interconnect materials. The system might also include other "balance-of-plant" materials such as fuel reformers.[12] This fuel cell would operate successfully at temperatures between 800°C and 1000°C. One of the main technical challenges in the SOFC field is the reduction of the fuel cell's operating temperature. Reducing the SOFC operating temperature to more intermediate values below 700°C would impart advantages such as lower degradation of electrodes and decreased thermal stresses at component interfaces. Lowering the SOFC's operating temperature, however, decreases its conductivity and catalytic activity, resulting in cell voltage losses.

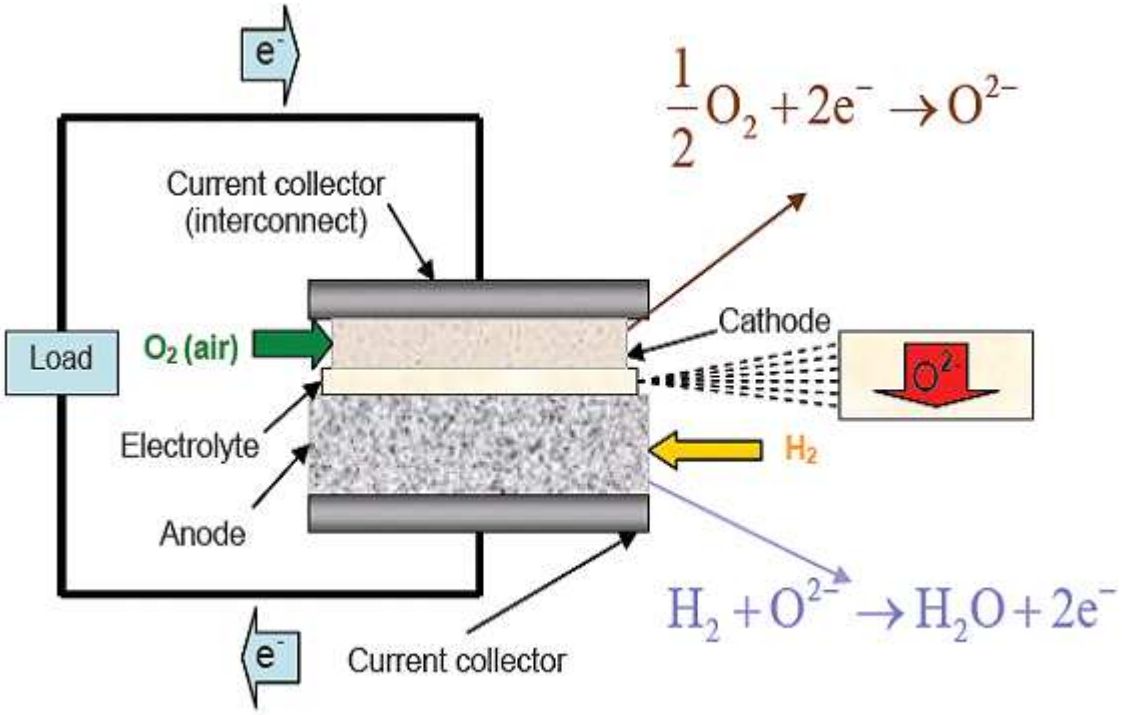

Figure 2.1. Schematic of a typical working anode-supported SOFC and the electrochemical equations associated with operation. The electrode materials are porous as to allow gases to flow through them.

2.2. Performance limitations in SOFCs

The two major factors that cause voltage loss in SOFCs are electrolyte bulk resistance and polarization resistance at the electrode-electrolyte interfaces. The contribution of the bulk resistance, which encompasses the ionic resistance of the electrolyte and the electronic resistance of the electrodes, can be simply calculated by Ohm's law:

$$\eta_{Bulk} = IR_{Bulk} \tag{2-7}$$

where I is the current passing through the cell, R_{bulk} is the bulk (or Ohmic) resistance, and η_{Bulk} is the resulting voltage loss. Electrolyte materials with higher conductivity coupled with thinner electrolyte layers have already been used to lower electrolyte bulk resistance in so-called intermediate-temperature SOFCs.[13, 14] The true bottlenecks in development of SOFC technology involve electrode materials and microstructures.[2] These aspects contribute more to polarization, which is the second major type of voltage loss and a more complex problem to approach.

Polarization can be roughly divided into two categories, which are known as charge transfer and mass transfer. Charge transfer polarization involves the extra potential (i.e. "overpotential") required to overcome the activation energy barrier that impedes a reaction within the cell from proceeding at a particular rate. This overpotential results in an equivalent voltage loss for the cell. In an electrochemical reaction, the produced current is the indicator of reaction rate. Hence, this type of polarization mainly dominates when the cell is operating at low current. The relation between charge transfer loss and current density is given by the Butler-Volmer equation[12]:

$$j = j_0\left[\exp\left(\frac{\beta F\eta_{ct}}{RT}\right) - \exp\left(-\frac{(1-\beta)F\eta_{ct}}{RT}\right)\right] \tag{2-8}$$

where η_{ct} represents the overpotential, β is the dimensionless charge transfer coefficient, j is the cell's current density (i.e. current per electrode area), and j_0 is the exchange current density. When charge transfer loss is prominent in a cell, the exhibited behavior in the cell might be called "activation polarization."

Mass transfer polarization, on the other hand, becomes evident when the kinetics of the transport of reactants to reaction sites and products away from reaction sites limit the electrochemical reaction. At a sufficiently high current, the mass transfer overpotential can be thus approximated:

$$\eta_{mt} = \frac{RT}{zF}\ln\left(1 - \frac{j}{j_L}\right) \tag{2-9}$$

where z is the number of electrons involved in the cell reaction and j_L is the limiting current density, or the current at which the mass transfer overpotential approaches infinity and cell voltage effectively drops to zero.

2.3. Common ways to test SOFCs

Linear voltammetry is the most basic way to test a fuel cell's performance. The top plot in Figure 1.4 provides a picture of how a typical voltage-current (I-V) relationship plot from this test might look. The various current regimes in which each type of loss dominates are indicated. From this plot, the task of calculating the bulk resistance of the cell is a simple one since it is merely the magnitude of the slope in the linear region. Determining components of polarization resistance from the I-V plot is far less trivial; other types of testing are warranted for this endeavor. Impedance

spectroscopy is one such route to this information. Shown in the bottom part of Figure 1.4 is a Nyquist plot that might be seen from an impedance test of a cell. The value of Z' at the high-frequency (ω) intercept with the Z' axis can be interpreted as the cell's bulk resistance, while the difference between the low-frequency and high-frequency intercept values is the polarization resistance. In order to characterize the processes responsible for polarization resistance, the loop can be deconvoluted into multiple loops that each represent different "equivalent circuit" elements.[15] These elements are usually resistance-capacitance pairs that have a specific relaxation time constant. Since charge transfer processes have faster relaxation times than mass transfer processes, they generally reside towards the high-frequency (left) side of the loop, while mass transfer processes tend

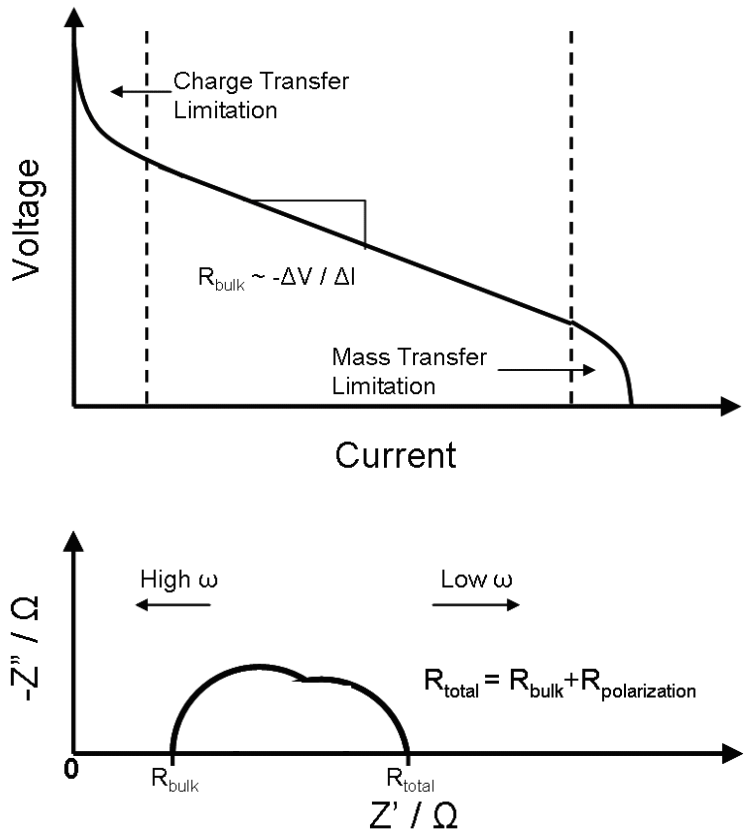

Figure 2.2. V-I (top) and Nyquist (bottom) plots for a typical SOFC.

towards the right side. An excellent and more detailed explanation of impedance spectroscopy and how it generally relates to electrochemical kinetics can be found in the text by Bard and Faulkner.[16]

Impedance spectroscopy, however, may not tell the whole story. While an impedance test might reveal what type of resistance is limiting a cell's performance the most, the specific source of the resistance may not be readily apparent. For example, an equivalent circuit fitting of an impedance spectrum might have a large charge transfer resistance element. One might struggle with determining whether that resistance is a result of slow oxygen reduction at the cathode or contaminant-blocked reaction sites hampering fuel oxidation at the anode. Therefore, other forms of characterization are necessary to ascertain the specific chemical and electrochemical information from these processes that is critical to designing better electrode materials. Research along this line is a large part of the work discussed in this dissertation.

2.4. Issues involving SOFC anodes (fuel-side electrodes)

As was already mentioned, Ni-YSZ cermets are currently state-of-the-art anodes because of their excellent catalytic activity for hydrogen oxidation, electrical conductivity for current collection, and their obvious compatibility with pure YSZ as an electrolyte. On the other hand, the susceptibility of Ni metal to problems such as re-oxidation, carbon buildup (coking) in carbon-containing fuels, and deactivation by fuel contaminants (e.g. sulfur poisoning) when fuels other than hydrogen are used is extensively documented in the SOFC field to date.[8, 9, 17-25] The two latter issues are topics to which particularly heavy amounts of research has been devoted.

2.4.1. Coking of Ni-based anodes

Carbon deposition, or coking, occurs when Ni-based anodes are operated using carbon-containing or hydrocarbon fuels. Two of the major types of coking-related degradation include direct incorporation of carbon into the anode and gas-phase pyrolysis. The nature and mechanism of coking-related degradation in Ni-based anodes depends heavily on the composition of the fuel. In the case of hydrocarbon fuels, the probability of gas-phase pyrolysis of the fuel increases with the order of the hydrocarbon.[9] Thus, pyrolysis is more likely to occur with fuels like C_3H_8, C_4H_{10}, and iso-octane. Meanwhile, coking from CH_4 and C_2H_4 might be more "catalytically" driven by the Ni in the anode. Hill et al. recently performed a detailed study of the effect of direct CH_4 utilization on the Ni-YSZ anode.[24] They determined that the following reactions govern the behavior of CH_4:

$$CH_4 + O^{2-} \rightarrow CO + 2H_2 + 2e^- \quad (2\text{-}10)$$

$$CH_4 \rightarrow C + 2H_2 \quad (2\text{-}11)$$

$$2CO + 3Ni \rightarrow CO_2 + Ni_3C \quad (2\text{-}12)$$

The presence of C and Ni_3C was confirmed in the anode after operation in CH_4 by X-ray analysis. Microscopic analysis of the post-operation anode, which is reproduced in Figure 2.3, revealed features with fibrous morphology. This finding is in agreement with the outcome of a carbon dissolution-precipitation mechanism proposed by others for Ni.[26] In other words, one possibility is that carbon species which separated from CH_4 fuel dissolved into the Ni layer and re-precipitated out, which would eventually disintegrate the anode layer.

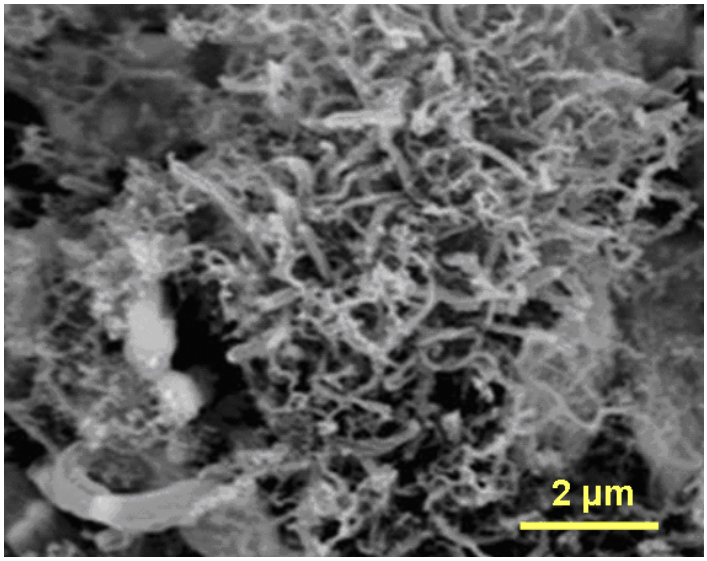

Figure 2.3. Electron microscope image of fibrous carbon on a coked Ni-YSZ anode (reproduced from work by Hill *et al*.[24]

The effect of temperature on severity of coking also depends on the fuel involved. For example, for CO fuel, graphitic carbon can be produced in the anode by the carbon disproportionation reaction, which is shown by the following:

$$2CO \leftrightarrow CO_2 + C \tag{2-13}$$

At cell operating temperatures below 850ºC, Boudouard's equilibrium predicts that this reaction will proceed in the forward direction, depositing carbon on the anode surface.[11] Therefore, cell performance will actually decrease faster at lower temperatures. On the other hand, for fuel like CH_4, higher operating temperatures result in more rapid degradation. As experimentally observed by Barnett and co-workers, a cell that operated with relatively stable behavior for at least 3 hours at 700ºC completely failed within less than an hour at the same operating current.[8] Finally, increasing cell current (i.e. fuel utilization) decreases the rate of performance degradation.[8, 17]

2.4.2. Sulfur poisoning of Ni-based anodes

Even when treated with desulfurization processes, fuels such as natural gas, diesel, and jet fuel tend to have appreciable sulfur content, usually in the form of H_2S. Therefore, operating a cell with Ni-containing anodes on these types of fuels inevitably results in sulfur poisoning of the anode. The most common type of sulfur poisoning for Ni-YSZ anodes is characterized by a rapid drop in cell performance upon introduction of a small amount of H_2S into the fuel stream. For example, a cell operating on 1-2 ppm H_2S in a H_2 fuel might experience a 10% drop in power output versus a cell utilizing H_2 fuel devoid of sulfur content[20].

Mechanistically, the sulfur dissociates from the H_2S and adsorbs on the Ni surface, as represented by the following:

$$H_2S + s^{\#}_{Ni} \rightarrow H_2 + S^{\#}_{Ni} \qquad (2\text{-}14)$$

The $s^{\#}_{Ni}$ symbol represents a Ni surface site. The adsorbed sulfur effectively deactivates the Ni surface, blocking reaction sites in the vicinity. Unlike coking, which can have deleterious effects on both the surface and bulk structure of Ni-YSZ anodes, under typical fuel cell operating conditions, sulfur poisoning is largely a surface-specific phenomenon, which also accounts for the fact that its effects are complete within minutes of introducing the sulfur.[20] At operating temperatures above 600ºC, with H_2S concentrations upwards of 1000 ppm in fuel gas flow, formation of bulk nickel sulfide is not thermodynamically favorable[27]. On the other hand, at 800ºC, adsorption of elemental sulfur on the Ni surface is thermodynamically favorable even at H_2S concentrations as low as 0.1 ppm. As temperature is decreased, this type of sulfur poisoning is possible at even lower concentrations of H_2S.

As with coking, the effects of sulfur poisoning can be reduced by running a cell at a higher current. The following is a possible reaction mechanism responsible for this phenomenon[20]:

$$S_{Ni}^{\#} + 2O^{2-} \rightarrow SO_2(g) + s_{Ni}^{\#} + 4e^{-} \quad (2\text{-}15)$$

Ni does not catalyze the dissociation of SO_2 nor does SO_2 adsorb well onto the Ni surface, so the sulfur is effectively carried away from the Ni in this manner. Running the cell at a higher current induces a higher oxygen flux, resulting in more sulfur being carried away.

Due to the transient nature of the sulfur adsorption on Ni, sulfur poisoning is also a reversible phenomenon. By removing the source of sulfur from the fuel stream, all of the sulfur would theoretically be removed from the surface as long as the H_2S concentration was low enough. Eventual full recovery of performance has been experimentally observed upon removal of H_2S from H_2 fuel, although this process generally takes considerably more time than the poisoning itself.[18, 20, 25, 28] Of course, the surface specificity and transience of sulfur poisoning itself has made the task of studying this phenomenon a difficult one; traditional electrochemical techniques have proven useful in characterizing the contribution of sulfur poisoning to polarization resistance, but more chemically-oriented methods are necessary to truly understand its mechanism and find the key to sulfur tolerance.

2.4.3. Alleviating anode degradation

A multitude of approaches have been used to solve the issues of coking and sulfur tolerance, including the use of “Ni-free” conductive oxides. These alternative materials have shown promise in averting the problems inherent to Ni-based anodes but create issues of their own in terms of cost and compatibility with well-established technology.

Recently, a couple of different approaches were adopted to solve the problems of coking and sulfur poisoning in Ni-based anodes. One involved the replacement of YSZ in a Ni-YSZ cermet anode by the dual-ion (O^{2-}/H^{+}) conducting electrolyte material $BaZr_{0.1}Ce_{0.7}Y_{0.1}Yb_{0.1}O_{3-\delta}$ (BZCYYb)[29]. The rationale was that the –OH groups produced on anode surfaces by dissociative adsorption of water greatly facilitate oxidation of carbon to CO_2 and H_2S to SO_2, thus removing unwanted deposits and species from anode surfaces. Alternatively, these –OH groups might drive *in situ* reformation of carbon-containing fuels under typical SOFC operating conditions, minimizing the coking that occurs in the first place. Like other proposed conductive oxides, however, BZCYYb is not very compatible with other oxygen anion-conducting electrolytes like YSZ.

One theory proposed that BZCYYb provided protection to the Ni by distributing minute amounts of BaO over the Ni surface during high-temperature processing. Thus another approach was attempted in which nano-sized BaO islands were deliberately created on the surface of the Ni grains in a Ni-YSZ cermet anode using a vapor phase deposition.[6] The resistance to coking was also dramatically enhanced in this case, although sulfur poisoning remained a problem.

Some questions remain on the role that water plays in the coking and sulfur tolerance of Ni-based SOFC anodes containing BZCYYb and other surface modification. Answering these questions would be greatly facilitated by studying the anode surface under relevant operating conditions by an "*in situ*" chemical analysis method that allows for tracking of the evolution of water, carbon, and sulfur species as well as new phases at SOFC anode surfaces while they are subject to various temperatures, atmospheres, and electrochemical stimuli. This type information, coupled with performance data, would

help to unravel the mechanism of the electrode reactions (i.e. the connection between water and anode poisoning tolerance) and thus offer better insights vital to design of better electrodes.

2.5 Issues involving SOFC cathodes (air-side electrodes)

On the other side of the SOFC, a major issue facing the development of SOFCs with high performance capabilities at low temperatures is the lack of complete understanding of the oxygen reduction process on the cathode. This series of physical and chemical phenomena is the main culprit behind cathodic interfacial polarization, which limits the performance of the cell. Some consensus exists among scientists as to which types of events occur during the process. They include the adsorption of oxygen molecules, the dissociation of these molecules into atoms, the reduction of atoms and molecules to ions, and the incorporation of ions into the electrolyte.[30, 31] The order and dominance of these events in the process is the subject of much scientific debate, as is which step is rate-limiting. For example, the oxygen molecules may be partially reduced rather than becoming fully reduced species after adsorbing onto the surface of the cathode. In addition, the ionic species in question have multiple possible transport routes towards incorporation into the electrolyte, including cathode surfaces, interfaces, and the bulk of the cathode material itself. The oxygen species could potentially be reduced at any time during transport.

Some combination of these events forms a rate-limiting mechanism for the oxygen reduction, and discovering that mechanism defines one important piece of information for optimizing SOFC cathode materials and systems. While studies have

been performed with the goal of characterizing the oxygen reduction process of popular cathode materials such as doped lanthanum manganites and cobaltites under various performance conditions, they have been widely based on electrochemical analysis via impedance spectroscopy.[31-33] As mentioned above, a simple impedance spectrum can quickly become convoluted by the influence of multiple processes, and its interpretation is especially difficult when the details of these processes are largely unknown.

The following equation, which uses Kröger-Vink notation, represents the overall electrochemical reaction on the cathode side of a generic SOFC:

$$\frac{1}{2}\mathrm{O}_{2(\mathrm{gas})} + V_O^{\bullet\bullet} + 2e' \rightarrow O_O^X \qquad (2\text{-}16)$$

As mentioned above, in this reaction, oxygen gas is reduced by electrons supplied by the cathode and incorporated into a vacant lattice site. As such, the gas, electrons, and vacancies must be simultaneously present in order for the reaction to proceed. When the cathode is a pure electronic conductor and does not have the vacancies to incorporate and conduct ions, the electrochemical reaction will only take place around the triple phase boundary (TPB) of the electrode, electrolyte, and gas. As a result, very little active surface area is available for reaction. Therefore, pure electronic conductors like the noble metals that are required for successful electrocatalysis in proton exchange membrane (PEM) fuel cells[34] are not necessarily the ideal candidates for SOFC cathodes.

Mixed ionic-electronic conductors (MIECs), as their name implies, are conductive of electronic and ionic sites. These types of materials fill the role of the SOFC cathode better, as they can potentially extend the catalytically active sites over wherever the cathode surface area is in contact with the gas, creating parallel paths with the TPBs for conduction.[35] Previous investigations have indicated that materials such as $La_{1-x}Sr_xCoO_{3-}$

$_{\delta}$ (LSC), $La_{1-x}Sr_xCo_{0.2}Fe_{0.8}O_{3-\delta}$ (LSCF), and $Sr_{0.5}Sm_{0.5}CoO_{3-\delta}$ (SSC) show notable levels of mixed conduction below 700°C.[36-38] Some researchers have also considered two-phase MIEC cathode materials, such as a composite of LSM and YSZ[39, 40]; LSM is generally accepted as an electronic conductor, while YSZ is an excellent oxide ion conductor. Thin coatings have been previously implemented to LSCF backbone to provide additional catalytic activity and stability.[41, 42] The search for materials and architectures that are more active for the oxygen reduction reaction at lower temperatures has led to other more "exotic" cathode materials[43] including doped $SrFeO_3$[44], $Ba_{0.5}Sr_{0.5}Co_{0.8}Fe_{0.2}O_{3-\delta}$ composites[45], and SSC with cone-shaped microstructure.[46]

Even with the advent of such materials for use in SOFCs, the interfacial polarization resistance at the cathode still limits the performance of fuel cells with lower operating temperatures. While the intrinsic conductivity and catalytic prowess of an effective MIEC cathode material are important, the properties of its microstructure have significant bearing on its ultimate performance. These attributes include the connectivity of the bulk of the electrode along with the surface area available to the gas. A comprehensive understanding of the oxygen reduction process is needed in order to find the optimum balance of these properties.

Oxygen reduction mechanisms for MIEC cathodes will differ based on the amount and order of steps taken towards an oxygen ion's final incorporation into the electrolyte. Shown in Figure 2.4a are only two of the many possible sets of steps, depending on whether the oxygen is first reduced or dissociated. The reduction process will also depend on the configurations that occur on the surface of the cathode. Two possible species configurations are superoxo and peroxo.[47] Figure 2.4b displays these

configurations and some of the possible interactions they undergo during the oxygen reduction process.

Mixed conduction further complicates the oxygen reduction process, since the electrochemical reaction described above takes place at multiple types of interfaces. These possible interfaces are represented in Figure 2.4c. Notwithstanding at which type of interface the oxygen is fully reduced and incorporated, the oxygen ions may still need to diffuse through the bulk of the cathode or possibly over its surface to reach the electrolyte. These types of transport have been previously investigated; for example, finite element methods have been previously implemented to isolate types of transport and work towards finding the rate limiting step in oxygen reduction.[48] Similar techniques have been used in conjunction with X-ray tomography to ascertain the role of microstructure in the oxygen reduction reaction.[49] More experimental methods might advance these types of ends even further.

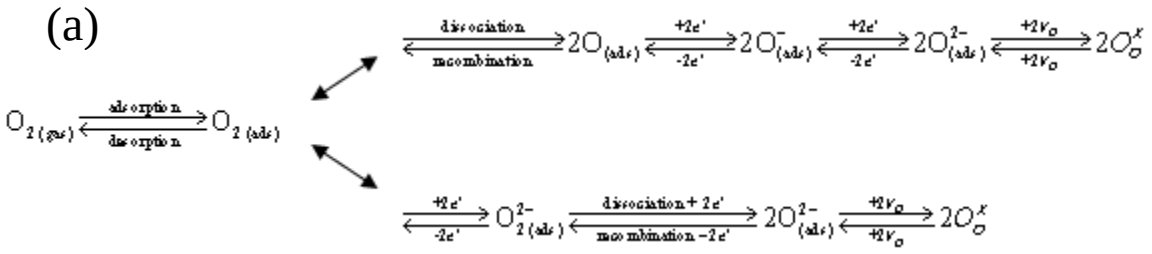

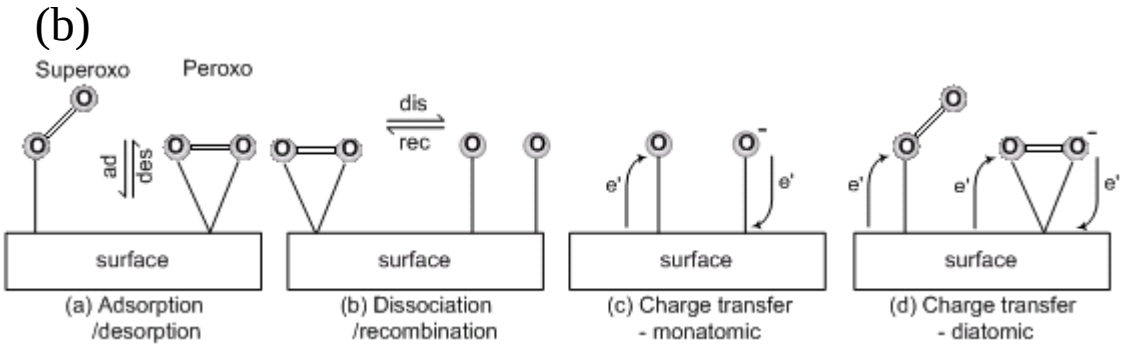

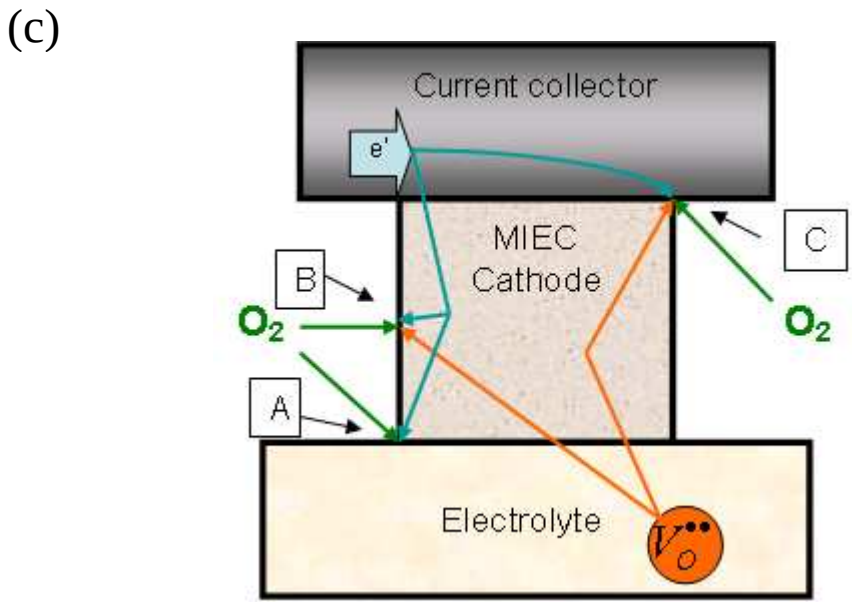

Figure 2.4. (a) Example reaction paths for oxygen reduction, (b) oxygen adsorption configurations, and (c) possible oxygen reduction reaction sites for a cathode composed of a mixed electronic-ionic conductor (MIEC).

2.6. Characterization by Raman spectroscopy

Through a collection of recent research efforts, Raman spectroscopy has already been shown to be an effective tool for studying a variety of SOFC problems. Previous investigations have included probing of oxidation states in Gd-doped ceria (GDC) electrolytes under reducing atmosphere[50], modification of glass sealants for full SOFC systems[51], and Cr poisoning of cathodes for cells that have metallic interconnects[52]. Raman spectroscopy has also been used in other investigations of electrode processes including coking, sulfur poisoning, and oxygen reduction. The research work supporting this dissertation is meant to expand and improve upon that information in order to contribute new insights to the SOFC field.

In the following sections, some of the basic origins of Raman spectroscopy and brief examples of its applicability to the field of SOFC materials science are described. For further information on the general subject of Raman spectroscopy not covered in this dissertation, a great deal of literature exists in the field, including several excellent textbooks[53-55].

2.7. Fundamentals of Raman scattering and spectroscopy

Raman scattering, the principle on which Raman spectroscopy is based, is a type of inelastic light scattering, which is itself known as a "two-photon" process. Generally speaking, inelastic light scattering involves the impingement of a photon of a particular energy on some medium or material. This photon is annihilated, and simultaneously, a second photon of a different energy is created and travels away from the material. Since the energy of a photon is proportional to its frequency by Planck's relation, the incident

and scattered photons can respectively be characterized by their frequencies, υ_i and υ_s. In a case where $\upsilon_s < \upsilon_i$, some quantum of energy was transferred from the original photon to the impinged material, and what is known as a "Stokes" process has occurred. The opposite case ($\upsilon_s > \upsilon_i$) is unsurprisingly called an "anti-Stokes" process, but anti-Stokes scattering is observed less frequently since the scattering medium needs to be in an excited state for it to occur.[53]

Raman scattering, which fits into this category, is so named because of its first reporting by C. V. Raman and his colleague in 1928.[56] In Raman scattering, the energy or frequency difference between the incident and scattered photons corresponds to some vibrational mode within the scattering medium or material. Raman spectroscopy, in turn, is a technique in which light is directed at a material or substance and the resulting backscattered Raman radiation is detected in order to determine its nature from characteristic vibrational modes. The most common incident light source used to illuminate samples in Raman spectroscopy is a laser, although some have tried using other sources such as synchrotron X-rays.[57] The reasons that a laser is ideal for this technique are that the wavelength (and therefore frequency) can be fixed and that many photons can be concentrated in one spot. A large number of photons are required for successful detection of Raman scattered light because only 1 in millions of photons that undergo a scattering process are of the Raman variety, on average.[54] Most light undergoes Rayleigh (or elastic) scattering in which the incident and scattered photon energies are equal. Generally, laser wavelengths utilized for Raman spectroscopy fall between the ultraviolet (UV) and infrared (IR) ranges; 514 nm (green) and 633 nm (red) wavelengths are used in the research described in this dissertation.

During a Raman spectroscopy experiment, backscattered radiation from a sample is physically separated by position into the different frequencies it contains before being collected by a detector. Rayleigh scattered light is filtered out before this stage. The frequency shifts between the Raman scattered light and incident light are plotted on an intensity spectrum where vibrational modes appear as intensity peaks. By convention, Raman shifts are expressed in cm^{-1} (wavenumber) units. In a Raman spectrum plot, the Raman shift axis units are best labeled as "Δcm^{-1}" to clarify that a shift in frequency between the incident and scattered light is being expressed rather than an absolute frequency itself, since the shift directly represents the vibrational mode of a material. Making this distinction helps prevent confusion with IR vibrational spectroscopy, in which absolute light frequencies correspond to vibrational modes.

2.8. Vibrational modes and Raman selection rules

The most simplistic way to model the connection between Raman scattering and the vibrational modes is in a classical, "macroscopic" manner.[53, 54] Figure 2.5 shows a classical representation of a water molecule. Generally speaking, molecules with N atoms have $3N - 6$ vibrational modes, which equates to the number of degrees of freedom of a molecule ($3N$) excluding 3 translational and 3 rotational modes. Since water has 3 atoms, it has 3 vibrational modes[58]: symmetric stretching, asymmetric stretching, and bending. While these three modes are all observable by Raman spectroscopy, or "Raman-active," not all vibrational modes fit this category. Fortunately, selection rules have been devised in this field to identify what types of vibrations are Raman-active.

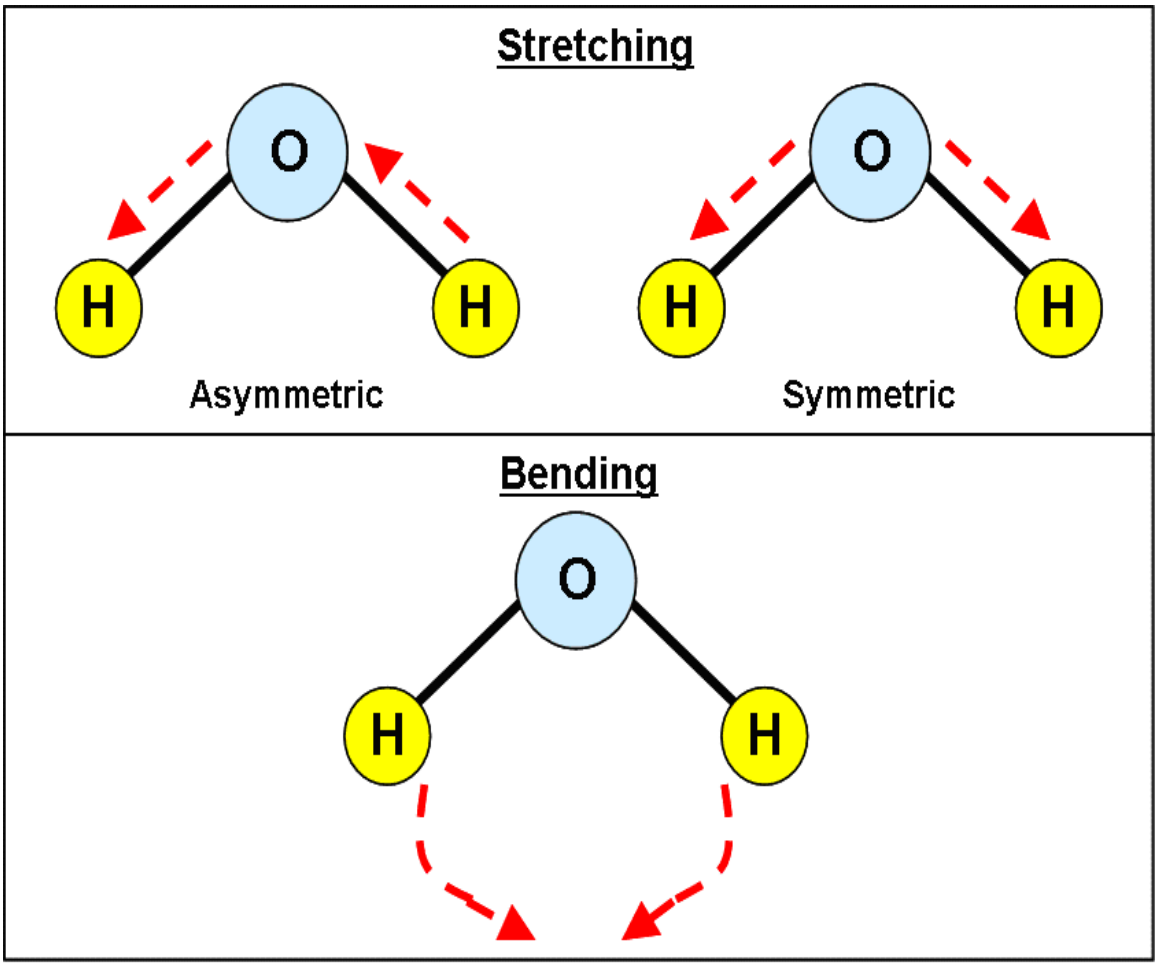

Figure 2.5. Vibrational modes of a water molecule.

The strongest inelastic scattering processes in a given material or substance are due to the coupling of light and electric moments, and this coupling can be understood as a modulation of the electric susceptibility to polarization caused by the excitation from the incident light.[53] Therefore, a vibration associated with Raman scattering can be treated as an induced dipole moment, which is expressed in the below equation[54]:

$$\mu_i(\nu_s) = \alpha_{ij} E_j(\nu_i) \tag{2-17}$$

$E_j(\upsilon_i)$ is the electric field caused by the incident light as a function of that light's frequency, $\boldsymbol{\alpha}_{ij}$ is the polarizability tensor of the scattering medium, and $\mu_i(\upsilon_s)$ is the

induced dipole moment as a function of the scattered light's frequency. A particular vibrational mode is Raman-active if this polarizability tensor $\boldsymbol{\alpha}_{ij}$ changes with position during the vibration, or in mathematical terms:

$$\frac{d\alpha}{dx} \neq 0 \tag{2-18}$$

The behavior of $\boldsymbol{\alpha}_{ij}$ largely depends on the symmetry of the material or molecule in question. Thus, only vibration modes of certain symmetries are Raman active. In centrosymmetric molecules and materials, Raman-active modes have gerade (or "even") symmetry; hence, all Raman mode notations will have a "g" subscript. As an aside, so called "IR-active" modes, which are observable by IR vibrational spectroscopy, have ungerade symmetry (i.e. odd, subscript "u"). Raman-active and IR-active modes are therefore mutually exclusive for centrosymmetric materials. On the other hand, for non-centrosymmetric materials and molecules, this mutual exclusivity rule does not apply[54]; water is a good example of this case, as all three of its vibrational modes are both Raman-active and IR-active.

Using group theory, theoretically observable Raman modes for a particular substance can be determined by symmetry-based selection rules, making characterization of a material or substance by Raman spectroscopy an easier task. Of course, Raman activity of a mode does not guarantee that it will actually be observed when spectroscopy is performed; enough photons are needed to meet the spectrometer's detection threshold. The so-called intensity of a Raman scattering mode depends on the molecule's Raman "cross-section," which in turn depends on the actual polarizability of the mode. The intensity will also depend on the properties of the incident light used during spectroscopy. The observed Raman scattering intensity therefore follows this proportionality:

$$I \propto L\alpha^2 \nu_i^4 \quad (2\text{-}19)$$

L represents the power of the incident radiation (i.e. laser power). As the equation shows, a greater magnitude of polarizability and a light source of higher frequency (i.e. shorter laser wavelength) result in much greater Raman scattering intensity.

2.9. Raman spectroscopy of crystalline phases relevant to SOFC

When using Raman spectroscopy to analyze materials of virtually perfect crystallinity, most of the vibrational modes that are observed are known as lattice phonon modes. The theoretically Raman-active modes in this category for a given material can be easily ascertained from a standard character table if the space group is known and assigned to peaks on the spectrum. More peaks may be observed on the spectra than the theoretical amount of vibrational modes; if extra peaks occur at approximate integer multiples of the frequency of an assigned peak, it is likely an overtone of that peak. A significant number of defects in the material may also cause other Raman modes to appear.[53] New modes will usually emerge on spectra in the form of shifting or splitting of existing peaks; a good example is shown by a Raman spectrum collected from a sample of the common SOFC electrolyte material Sm-doped CeO_2 (SDC), which is displayed in Figure 2.6. CeO_2 has 6 total lattice phonon modes and belongs to the space group $Fm\bar{3}m$ (O_h^5).[59, 60] The triply degenerate vibrational mode F_{2g}, which is Raman-active, accounts for 3 of these modes, while the other 3 comprise the IR-active mode F_{1u}. Thus, only one peak corresponding to F_{2g} should be observed in a given Raman for CeO_2 at around 460 cm^{-1}.[59] The spectrum in Figure 2.6 from the Sm-doped sample, however, displays three

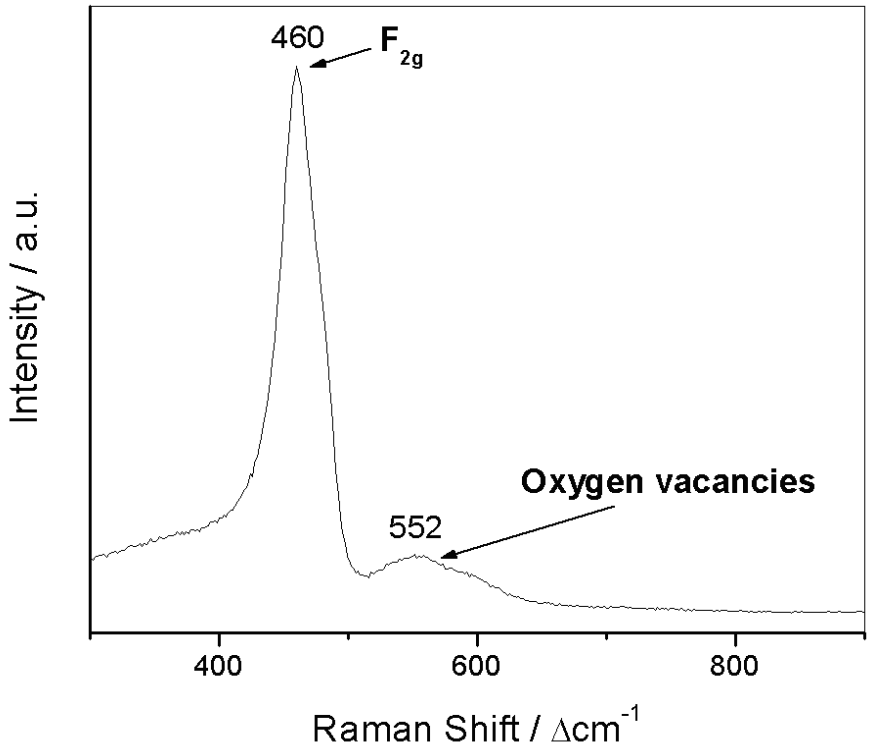

Figure 2.6. Raman spectrum collected in air from $Sm_{0.1}Ce_{0.9}O_{2-\delta}$ powder.

distinct peaks. Therefore, the other peak at 552 cm^{-1} correspond to extra oxygen vacancies induced by the Sm doping.[59]

Graphite, which is the form of carbon seen in coked anode materials, provides a very similar scenario; its space group is $P6_3/mmc$ (D_{6h}^4), and it theoretically contains only one doubly degenerate mode Raman active mode (E_{2g}).[61] This mode manifests as a peak near 1585 cm^{-1} on a Raman spectrum collected from carbon and is colloquially called the "G-band." For most carbon samples, other peaks can often be seen on the spectra that correspond to defects and resulting disorder in the graphite structure; in particular, a peak near 1360 cm^{-1} is common (the "D-band"). Discussion of carbon Raman spectra comprises a considerable portion of the rest of this dissertation.

Characterizing SOFC cathode materials by Raman spectroscopy tends to pose a trickier situation. For example, LSM, a popular cathode material, is an orthorhombically distorted perovskite belonging to the space group Pnma (D_{2h}^{16}).[62] This space group has 24 theoretically Raman-active vibrational modes (7 A_g + 5 B_{1g} + 7 B_{2g} + 5 B_{3g}). Since the structure of LSM is close to a cubic perovskite in character, however, its polarizability properties are weak, so its Raman cross section is low. The bottom spectrum shown in Figure 3.3 was collected from a sample of $La_{0.85}Sr_{0.15}MnO_{3-\delta}$ powder; because of the low Raman signal, only a shallow broad band between 250 and 800 cm^{-1} can be observed. This spectrum required a ~10-minute collection time to achieve the little bit of signal that can be seen.

Low signal does not necessarily disqualify Raman spectroscopy as a useful characterization technique for SOFC cathodes. On one hand, signal from the bulk has a smaller chance of swamping useful signal from surface species that are critical to understanding reaction mechanisms. Nevertheless, structural information about the bulk material's behavior is still accessible. The top spectrum in Figure 2.7 was obtained from LSCF, another popular cathode material. As a rhombohedrally distorted perovskite, LSCF is in the space group $R\bar{3}c$ (D_{3d}^{6}) [63] and has 5 Raman-active modes (1 A_g + 4 E_g). Broad peaks for 3 of the E_g modes can be seen in the collected spectrum at 321 cm^{-1}, 520 cm^{-1}, and 697 cm^{-1}.[64] The spectrum under the one from LSCF, which has the same overall shape with peaks in similar positions, was actually collected from a sample of LSM with different stoichiometry ($La_{0.8}Sr_{0.2}MnO_{3-\delta}$). The radical change in the Raman spectrum associated with the minute change in the LSM stoichiometry suggests a considerable change in the overall structure of the material from Pbnm to $R\bar{3}c$. The largest difference

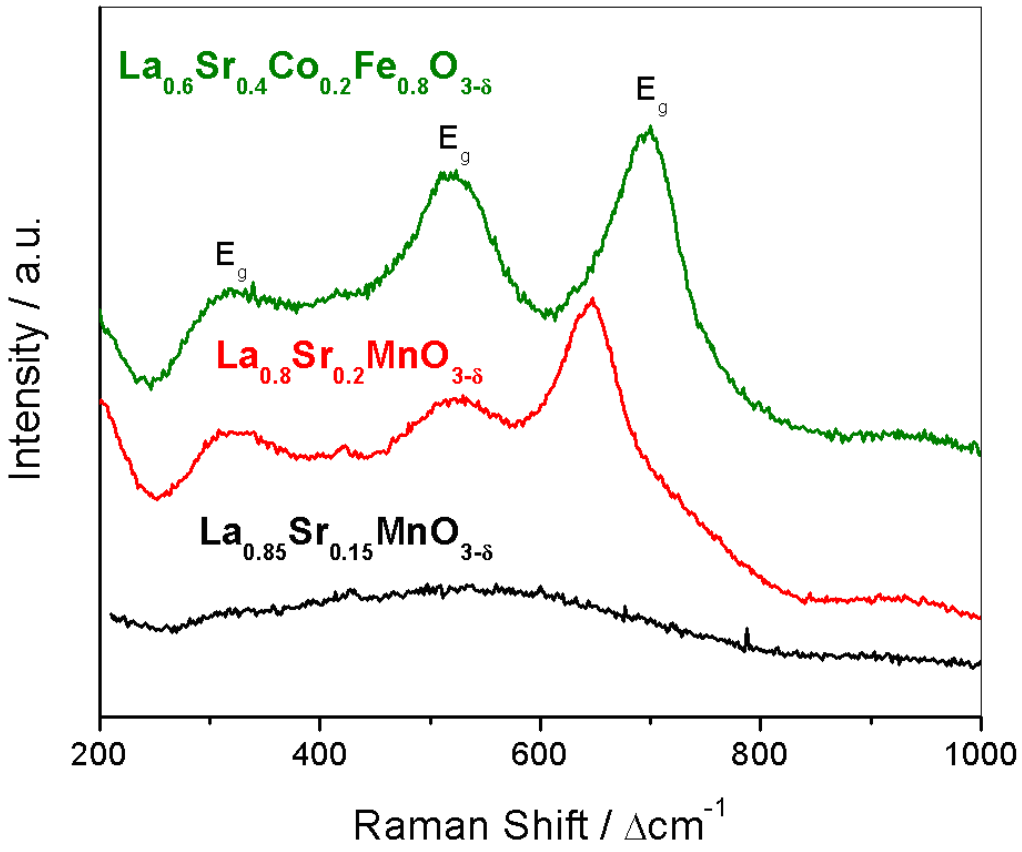

Figure 2.7. Raman spectra obtained from one LSCF sample (green trace) and two LSM samples with slightly different stoichiometry (red and black trace).

between the LSCF and $La_{0.8}Sr_{0.2}MnO_{3-\delta}$ spectra is the position and shape of the rightmost band (697 cm^{-1} and 646 cm^{-1}, respectively). Since this band corresponds to vibrations between the B-site and O ions, the difference in B-site ions between the two materials might account for this distinction.

A similar transition of LSM with a change in La:Sr ratio was reported by Mitchell *et al.*[62] Hence, Raman spectroscopy might serve as a good indicator of Sr segregation, which is a possible degradation mechanism in SOFC cathode materials.

2.10. Raman spectroscopy and SOFC electrode surface characterization

While Raman spectroscopy is technically a "near-surface" analysis technique due to its relatively large information depth, it is still useful for characterizing SOFC surfaces. The main advantage of Raman spectroscopy lies in the fact that it possesses large flexibility in terms of conditions under which it can be performed, including the harsh temperatures and atmospheres inherent to SOFC electrode operation. In addition, it is quite sensitive to a vast variety of materials and chemical species that are of interest to the SOFC field, including different forms of carbon[61, 65, 66], hydrocarbons[67], sulfur[68-70], oxygen[71-73], and water.[5-7] Table A.1 in Appendix A summarizes information about the Raman vibrational modes of these materials. One possible drawback is that Raman spectroscopy is not sensitive to pure metals such as Ni, but the presence of these materials within the SOFC system tends to be a fixed assumption, so this disadvantage does not necessarily apply. Moreover, Raman spectroscopy can potentially be used alongside electrochemical measurements to probe surface species and phases of interest (e.g. anode reaction intermediates and products), allowing the direct correlation of electrochemical performance to electrode surface chemistry. Therefore, the use of this technique in the fuel cell and electrochemistry fields in general has recently grown, and part of the impetus for this dissertation is further demonstration of its excellent utility.

CHAPTER 3: TECHNICAL APPROACHES

3.1. Overview of the Raman spectroscopy system

A major portion of the work presented herein was performed using some form of Raman spectroscopic characterization. All Raman measurements were performed using a Renishaw RM1000 spectromicroscopy system owned by the Center for Innovative Fuel Cell and Battery Technologies at the Georgia Institute of Technology. With this system, 488 nm and 514 nm excitations can be supplied with a Modu-Laser StellarPro 150 air-cooled Ar-ion laser, while 633 nm excitation is supplied by a Thorlabs HRP170 He-Ne laser. The spectrometer contains laser line cleanup filters and Rayleigh cutoff filters to accommodate these three excitation lines, although the experiments in this work only utilized 514 nm and 633 nm excitations. For a typical spectrum collection, Raman signal was backscattered off the sample surface at 180º, separated by a diffraction grating (1800 lines/mm), and collected using a thermoelectrically cooled CCD camera. Figure 3.1 displays the optical pathway and signal collection schematic of the Raman spectroscopy system.

The microscope part of the system consists of a Leica DM series upright microscope equipped with a Prior Scientific ProScan II motorized x-y-z stage. The stage has a step size of 20 nm, which allows precision movement well within the spatial resolution of the Raman microscope itself. Laser excitation was focused and backscattered Raman signal was collected through the same 50X objective (0.40 NA, 8.8 mm working distance). The 50X objective allows for optical images with 500X

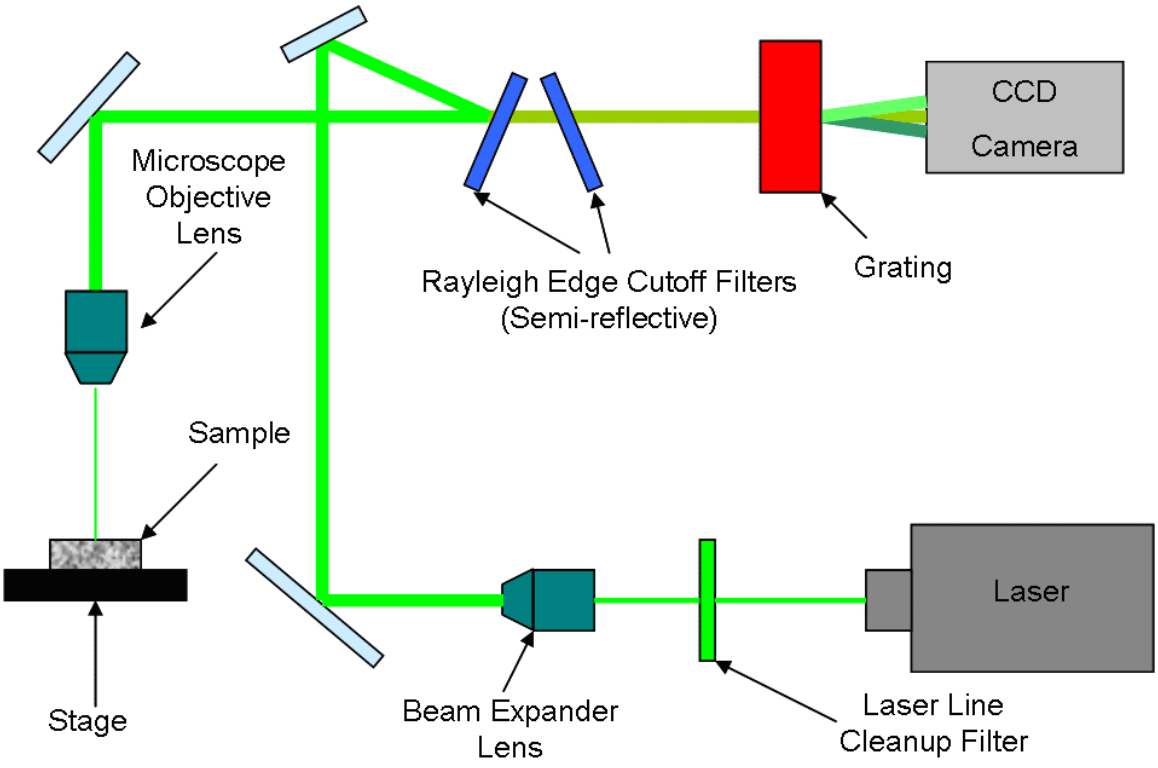

Figure 3.1. Schematic of the optical pathway and signal collection in the Renishaw RM1000 Raman spectromicroscopy system.

magnification and for the laser excitation to be focused on a spot with 1-2 μm diameter, giving an effective spatial resolution of 2 μm for Raman signal collection. Collection and integration time depended heavily on the materials being analyzed and varied between as little as 5 seconds and as much as 1 hour.

3.2. *In situ* Raman spectroscopy

For *in situ* Raman measurements calling for environmental conditions other than ambient atmosphere, a high-temperature reaction chamber (HTRC) from Harrick Scientific was employed. The chamber was originally converted from a Harrick Praying Mantis chamber used for diffuse reflectance infrared spectroscopy. The chamber's top

window is transparent quartz, which still allows for the same 180° backscattering geometry as in conventional Raman measurements. The chamber can accommodate gas flow using VCO and Swagelok tube fittings. The chamber can also heat ceramic sample surfaces up to 600-650ºC; the chamber itself can withstand up to 750ºC, but there is always a temperature gradient between the heating element under the sample holder and the top surface of the sample being measured. An example calibration curve showing this temperature difference is given by Figure B.1 in Appendix B. Finally, a cooling water line that runs through the chamber carries away excess heat and prevents thermal damage to sensitive equipment in close proximity to the chamber such as the motorized stage and the microscope's objective lens. A photograph of the chamber is shown below in Figure 3.2.

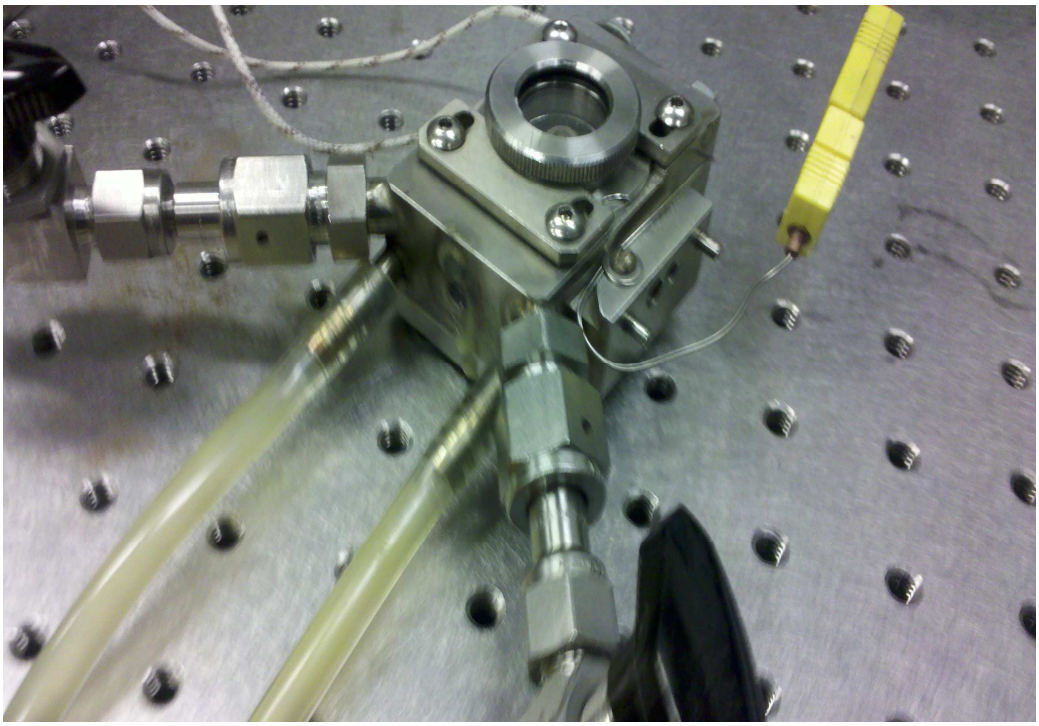

Figure 3.2. Photograph of environmental chamber used for *in situ* Raman microscopy.

Electrochemical characterization was combined with Raman spectroscopy for certain *in situ* experiments. The main equipment for this type of analysis was an Arbin MSTAT multi-channel potentiostat. DC polarization can be applied to the sample of interest as an electrochemical driving force by lead wires to simulate electrochemical operating conditions within a fuel cell system. Platinum wires threaded through the environmental chamber's quartz window were used for experiments requiring polarization and current collection. These wires were attached to a DC-sputtered Ag working electrode on the analyzed side of the sample and a porous Ag counter electrode on the opposite side using Ag paste. The electrochemistry induced here can be effectively coupled with the Raman data to semi-quantitatively relate the chemical and electrochemical interactions on the cathode surface. This methodology was used to study the surface of BZCYYb. A photograph and schematic of the complete apparatus are both shown in Figure 3.3.

3.3. Sample preparation for *ex situ* and *in situ* Raman characterization

Raman spectroscopy was used to analyze the structure and water adsorption characteristics of various BaO-containing materials and modifications: $BaZr_{0.1}Ce_{0.7}Y_{0.1}Yb_{0.1}O_{3-\delta}$ (BZCYYb), BaO-modified Ni, and $BaZr_{0.8}Y_{0.2}O_3$ (BZY).

BZCYYb powder was prepared by conventional solid state reaction. Stoichiometric amounts of high-purity barium carbonate, zirconium oxide, cerium oxide, ytterbium oxide, and yttrium oxide powders (all from Aldrich Chemicals) were mixed by ball milling in ethanol for 48 hours, followed by drying in an oven and calcination at 1100 ^{o}C in air for 10 hours. The calcined powder was ball milled again, followed by

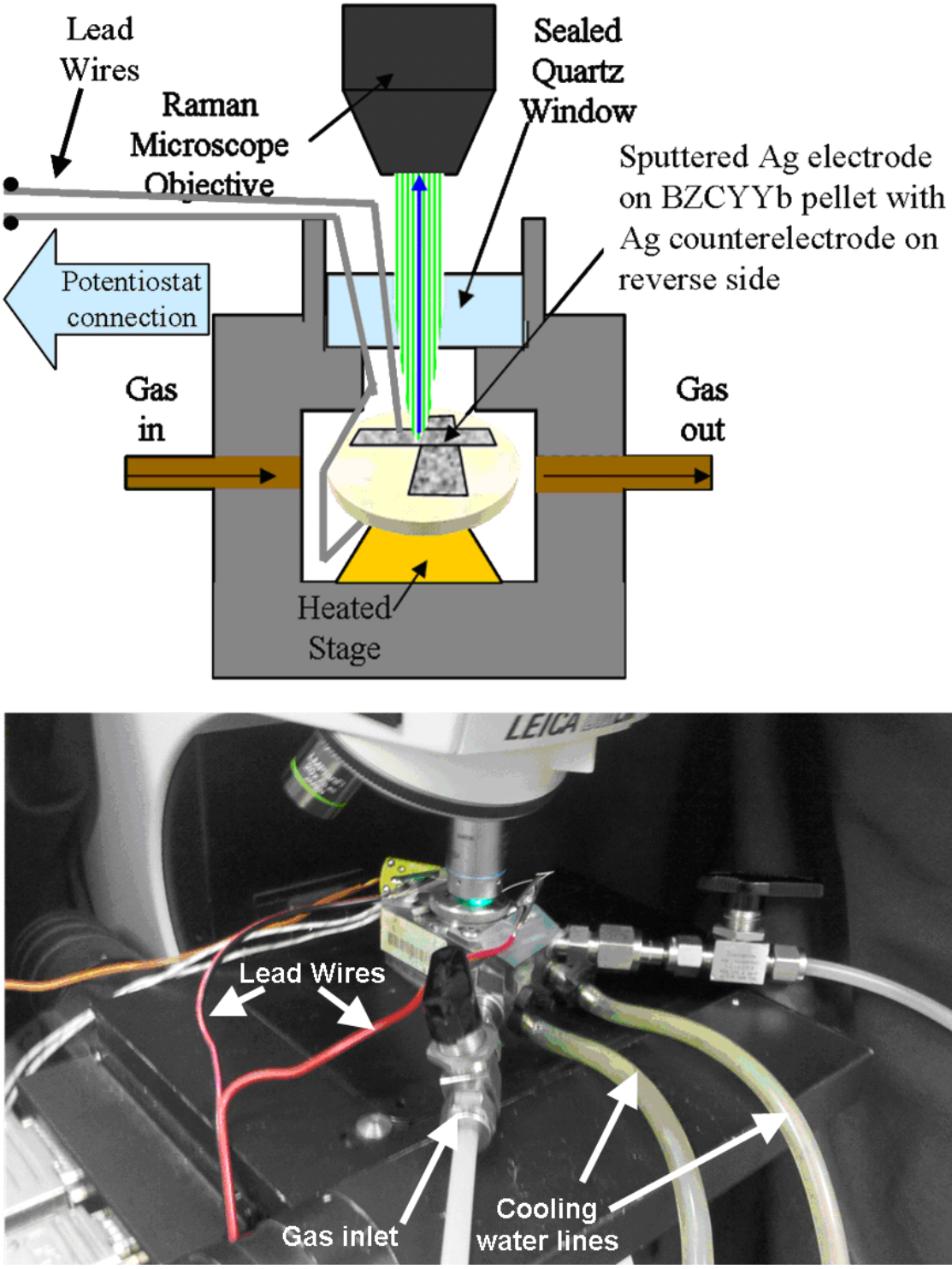

Figure 3.3. Schematic of *in situ* electrochemical Raman analysis (top) along with a photograph of the setup (bottom).

another calcination at 1100^{o}C in air for 10 hours. Some powders were analyzed directly, while other powders were uniaxially pressed into a disk at ~275 MPa and sintered at 1550 ^{o}C for 10 hours in air. One face of each of the sintered pellets was then ground and polished to a grade of 1 μm.

For BaO-modified Ni, the modification was introduced to the NiO powder through evaporation deposition; NiO powder was fired at 1200ºC for 2 hours in the presence of BaO powder without any direct contact between NiO and BaO particles. Modified and blank NiO powders were then treated in flowing dry H_2 at 600ºC for 2 hours in order to reduce the NiO to Ni.

Finally, BZY was fabricated by ball-milling stoichiometric amounts of YSZ (Daichii) and $BaCO_3$ for 24 hours in EtOH with zirconia media and firing the powders at 1100ºC for 10 hours.

3.4. Raman mapping and monitoring

For part of this work, Raman spectroscopy was used to study carbon deposition and sulfur poisoning on Ni anodes. Different types of samples were prepared for this investigation. First, square Ni coupons (~8 mm) were prepared from Ni foil (Alfa Aesar) and polished to a grade of 0.1 μm using diamond media, after which the coupons were cleaned ultrasonically in acetone, washed with ethanol and purified water, and then dried under a compressed air stream. The coupons were exposed to flowing gas mixture (>100 sccm flow rate) composed of 15% H_2 and 10% C_3H_8 in dry Ar for 5 minutes at 550°C in a quartz tube to induce chemically-driven carbon deposition over the Ni surface.

For the patterned strip electrode samples, YSZ substrates were first prepared by tape-casting a YSZ powder slurry (Daiichi). The tape was cut into 1.7 cm discs, after which stacks of 3 discs were laminated by uniaxial pressing. The laminated stacks were sintered into dense pellets at 1450ºC for 5 hours in air. The dense pellets had a thickness of ~400 μm. The pellets were subsequently cleaned and patterned with Ni strips deposited using photolithography methods like those described elsewhere.[74, 75]

Samples with Ni mesh electrodes were also prepared. Squares of Ni mesh (Alfa Aesar, size 50) that were <1 cm in size were sandwiched between packs of YSZ powder and uniaxially co-pressed with the packed powder into 13-mm disc pellets (~1 mm thickness). The pellets were sintered at 1440ºC for 5 hours in a tube furnace under a flowing reducing gas atmosphere (4% H_2/bal. Ar) to prevent degradation of the mesh by oxidation. After firing, one face of each pellet was mechanically ground away to reveal the embedded Ni mesh. The embedded mesh surface was then further polished and cleaned by the same method used for the Ni coupon samples. Figure 3.4 illustrates the steps for making these samples and shows some magnified images of a typical exposed Ni mesh.

A modification was applied to the Ni mesh samples for some samples by heating them to 1200ºC for 2 hours in reducing atmosphere (4% H_2/bal. Ar) with BaO powder present in the same crucible. While the BaO powder was not placed in physical contact with the samples, vapor evolved and deposited on the revealed Ni mesh surface. For the purpose of *ex situ* measurements, a selection of the patterned Ni and plain/modified Ni mesh pellets were heated to 625°C in flowing C_3H_8 gas for 2 hours. In addition, some Ni mesh pellets were used as anodes functional cells by adding Ag paste to the opposite face

of the pellet and operating the anodes in 20 ppm H_2S / bal. H_2 fuel at 767ºC over the course of 24 hours. These cells were then aged in air at room temperature for 18 days with several Raman scans collected over that period to characterize sulfur poisoning.

For Raman mapping, spectra were quickly collected from different spots on the sample with the laser at maximum focus. Sample movement was automatically controlled by the motorized XYZ stage. Specifically, the Raman system was programmed to obtain spectra at the intersections of a rectangular grid overlaying the area of interest with set intervals separating the intersections as shown in Figure 3.5. The spectra were centered around the Raman shifts corresponding to the modes of the wanted species or phases. Since the fully focused beam diameter was ~2 μm, the spectra were collected at 2-μm intervals.

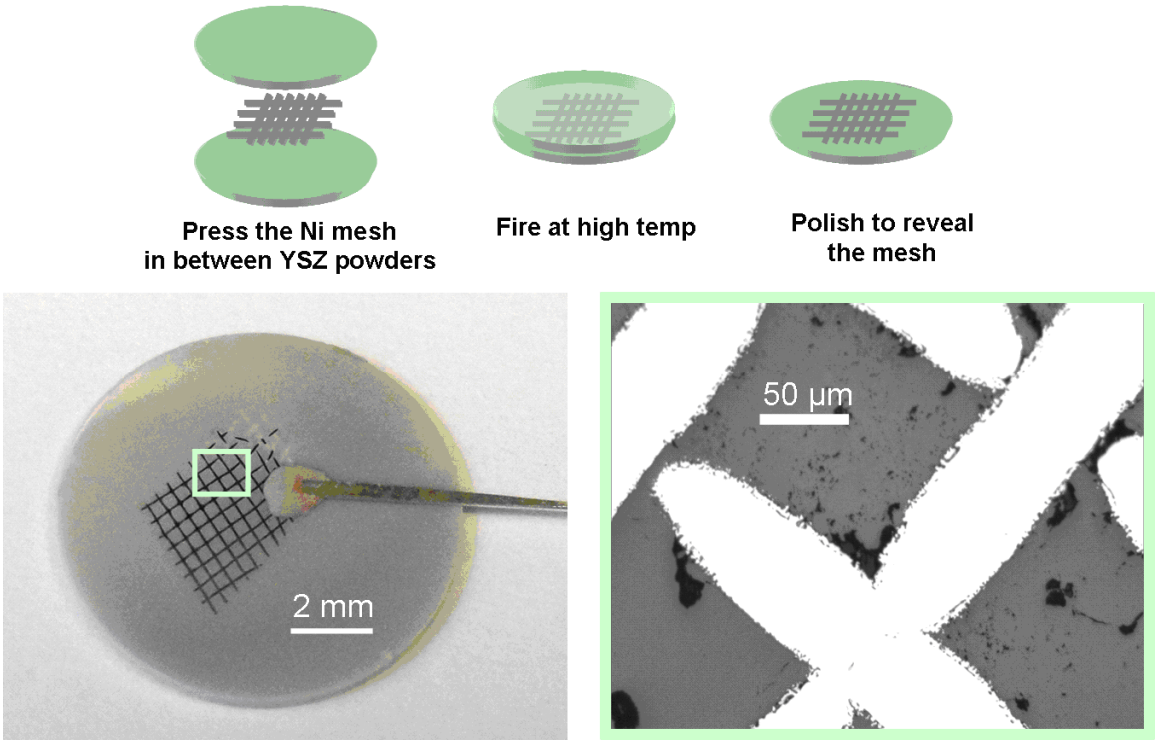

Figure 3.4. Illustrated steps for fabricating YSZ-embedded Ni mesh samples (top) along with a magnified photograph (bottom left) and optical micrograph (bottom right) of the sample.

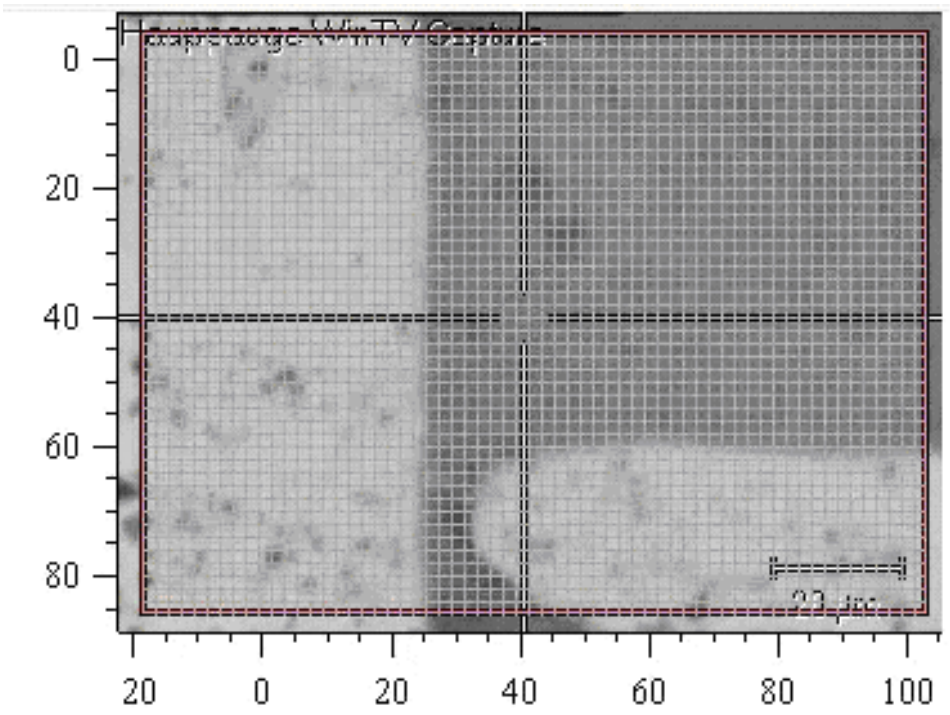

Figure 3.5. Optical micrograph of a YSZ-embedded Ni mesh samples with a Raman measurement grid overlay.

The YSZ pellets with strip-patterned Ni or Cu as well as those with embedded Ni mesh were used for *in situ* carbon deposition monitoring experiments. The former samples were heated in the chamber at 625ºC with flowing CH_4 gas for 12 hours, while the mesh samples were treated at 625°C in a flowing mixed gas containing 4% H_2, 5% C_3H_8, and 3% H_2O balanced by Ar for 15 hours. Raman signal was collected *while* the samples were held at high temperature.

3.5. Surface-enhanced Raman scattering (SERS) methodologies

Surface enhanced Raman scattering (SERS) techniques were used to enhance signal from analyzed surfaces. Mechanism details and results are described in Chapter 6.

3.5.1. SERS for cathode materials

For studying cathode material surfaces, LSM, and LSCF powders were first synthesized by a solid state reaction (SSR) method. Precursors for the SSR powders were ball-milled in ethanol with yttria-stabilized zirconia (YSZ) media for 24 hours. The mixed precursors were then calcined at 1050°C for 10 hours twice, with grinding and mixing following each firing. The resulting powders were uniaxially pressed into cylindrical pellets 10 mm in diameter using 3 tons of pressure. Pressed LSM and LSCF pellets were fired at 1350°C (LSM and LSCF). Finally, discontinuous Ag films were deposited on the pellet surfaces by sputtering in vacuum for a very short time (e.g. 10-30 seconds). A Si wafer piece was used as a control sample.

3.5.2. SERS for anode materials

For analyzing anode material surfaces with the help of SERS, $Ag@SiO_2$ core-shell nanoparticles were prepared. First, Ag nanoparticles were prepared by a polyol synthesis method similar to a previously published one.[76, 77] 0.1 g $AgNO_3$ and 1.5 g of polyvinyl pyrrolidone were dissolved in 6 mL ethylene glycol. The mixture was heated to 120°C for 1 hour. Afterwards, this Ag nanoparticle mixture was dissolved in 140 mL of ethanol with 4 mL of NH_4OH. 0.75 mL of tetraethylorthosilicate (TEOS) was injected in the solution while stirring. After 30 minutes of stirring, another 0.75 mL of TEOS was injected. The TEOS was used to create the SiO_2 shell around the nanoparticles.[77] Finally, the excess precursors were separated out by centrifugation, leaving behind $Ag@SiO_2$ nanoparticles suspended in ethanol. The nanoparticle suspension was applied drop-wise to a polished Ni foil coupon and allowed to dry in air overnight.

3.6. Bi-electrode supported solid oxide fuel cells

Information gained about coking tolerance from Raman experiments was applied towards modifying bi-electrode supported cell (BSC) anodes for improved performance. Details about this architecture and the results of experiments are described in Chapter 8.

3.6.1. Cell preparation

Circular YSZ BSC scaffolds (~40 mm diameter) that were prepared by the SOFC team at NASA GRC using freeze-casting methods similar to those reported previously[78] were used for this project. These scaffolds were used to prepare SOFC "slabs" to be cut into button cells for testing. A photograph of a typical scaffold prior to infiltration is shown in Figure 3.6; the pink coloration is due to a degradable red die that was used to test the electrolyte for pinholes. The anodes were prepared at GRC by first infiltrating one face of the YSZ scaffold with heavily concentrated $Ni(NO_3)_2$ (~8 *M* concentration) solution in methanol and modification solution. Three types of modifications were used: 3Ba-4Yb nitrate (0.5 *M* total metal ion concentration), 10Ba-1Zr-7Ce-1Y-1Yb nitrate (0.02 *M* concentration, BZCYYb composition), and 10Ba-9Zr-1Yb (0.03 *M* concentration, $BaZr_{0.9}Yb_{0.1}O_{3-\delta}$ or "BZYb" composition). These solutions were all homemade. For example, the BZCYYb solution itself was prepared by dissolving citric acid, EDTA, and an appropriate amount of zirconyl nitrate in a small amount of water (~5 mL). The target molar ratio for citric acid to EDTA to zirconyl nitrate was 15:10:1. After mixing this solution, ammonium hydroxide and nitric acid were slowly added and mixed into the solution until a clear solution with pH ~7-8 was obtained. The final solution was added drop by drop to the rest of the metal nitrate precursors (Ba, Ce, Y, Yb) and stirred overnight (>12 hours), resulting in a stable

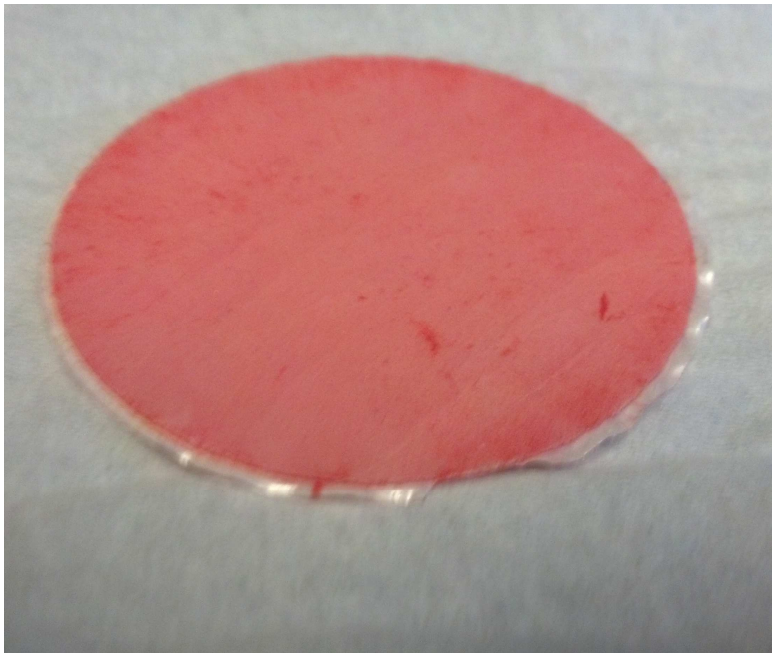

Figure 3.6. Typical YSZ BSC scaffold prior to infiltration.

transparent solution with very light yellow color. The preparation of the other two mixed nitrate solutions was similar.

For infiltration, the solutions were applied drop-wise to one face of the scaffold until visibly saturated. The scaffold was then heated up to 450°C on a hot plate over ~2 hours, held at temperature for 15 minutes, and then cooled down. Ni and modification solutions were alternately infiltrated six times each in this manner in order to establish an active electrode layer with a thickness of several µm. Ni-only cells were also infiltrated to be used as control samples. All sample slabs were heated to 1000°C for 2 hours to complete the conversion of the anode layer to its constituent oxides. Next, a heavily concentrated proprietary La-Sr-Co-Fe nitrate solution with appropriate stoichiometry to eventually form the perovskite $La_{0.6}Sr_{0.4}Co_{0.2}Fe_{0.8}O_{3-\delta}$ (LSCF) was infiltrated on the opposite face from the anode and heated to 450°C in order to create the cell's cathode.

This step was also repeated a total of 6 times. The completed cell slabs were heated again to 900°C to complete the conversion of the cathode layer to LSCF perovskite. Finally, while a blank Ni slab and a BZYb-modified slab were set aside to test as large cells by themselves, most slabs were cut into 1-cm button cells by a laser cutter. The resulting "glaze" left on the edges of the button cells from the extreme heat of the laser were ground away to prevent short-circuiting. Figure 3.7 displays a photograph of a typical cut button cell with the anode side facing up.

3.6.2. BSC performance and stability tests

Button cells were tested for performance and stability at using an apparatus like the one shown below in Figure 3.8. Coiled Ag wire was used as the current collector and attached to the anode using NiO paste and the cathode using Ag paste. The cell itself was mounted atop an alumina tube fixture with the anode facing into the tube so that it could

Figure 3.7. Typical BSC button cell with the anode side face-up.

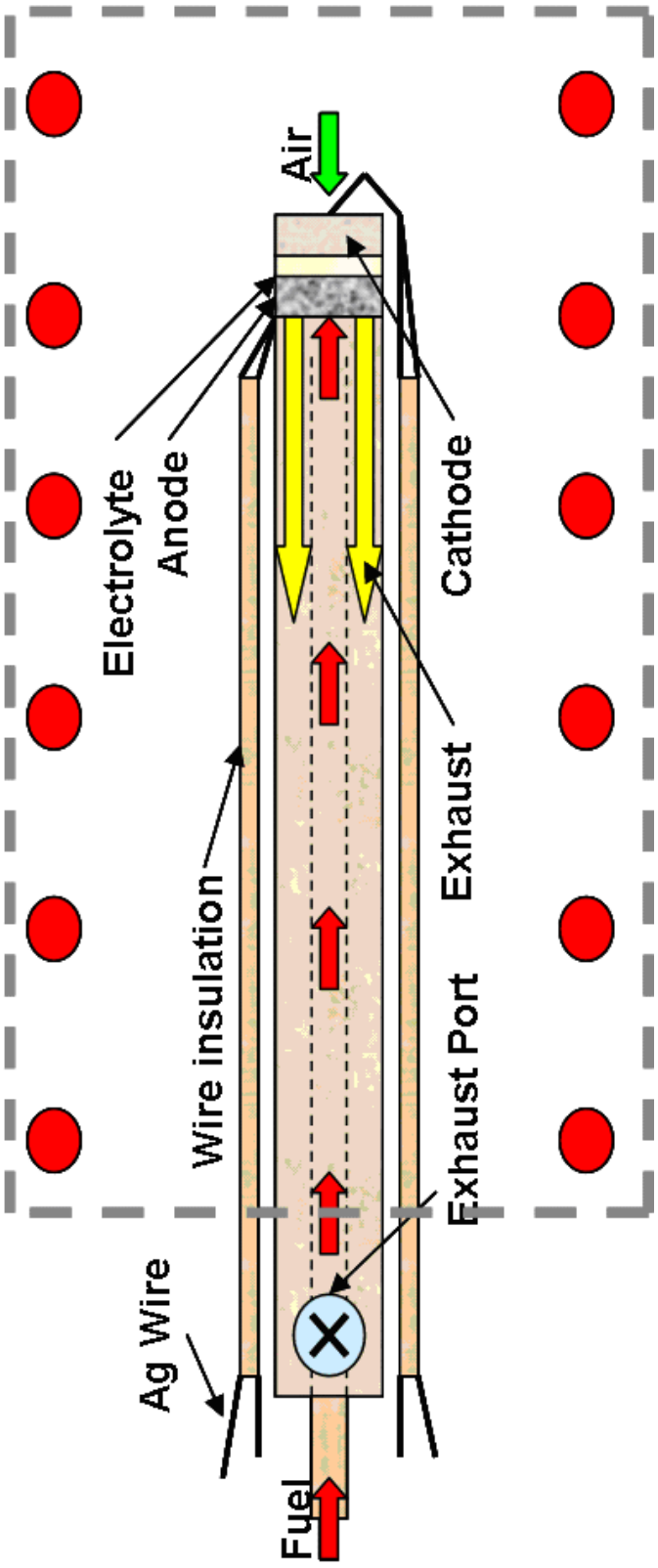

Figure 3.8. Schematic for performance and stability testing of button cells.

be sealed off at the edge from the air using Ceramabond (Aremco Scientific). A thinner tube running down the center of the mount tube acted as the fuel flow supply, while any exhaust exited out the bottom of the mount tube. The cathode was exposed to open air in order to supply oxygen to the cell.

Mounted cells were heated in a tube furnace up to 100°C, held for 1 hour, heated to 260°C, held for another 1 hours, and finally heated to 100°C. The first two heating steps were used to cure the Ceramabond. A 1°C/min. ramping rate was used during temperature increases. Once a cell had dwelled at 800°C for at least 2 hours, N_2 or Ar gas was allowed to flow through its tube fixture at 40 sccm for 15 minutes to flush the air out of the fixture. Next, the flowing gas was switched to H_2 for 1 hour to reduce the cell's anode. Following this step, testing was begun.

For the button cells, performance was tested at 600, 650, 700, 750, and 800°C by linear voltammetry using wet H_2 fuel (40 sccm, 3% vol. H_2O). A room-temperature water bubbler was used to supply humidity. Stability was tested by applying a constant current or voltage to the cell over time while supplying the anode with H_2, CH_4, C_3H_8, and/or H_2S gas. In the case of C_3H_8 gas, a very low flow (5 sccm) diluted with N_2 was used to prevent quick catastrophic failure of the cell as the gas is very prone to pyrolysis, which would clog the fuel gas supply tube with carbon and impede the fuel from reaching the anode. When H_2S gas was used for sulfur tolerance testing, the H_2S content on the gas flow was never more than 30 ppm. All of the aforementioned electrochemical testing was performed using an Arbin MSTAT potentiostat. The effective electrode area of these cells by which current density was calculated as 0.18 cm^2.

Performance and stability testing of the larger “full-slab” cells was performed at the NASA Glenn Research Center. Silver mesh was used as current collector for both electrodes and was attached using gold paste. A platinum wire was also attached near the outer part of the electrode to assist with current collection and function as the cell’s connection to the electrochemical testing equipment. The cells were sandwiched between two heavy 2-inch stainless steel plugs attached to gas feed pipes that formed the cell test assembly. The surfaces of the plug in contact with the anode side of the cell and the inside of the fuel gas inlet were coated with Cu by electroplating in order to attempt to prevent carbon deposition on those surfaces.

The large cell test assembly was mounted in a tube furnace. Figure 3.9 shows a photograph of the mounted assembly in with the furnace opened. The assembly was heated in the furnace with no gas flow to 40°C overnight to slowly dry the gold paste. Next, the temperature was ramped up to 400°C at 5°C / min; once this temperature was reached, dry compressed air was fed to the cathode side at 50 sccm while a wet 50/50 mixture of N_2 and H_2 fed to the anode at the same flow rate. Again, fuel was fed through a room-temperature water bubbler before reaching the cell. Ramping was continued at 5°C/min up to 800°C. During this time, the gas flow rate on each side was gradually increased and the anode side was made more fuel-rich. When the assembly reached 800°C, the anode was fed with 75 % H_2 / 25% N_2 at 400 sccm, and the cathode was flooded with compressed air at 1000 sccm. The system was allowed to equilibrate for 1 hour before any electrochemical testing was performed.

For performance testing, linear voltammetry was performed on the large cells at 800°C in H_2 and CH_4 fuels. For the latter case, 100% CH_4 was fed to the anode at 100

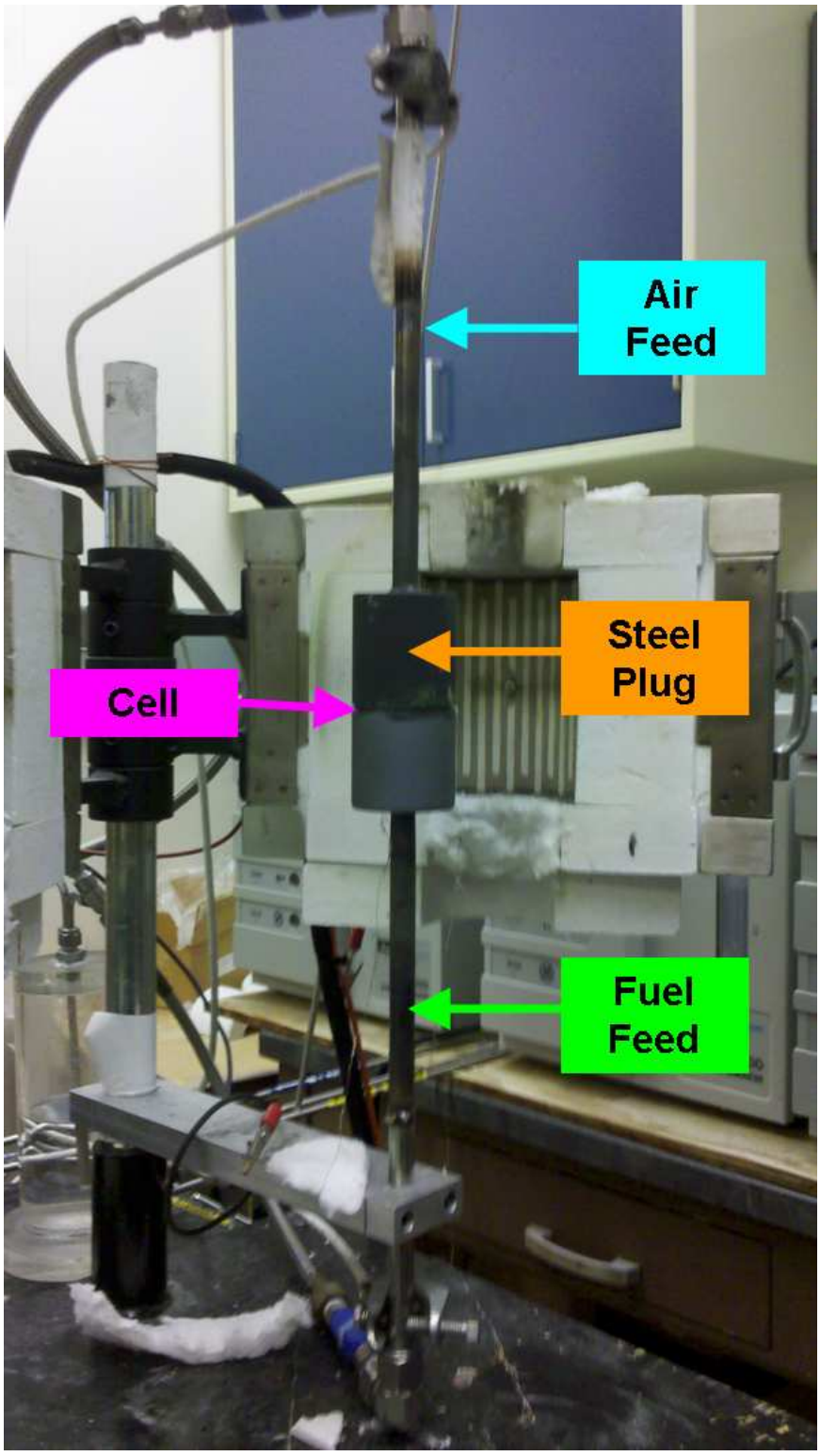

Figure 3.9. Photograph of the fuel cell rig used for testing large "slab" BSCs at the NASA Glenn Research Center.

sccm. The stability of the cells was tested in CH_4 at 800°C by holding the cells at constant current over time. Active electrode area was estimated as ~12.5 cm^2.

3.7. Other characterization

To help validate the findings of the various experiments outlined above, other conventional characterization methods were used. In the carbon deposition studies described in Chapter 5, scanning electron microscopy (SEM, Hitachi S800) and atomic force microscopy (AFM, Veeco Nanoscope IIIA) were employed for Ni surface characterization purposes.

For the SERS investigations described in Chapter 6, SEM was used to analyze the sputtered Ag substrates. Transmission electron microscopy (TEM, JEOL JEM) was used to characterize core shell nanoparticles.

In the portion of this work involving BSCs (Chapter 7), the modification solutions by themselves were evaporated following synthesis and calcined at 1000°C. The resulting powders were analyzed by X-ray diffraction and Raman spectroscopy to confirm their phases. Cell microstructure was examined by SEM (JEOL JSM) before and after operation, and Raman spectroscopy was used to assess cell degradation following operation.

CHAPTER 4: RAMAN SPECTROSCOPY OF BA-CONTAINING OXIDES

4.1. Structural analysis of BZCYYb

Ba-containing oxides have attracted interest for SOFC applications due to their potential for providing coking and sulfur poisoning tolerance[5-7]. In particular, $BaZr_{0.1}Ce_{0.7}Y_{0.1}Yb_{0.1}O_{3-\delta}$, or BZCYYb, has been shown to be a very effective anode material for running fuel cells on hydrocarbon fuels when combined with Ni. The structure of BZCYYb is thought to consist of a barium zirconate-cerate perovskite solid solution co-doped with Y^{3+} and Yb^{3+} cations at the B sites. Since Ce^{4+} is the majority cation in the B site, the material's crystal structure would most likely resemble that of $BaCeO_3$, which is an orthorhombic perovskite in the Pbnm space group[79]. Materials in this space group have 57 vibrational modes, and 24 of those are theoretically Raman-active. In contrast, $BaZrO_3$ is a cubic perovskite in the space group $Pm\bar{3}m$, and it has only 12 vibrational modes and 0 theoretical Raman modes[80].

Raman spectroscopy was used to help verify the structure of BZCYYb. Figure 4.1a shows a Raman spectrum that was collected from a typical BZCYYb powder. The sharp peaks located at 290, 316, and 335 cm^{-1} were assigned to BZCYYb, while the small peak at 460 cm^{-1} indicated a small amount of excess CeO_2 left over from the solid state reaction used to synthesize the powder[50, 71]. These results were compared to previous Raman-based studies of the structure of $BaCeO_3$.[79, 81] In these studies, the Ce^{4+} cations in $BaCeO_3$ were characterized as residing at "tilted" octahedral sites formed by the O^{2-} anions as illustrated in Figure 4.1b. Raman spectra collected from $BaCeO_3$ included three peaks at 307, 328, and 349 cm^{-1} that were similar in shape to those shown in the

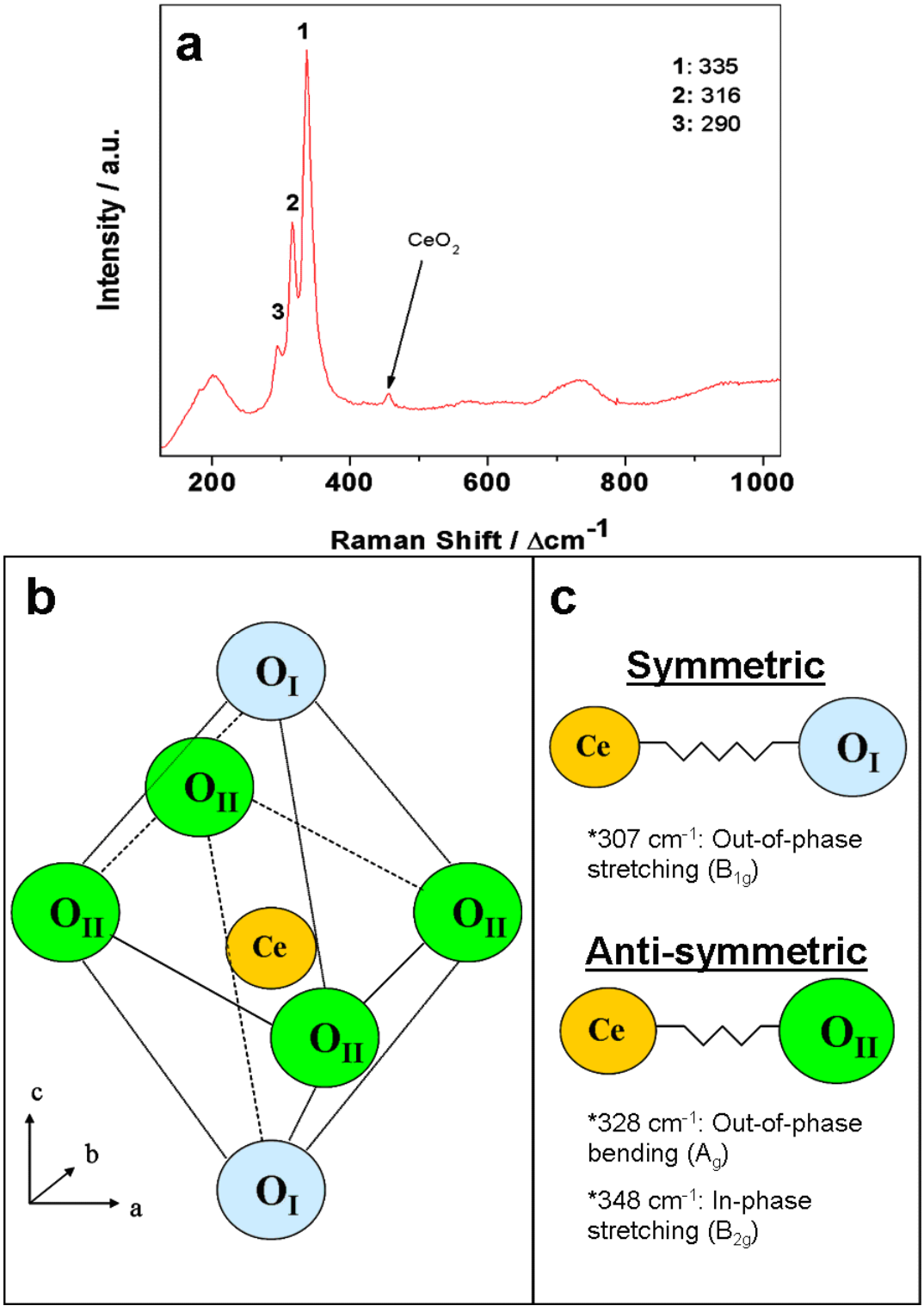

Figure 4.1. (a) Raman spectrum collected in air from typical BZCYYb powder. (b) Tilted octahedral site in $BaCeO_3$. (c) Vibrational mode assignments for peaks in a characteristic Raman spectrum obtained from $BaCeO_3$.

BZCYYb spectrum. Peak assignments are shown in Figure 4.1c; they correspond to various stretching and bending vibrations between the Ce^{4+} and O^{2-} ions. Unfortunately, the instrument configuration used to collect the BZCYYb spectrum could not access peaks below 200 cm^{-1}, where other phonon modes for this structure are found. Nonetheless, given the similarities between the $BaCeO_3$ and BZCYYb Raman spectra, one can infer that they have very similar structure; the B site ions are likely coordinated in the same fashion. The slight differences between the analogous Raman peaks are likely related to the dopants and substitutions in the B site of BZCYYb.

4.2. Water and OH groups on BZCYYb

Raman spectroscopy was used to probe for the presence of water on the surface of BZCYYb. A typical full-range spectrum from a sintered and polished BZCYYb pellet surface is shown in Figure 4.2. The band located at 344 cm^{-1} corresponds to the Raman modes discussed above; the three peaks all broadened slightly following sintering, seemingly merging. The 650 cm^{-1} band is a second-order harmonic of the first band[54]. The peak at 210 cm^{-1} and the set of modes between 2750 cm^{-1} and 3650 cm^{-1} (inset of Figure 4.2) correspond to OH modes inherent to the material. Previous studies suggest that the characteristic OH-bond stretching vibration modes appear in this regime.[82-84]

4.2.1. In situ detection of water on BZCYYb

Raman spectra were collected from BZCYYb powder at different times over the course of exposure to flowing wet Ar gas (~3 v% water) in the Raman environmental chamber at room temperature, where incorporation of water into the bulk phase of BZCYYb was unlikely because of limited bulk diffusion. Figure 4.3A displays those

spectra. The BZCYYb powder sample was first dried at 400°C under evacuation for 10 hours to remove water from the sample. Upon exposure to wet (3 v% H_2O) argon at room temperature, the mode centered near 3310 cm^{-1} appeared quickly, while the mode near 3580 cm^{-1} emerged more slowly over time. The presence of the modes in the 3100-3700 cm^{-1} range, particularly the mode that peaks near 3580 cm^{-1}, was strongly indicative of multi-layered surface water molecules, as modes at higher wave-numbers correspond to subsequent layers of water with weaker hydrogen bonds.[85] Thus, one possible explanation for this behavior is that a strongly bonded layer of water accumulates at the surface quickly in a wet atmosphere, while subsequent layers of water build up more slowly. These features are notably absent for the sample exposed to dry gas. Spectra collected in situ from samples held under the same gas conditions at 500ºC display similar features and contrast (Figure 4.3B).

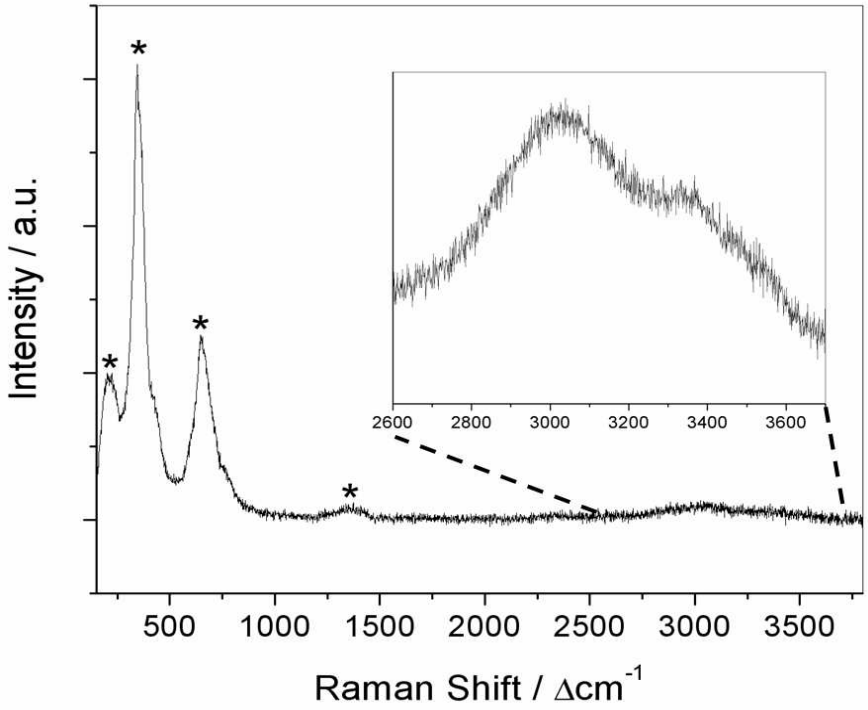

Figure 4.2. Typical Raman spectrum collected from a polished and sintered BZCYYb pellet surface in air.

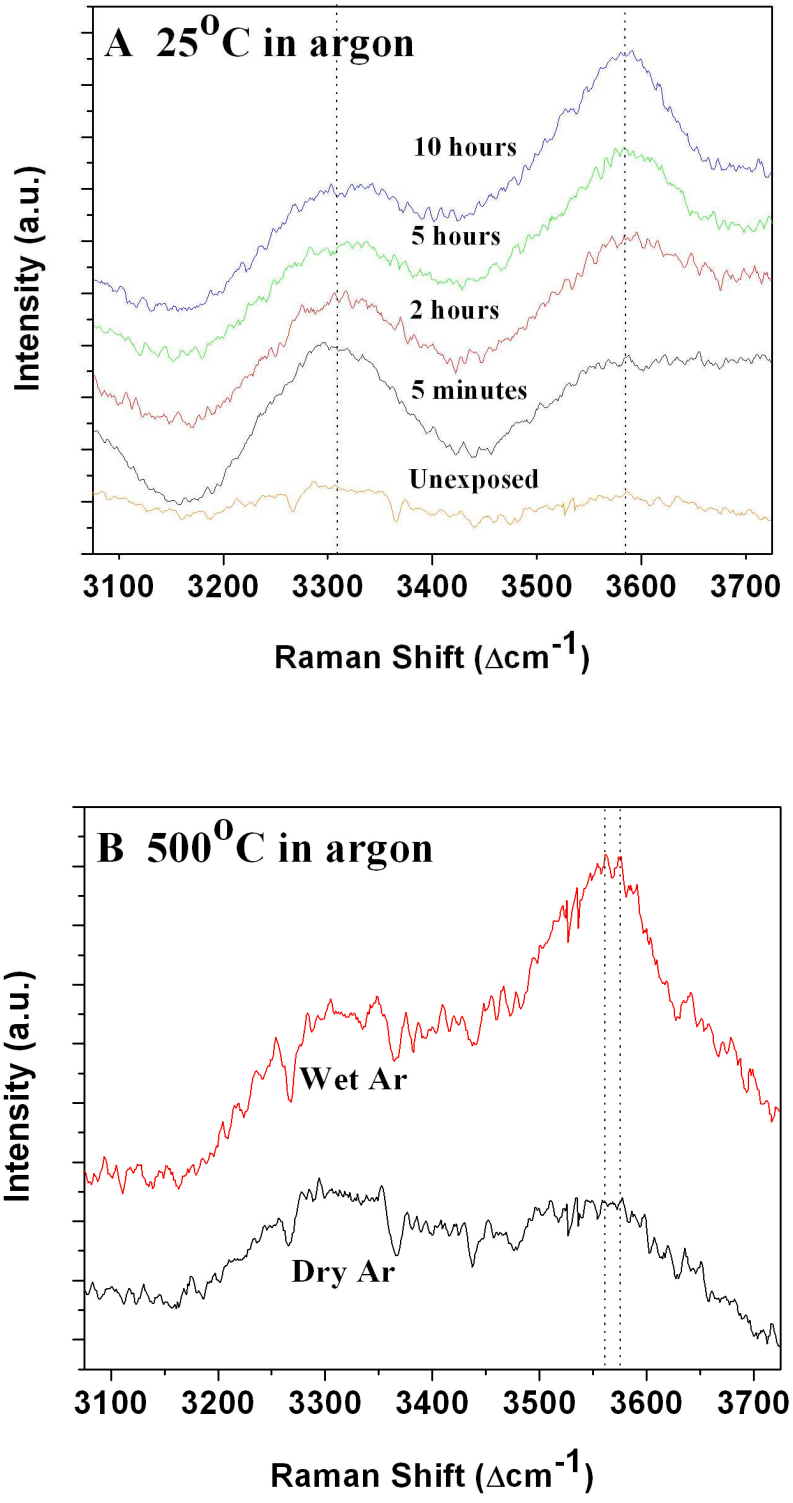

Figure 4.3. *In situ* Raman spectra collected from BZCYYb sample (A) at room temperature under wet Ar gas at various exposure times and (B) at 500°C in dry and wet argon.

4.2.2. Electrochemical in situ spectroscopy of species on BZCYYb

In situ analysis was employed to characterize changes in concentrations of OH groups on BZCYYb under conditions that included electrochemical stimuli. For these initial *in situ* experiments, spectra were collected at room temperature in a flowing gas atmosphere consisting of 3% H_2O and 4% H_2 balanced by Ar. A bias voltage of -0.7 V was applied to the BZCYYb pellet sample using the sputtered Ag electrode on the exposed BZCYYb pellet face, a porous Ag counterelectrode on the opposite face, and lead wires connected to a potentiostat.

Different positions on the BZCYYb surface with respect to the sputtered Ag electrode were probed. Figure 4.4a shows an optical micrograph of the vicinity of the interface between the sputtered Ag electrode and the uncovered BZCYYb surface. The spots that were probed are marked in this image. Lower cm^{-1} range Raman spectra obtained from these spots are displayed in Figure 4.4b along with a typical spectrum collected from the BZCYYb while no bias is applied. As can be seen, the characteristic BZCYYb peaks did not vary considerably with position or bias; however, the peak at 210 cm^{-1} was observed to be slightly more intense at the measured spot closest to the electrode, indicating greater concentration of OH groups in this region. It should be noted that Raman spectra in general did not vary with position when no bias was applied.

Figure 4.4c shows the higher wavenumber range of Raman spectra obtained in the same fashion. For this wavenumber range, the chamber conditions introduced a significant background signal, so this “noise” was subtracted from each of the measured spectra. As a result of this treatment, the no-bias spectrum had essentially zero signal. In contrast, under bias, the signal in this range increases with proximity to the Ag electrode,

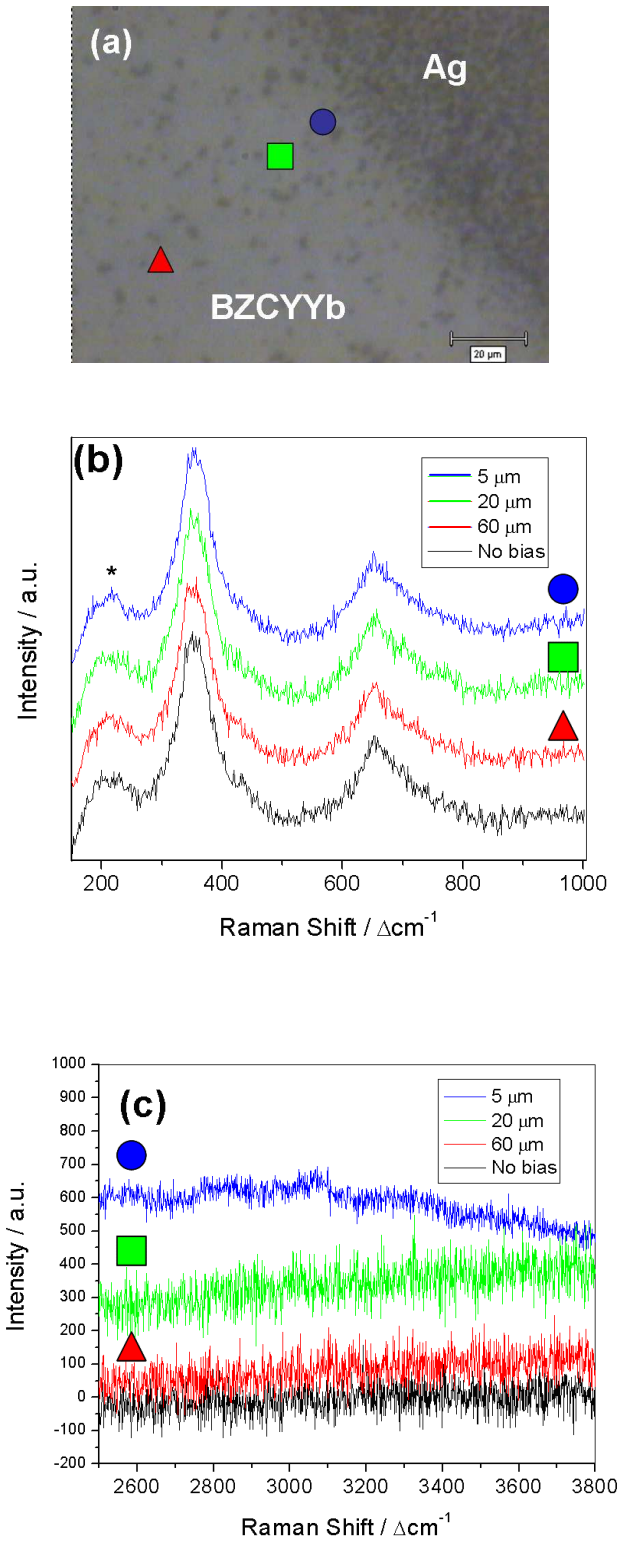

Figure 4.4. (a) Optical micrograph of Ag/BZCYYb interface with Raman measurement and (b,c) Raman spectra collected from marked spots under wet reducing atmosphere and -0.7 V bias.

again indicating an increase in OH concentration close to the electrode.

Finally, the BZCYYb sample was heated to 500ºC under the same flowing gas. Interestingly, according to the Raman spectrum collected near the interface of the Ag and BZCYYb, carbon became present on the surface of the Ag electrode (Figure 4.5, top spectrum). This electrode was attached to the wire using Ag paste, so it is possible that the organic material in the paste was not fully eliminated before the experiment. This material may have pyrolized and left behind some carbon on the silver electrode. When a -0.7 V bias was applied, however, the Raman signal associated with carbon[65] decreased (Figure 4.5, bottom spectrum), indicating that the carbon was driven off the surface, likely with assistance from the nearby BZCYYb. Since the applied electrochemical stimulus was responsible for the carbon removal observed in this case, the mechanism for carbon removal may bear similarity to the water-remediated coking tolerance mechanism in an actual fuel cell anode that contains BZCYYb. These preliminary results indicate that more systematic experiments along this vein might be worthwhile.

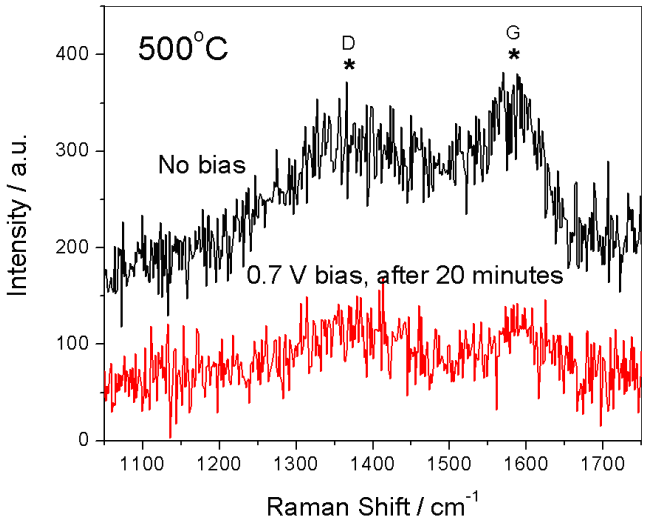

Figure 4.5. Raman spectra obtained near the interface of the Ag electrode and BZCYYb at 500ºC in flowing 4% H_2 / 3% H_2O / bal. Ar gas with/without an applied -0.7 V bias.

4.3. Raman analysis of water on BaO-modified Ni anodes

Water uptake behavior was also confirmed by Raman spectroscopy on BaO-modified Ni powders. Presented in Figure 4.6a are Raman spectra obtained from plain Ni and BaO-modified Ni powders in wet flowing H_2. The peak near 1600 cm^{-1}, corresponding to the bending mode of water[84], is observed on the Raman spectra collected from the BaO/Ni sample, but absent on that from a pure Ni exposed to wet H_2. Figure 4.6b shows the upper range of Raman spectra collected from a typical BaO/Ni sample in wet and dry atmospheres; the broad mode between 3450 and 3700 cm^{-1} on the spectrum from the BaO/Ni sample exposed to wet H_2 indicates the presence of water with weak hydrogen bonds that is likely on the surface of the sample.[82] In contrast, these spectral features disappeared when the same sample was exposed to dry H_2, further confirming the water uptake capability of the surface layers.

DFT calculations performed with the assistance of Dr. Yongman Choi at Brookhaven National Laboratory were used to validate the Raman measurements. A modeled BaO/Ni surface is illustrated in Figure 4.7. For this system, the calculations confirmed that a H_2O bending mode ($\upsilon_{w,b}$) exists at 1594 cm^{-1}, while two stretching modes (υ_{h1} and υ_{h2}) of adsorbed OH species on BaO are at 3368 and 3716 cm^{-1}, respectively.

Given that the presence of both H_2O and OH groups on BaO-modified Ni was demonstrated both theoretically and experimentally by Raman spectroscopy, water likely adsorbs on the surface both molecularly and dissociatively. The latter case allows for formation of intermediate species like COH that can help elimination of carbon from the anode surface. More details on theoretical calculations can be found in Yang *et al.*[6]

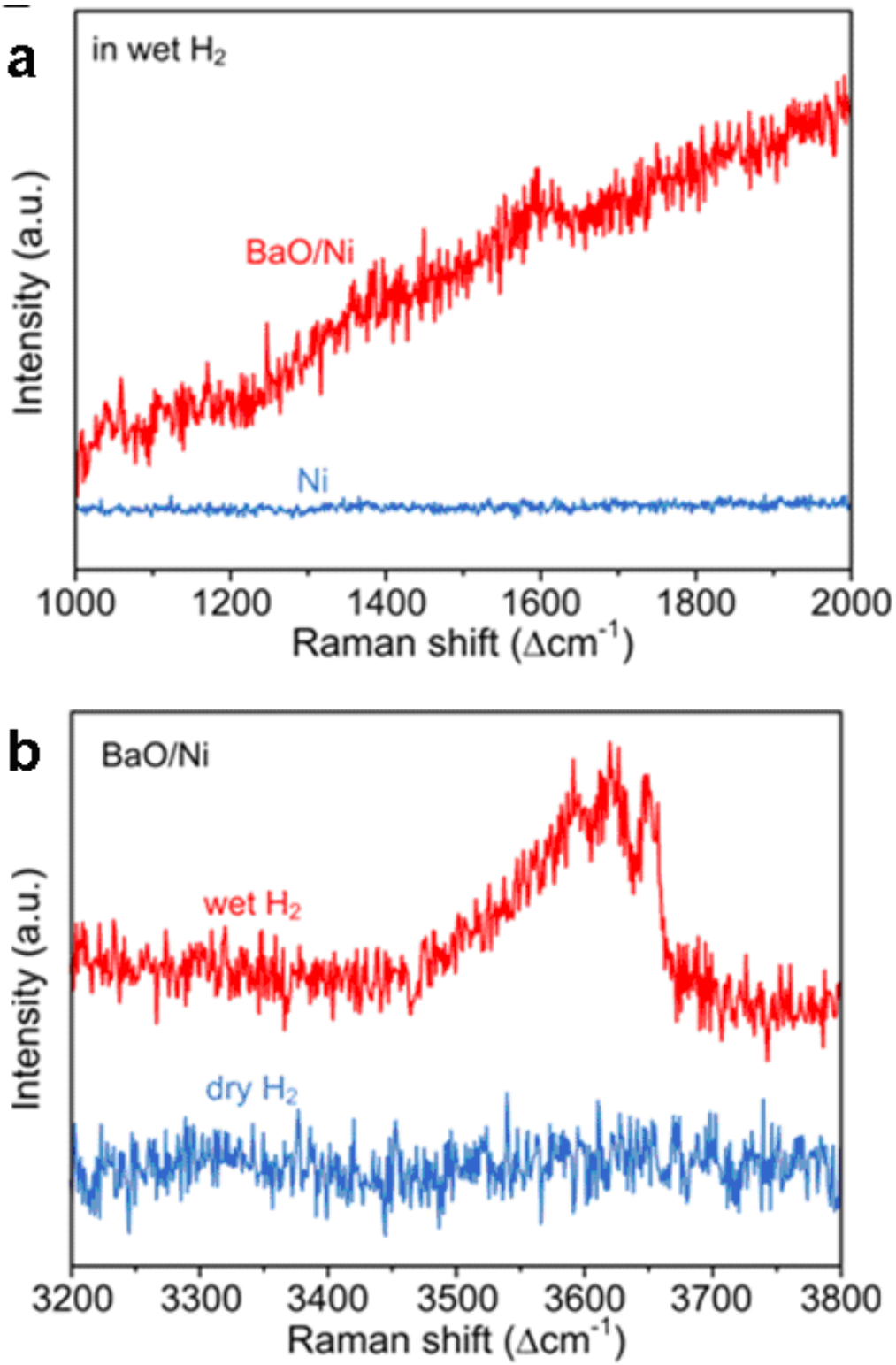

Figure 4.6. (a) Raman spectra collected from BaO/Ni and pure Ni samples in wet H_2 (with ~3 v% H_2O) atmosphere at room temperature. (b) Raman spectra collected from BaO/Ni samples in dry and wet H_2 (with ~3 v% H_2O) atmospheres at room temperature.

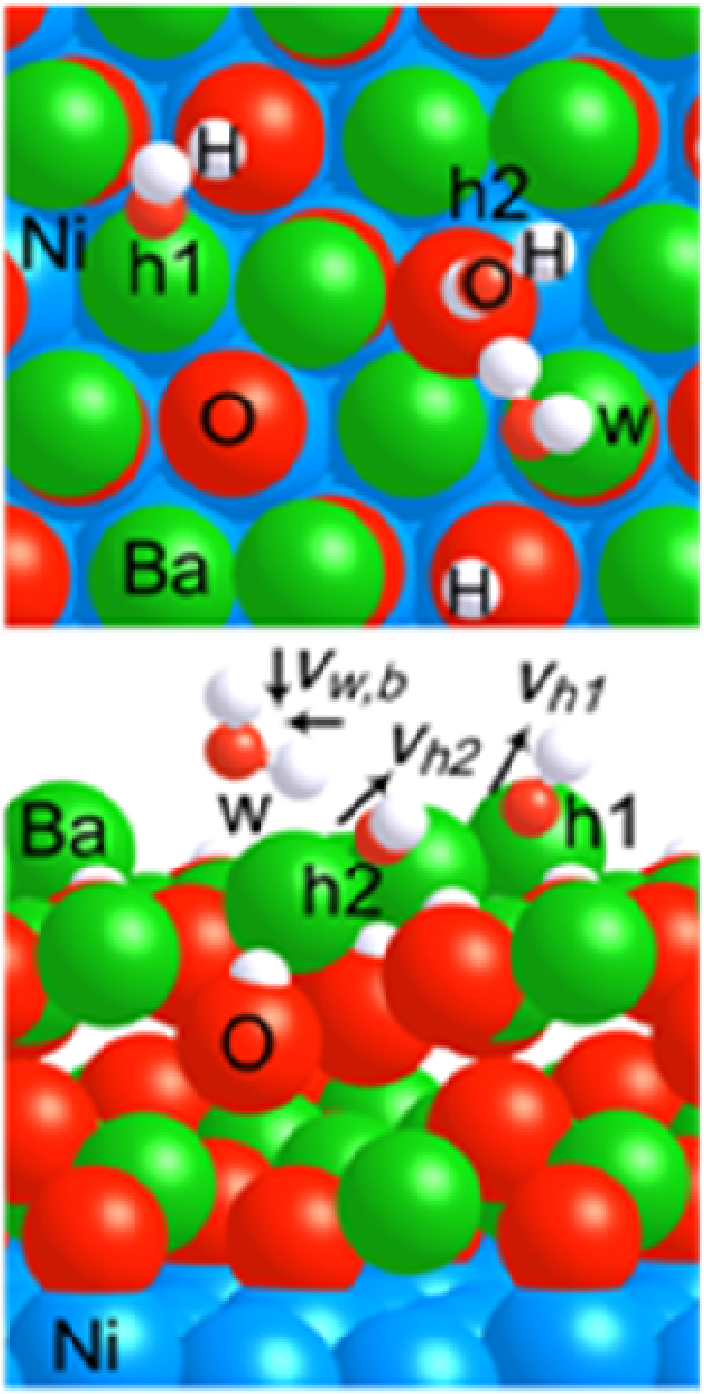

Figure 4.7. Top and side views for the interaction of H_2O on two-layer BaO deposited on p(3×3) Ni(111) containing 6 Ba and 6 O atoms. "W", "h1", and "h2" represent molecularly adsorbed H_2O and dissociated hydroxyl species, while $\nu_{w,b}$, ν_{h1}, and ν_{h2} are the vibration modes of H_2O bending and two OH stretching (1594, 3716, and 3368 cm^{-1}), respectively. Large balls in Brandeis blue, green, and red are Ni, Ba, and O of BaO, respectively, while small balls in red and white are O from H_2O and H, respectively.

4.4. Raman spectroscopy of $BaZr_{1-x}Y_xO_{3-\delta}$

Similar to BaO nanoparticles, recent work has demonstrated that the inclusion of a thin film of $BaZr_{1-x}Y_xO_{3-\delta}$ (BZY) on the surface of YSZ in a Ni-YSZ anode leads to excellent coking tolerance. BZY has also shown water adsorption properties akin to the other Ba-containing oxides discussed so far. Shown in Figure 4.8 are typical Raman spectra taken from pure BZY ($BaZr_{0.8}Y_{0.2}O_{3-\delta}$) and YSZ powders after treatment in wet Ar (3 vol. % H_2O) with 4 vol. % H_2 at 750°C for 4 hours. Clearly, a band that peaks near 3575 cm^{-1}, assigned to OH-stretching modes, was present in the BZY powder, indicating strong water and OH adsorption on the BZY surface. In contrast, no water adsorption was present in the YSZ powder. Looking further down the Raman spectra of BZY, a peak at 1625 cm^{-1} assigned to a water bending mode was present under wet gas, while this peak disappeared upon 2 hours of heat treatment at 600ºC in dry atmosphere, indicating desorption of water (Figure 4.9). Further, DFT calculations performed using a model BZY surface indicated a high preference for both molecular and dissociative adsorption of water.

For reference, Figure 4.10 shows the typical spectrum for BZY powder in the lower cm^{-1} range under both wet and dry atmospheres. The characteristic features for BZY identified by others[86] can be observed in both of these spectra. Although BZY is in the space group $Pm\bar{3}m$ and has no theoretical Raman modes, the peaks observed are likely the result of defects induced by the doping of Y into the Zr sites. Since the spectral features are the same in each case in this range, the material likely has good chemical stability under both atmospheres.

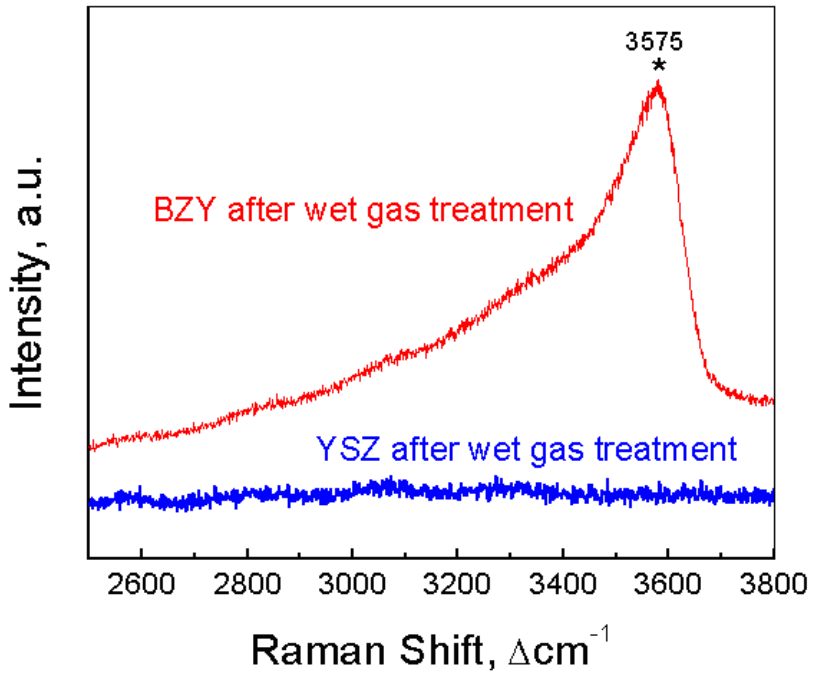

Figure 4.8. Raman spectra collected from BZY and YSZ powders following treatment in wet 4% H_2 / bal. Ar.

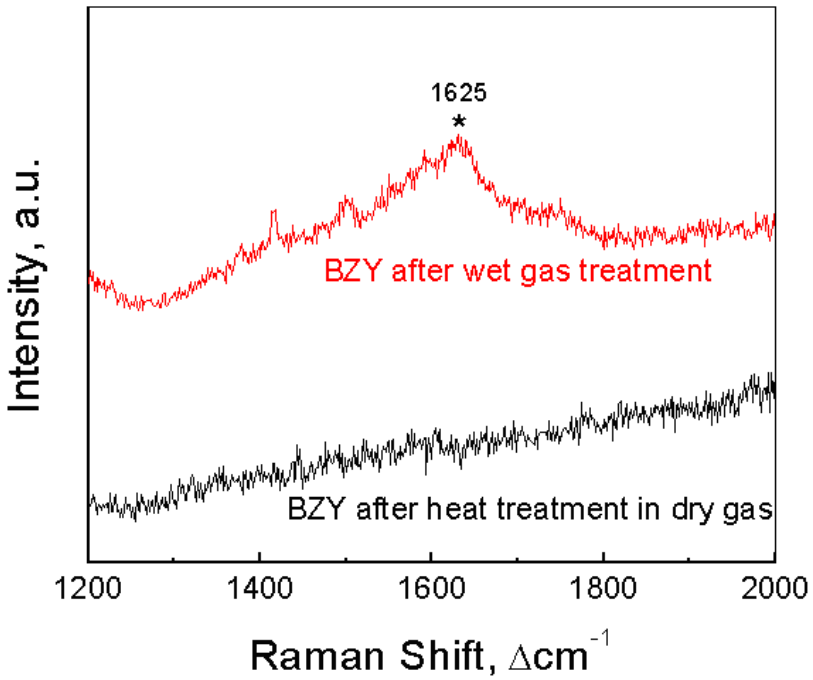

Figure 4.9. Raman spectra collected from BZY and YSZ powders following treatment in wet 4% H_2 / bal. Ar.

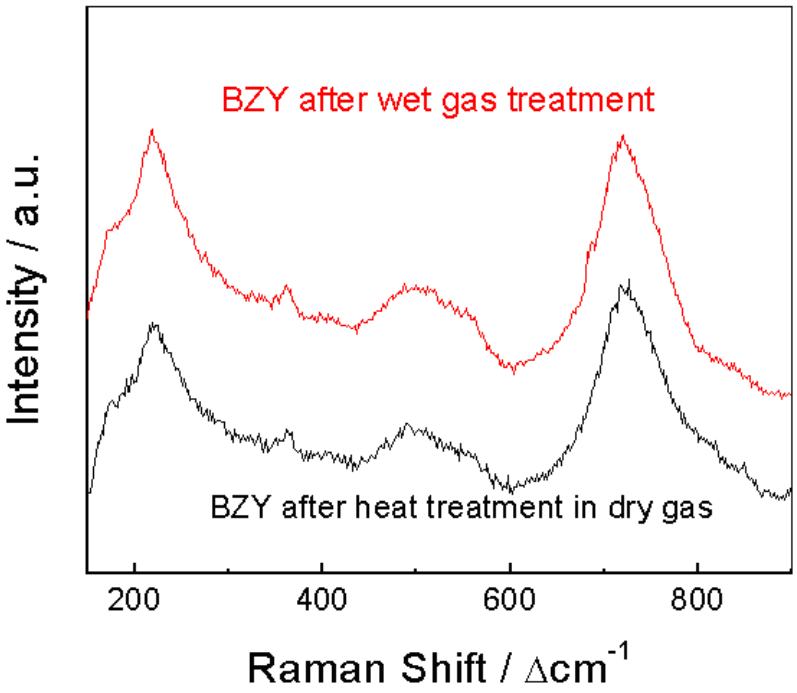

Figure 4.10. Characteristic Raman spectra obtained BZY following wet gas treatment and dry heat treatment.

4.5. Findings and outlook

The investigations summarized in this chapter suggest that the connection between the various Ba-containing oxides that add coking tolerance to SOFC anodes is water adsorption. Further, Raman analysis was demonstrated as a useful tool for characterizing these types of materials and their water uptake behavior. Therefore, Raman spectroscopy is likely a viable way of screening anode modifications that would potentially convey coking and sulfur poisoning tolerance based on their water adsorption capability. In subsequent chapters, the Raman spectroscopy's capability to examine these degradation behaviors more directly is also examined.

CHAPTER 5: RAMAN ANALYSIS OF COKING AND SULFUR POISONING

5.1. Coking and sulfur poisoning tolerance in SOFC anodes

As was mentioned previously, supplying SOFCs with hydrocarbon fuels poses many problems for systems using state-of-the-art material specifications, such as ceramic-metal composites (cermets) of Ni and yttria-stabilized zirconia (YSZ). Ni, the most common active component of anode materials used for SOFCs and for reforming of hydrocarbon fuels, is very prone to carbon deposition on its surface, or "coking."[8, 87] Even supplying a conventional Ni-anode SOFC with the low-order hydrocarbons (*i.e.* CH_4 and C_3H_8) contained in natural gas tends to result in very aggressive coking with blocking of active reaction sites and quick anode performance degradation when the temperature is high enough.[5, 8] In addition, single-digit ppm level H_2S contamination within in the fuel has been shown to cause a performance drop of well over 10% within the cell.[20]

To make SOFCs truly fuel-flexible and candidates for more effective power systems, the issues of anode coking and sulfur poisoning tolerance need to be addressed. Anode materials and structures beyond traditional cermets have been explored by SOFC researchers to this end. Recently, a new material, $BaZr_{0.1}Ce_{0.7}Y_{0.1}Yb_{0.1}O_{3-\delta}$ (BZCYYb), was reported to provide the anode with excellent tolerance to coking and sulfur poisoning under SOFC operating conditions in the presence of moisture.[5]

Other alternatives with appreciable coking tolerance, such as $(La,Sr)TiO_{3-\delta}$,[88, 89] $Sr_2(Mn,Mg)MoO_{6-\delta}$,[90] liquid Sn,[91] and Cu-based[21, 22] anodes have been proposed as well. In addition, conductive ceramic oxides incorporated into the anode like

$La_{0.75}Sr_{0.25}Cr_{0.5}Mn_{0.5}O_3$[92] and $Gd_2Ti_{1.4}Mo_{0.6}O_7$[93] have shown promising sulfur tolerance. Unfortunately, the chief problems facing their applicability to fuel cell systems lie in physical, chemical, and thermal incompatibilities with state-of-the-art YSZ electrolyte, relatively high cost, and lower overall catalytic performance. On the other hand, efforts have been made to improve the degradation tolerance of more conventional Ni-YSZ by modifying the surface of Ni with nanostructured "islands" of BaO [6] and Y-doped $BaZrO_3$ coatings.[7]

Some questions remain on how such modification conveys coking and sulfur poisoning resistance to the anode. For example, in the case of the BaO nanoparticles, one hypothesis revolves around the considerable affinity of BaO for water. According to DFT calculations performed for this material[6], nanoscale particles of BaO are capable of water adsorption. The adsorbed water can subsequently dissociate and form hydroxyl groups which may migrate to the Ni surface and assist in removing carbon from the Ni surface that is deposited by the cracking or pyrolysis of the hydrocarbon fuel. An improved understanding of this tolerance mechanism, such as knowledge of how and where the carbon deposits on the Ni electrode surface and how far away from the nanostructures the carbon removal effect happens, is vital to a more optimized design of coking-tolerant anodes. Obtaining such information requires direct observation and quantification of the carbon as it deposits on the anode surface under relevant operating conditions. Raman spectroscopy is ideally suited for gathering this information. In particular, the sensitivity of Raman spectroscopy to carbon species and its ability to distinguish between different forms of carbon bonding has been established quite well up to this point.[65, 94-98]

5.2. Raman spectroscopic investigation of degradation in SOFC anodes

Walker et al. first developed and demonstrated a Raman microscopy system that was capable of *in situ* detection of coking on Ni-YSZ anodes.[97-99] Since then, others have adapted this methodology for similar investigations.[19] In addition, surface-enhanced Raman methods have been used to further increase the sensitivity of Raman spectroscopy to carbon on anode surfaces.[100]

To truly understand degradation and tolerance mechanisms related to carbon and sulfur for SOFC anodes, the ability to effectively *map* the location and form of the deposited specie with adequate spatial resolution is needed. Yoshinaga et al. demonstrated *ex situ* Raman mapping of carbon on Ni.[101] Pomfret, Owrutsky, and co-workers have developed near-infrared thermal imaging techniques for monitoring coking-related degradation in SOFCs operated on alkane and alcohol fuels.[99, 102] In addition, Cheng, Dong, and co-workers recently applied Raman spectroscopy to the study of sulfur poisoning[68, 69, 103]. The goal of the current work is to expand upon this information even further by improved mapping and monitoring of species deposited both *ex situ* and *in situ* on Ni-based anodes with and without surface modifications by novel methods. For comparison purposes in the coking investigation, Cu anodes were also evaluated. Cu anodes have been shown to be much less active towards coking than Ni.[22]

5.3. Raman mapping of coking on pure Ni surfaces

Ni coupons were used to study how coking varies over a polycrystalline Ni surface. For a larger portion of this investigation, electrodes having well-defined boundaries with YSZ electrolyte material were employed to resolve phase boundaries.

Microscale patterned Ni and Cu strips that were deposited on YSZ substrates using photolithography methods[74, 75] as well as Ni mesh embedded in YSZ served these purposes. *In situ* experiments were performed using the environmental chamber designed for direct Raman analysis of samples under high temperature and fuel gas atmosphere. This study puts some emphasis on studying coking on Ni-based SOFC anodes from low-order alkane fuels, namely CH_4 and C_3H_8.

Figure 5.1 displays a portion of a typical Raman spectrum collected *ex situ* from a heavily coked spot on a Ni coupon following exposure to C_3H_8-containing gas at 550ºC. Over the 1200-1750 cm^{-1} region, the spectrum contains three primary features at 1357 cm^{-1} ("D-band"), 1585 cm^{-1} ("G-band"), and 1617 cm^{-1} ("D'-band"). The G-band corresponds to C-C stretching that is common to all sp^2-bonded carbon, while the D-band and D'-band features reflect disorder in the structure of the deposited carbon.[65] Raman features related to the D-band were the focus of the *ex situ* mapping studies; although the G-band was at times the spectral feature of greater intensity, some samples contained YSZ, whose characteristic Raman spectrum contains a broad peak in the same wavenumber range as the G-band when collected at room temperature. A corresponding spectrum for "uncoked" Ni is also shown, although it is featureless due to lack of active Raman modes in Ni metal itself.

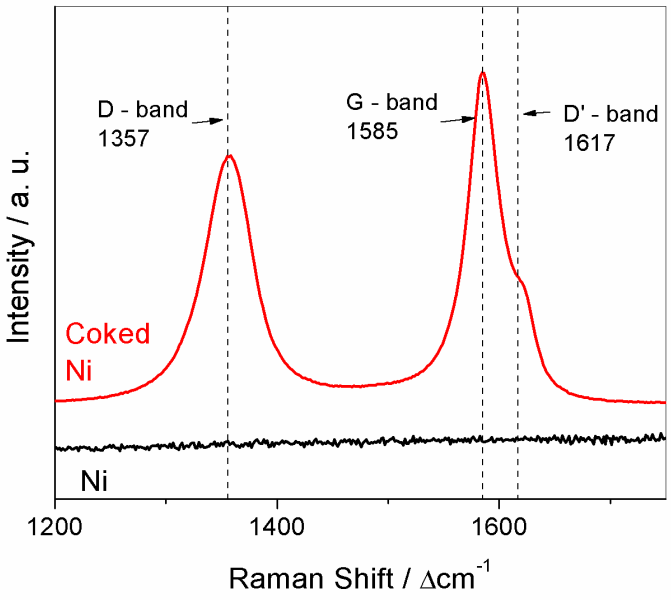

Figure 5.1. Typical Raman spectrum collected in air from a spot on the surface of a Ni coupon before (black trace) and after exposure to C_3H_8-containing gas at 550°C (red trace). The spectral band assignments highlighting characteristic carbon features are indicated by the arrows.

Presented in Figure 5.2a is an optical micrograph of a ~100 μm-wide area on the surface of the same Ni coupon along with a Raman intensity map for the carbon D-band of the same area (Figure 5.2b). Example spectra from a few of the mapped spots are shown in Figure 5.2c. From the optical micrograph, varying areas of discoloration with loose black particles in some places can be seen on the Ni surface, suggesting different levels of coking within the imaged area. The corresponding Raman map was plotted using a ratio of the integrated intensity for the D-band (area under 1250-1445 cm^{-1}) and the background signal. A direct correlation between higher carbon D-band intensities and higher levels of discoloration can be observed from the map and micrograph, indicating that the Raman mapping is a viable semi-quantitative indicator of how the carbon distribution varies across the Ni surface. This capability is important for understanding

coking and the corresponding tolerance phenomena since knowing where the carbon deposits gives clues about the relevant mechanisms.

These results indicate that initial coking was not homogeneous across the nickel surface. By examining different areas of the surface using scanning electron microscopy (SEM), we found clear grain boundaries that appear to separate regimes of carbon deposition, which was indicated by areas of dark discoloration (Figure 5.2d). Since this nickel coupon is polycrystalline and grains with different orientations will exhibit different crystal planes when they are polished, it is most likely that the heterogeneity in coking levels originated from varying propensities for carbon deposition across different crystal planes. A similar relationship between crystal plane orientations and coking tendencies was reported previously.[104] Finally, the micrograph in Figure 5.2d also shows that coking within some grains formed discontinuous, non-solid-colored patterns. Since the sample examined had been exposed to C_3H_8 for a relatively short time, the patterns observed might be related to the initial appearance and growth of carbon nuclei in favorable locations.

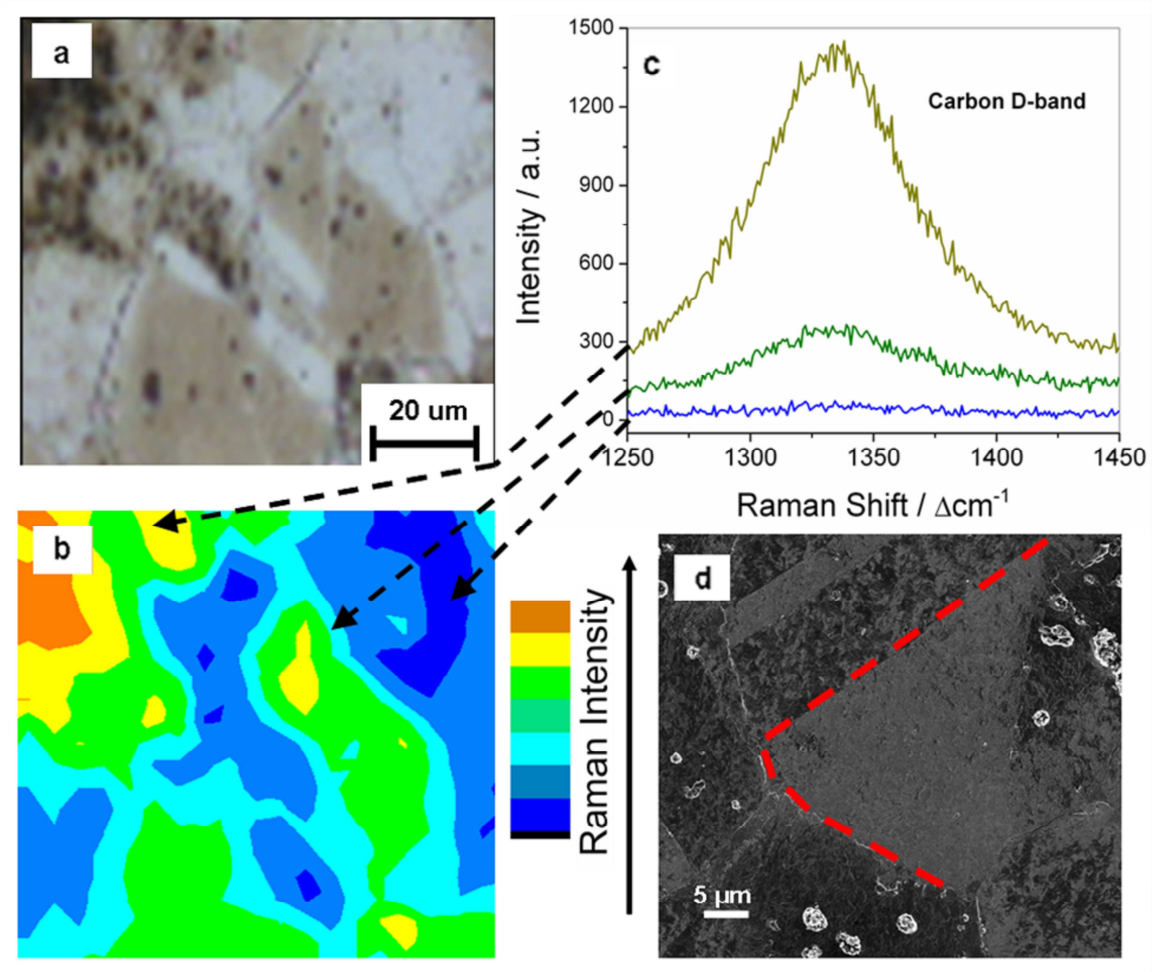

Figure. 5.2. (a) Optical micrograph of a Ni coupon after exposure to C_3H_8-containing gas at 550°C along with (b) a map of carbon D-band Raman intensity (integrated from 1270 – 1445 cm^{-1}) collected from the same area. **(**c) Actual spectra from selected spots of the map. (d) SEM micrograph of the same Ni coupon. Note that some of the grain boundaries are indicated by dotted red lines.

Besides the contrasts shown in optical image, SEM and Raman mapping, coking also produced morphological distortions on the polycrystalline nickel surface. For example, Figure 5.3a displays an image of the polished and cleaned Ni coupon surface prior to any other treatments. In most areas, the surface had a smooth texture although a small number of polishing media particles missed by the cleaning step can be seen. In the smooth areas, topographic variation was 10 nm, as measured by cross-sectional analysis of the AFM image (Figure 5.3b). The Ni surface morphology was changed considerably by carbon deposition, even in areas where coking was not severe. Figure 5.3c shows a high-magnification SEM image of a lightly coked area on a Ni coupon exposed to C_3H_8-containing gas at 550°C for 5 minutes. The surface was roughly textured in comparison to the untreated Ni. In addition, AFM images over the same area revealed nanoscale dot features (see inset in Figure 5.3c). These features likely represent the sites of initial carbon nucleation. The same analyses performed on a heavily coked area showed an even rougher surface texture (Figure 5.3d). In this case, much larger granules were observable in the AFM image.

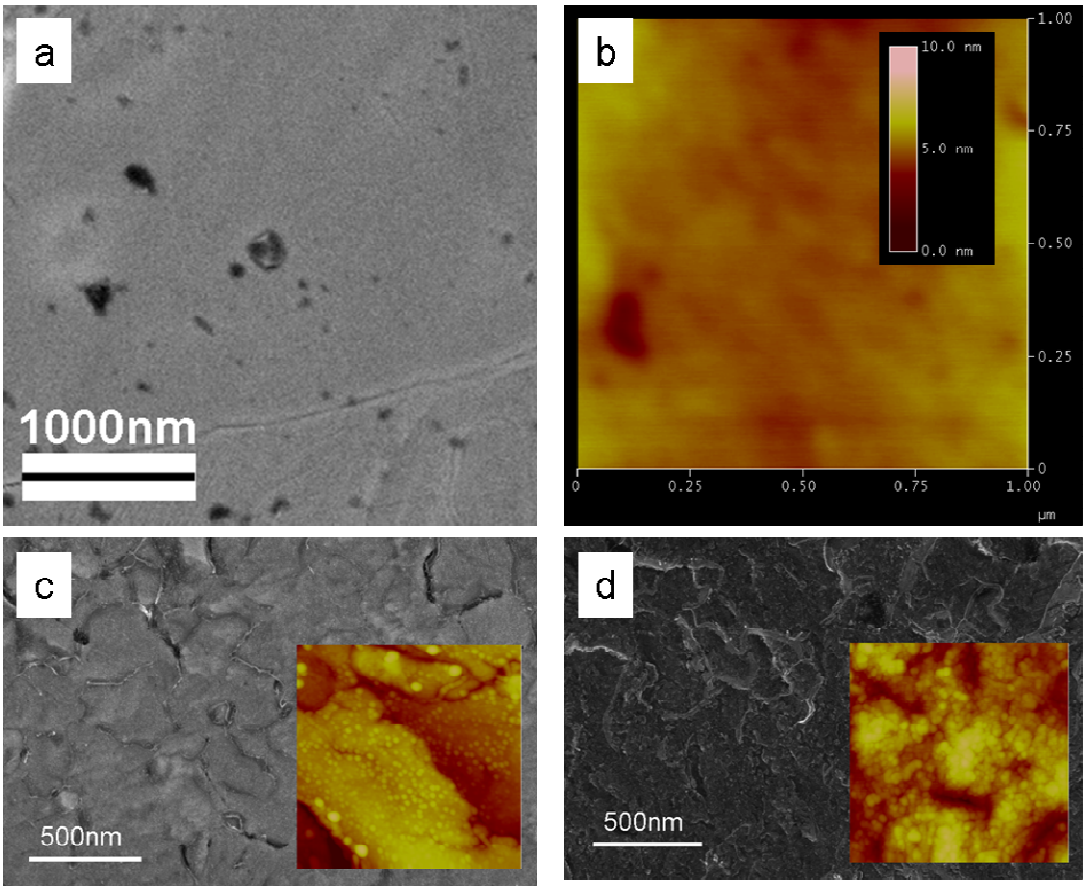

Figure 5.3. (a) SEM image of the surface of a polished Ni coupon. (b) AFM image of a typical area on the surface of a polished Ni coupon. (c,d) SEM images of a lightly coked region and a heavily coked region (respectively) of the Ni coupon after exposure to C_3H_8-containing gas at 550°C. The insets are AFM images of the same regions.

5.4. Coking variation across Ni-YSZ surfaces

On the other hand, of greater interest to those in the field of SOFC research is where and how carbon actually deposits during coking processes in multi-phase or composite anodes which contain Ni. To address this issue, electrodes with well-defined boundaries *vis-à-vis* YSZ substrates[52, 68] were used in this work. Figure 5.4a shows an example micrograph of patterned Ni strips on YSZ. The darker strips are the Ni phase and the lighter areas are exposed YSZ substrate. The widths of the Ni strips were ~10-15 µm, while the distances between the strips varied from and 15-30 µm, respectively.

Figure 5.4b displays the same area after exposure to C_3H_8 gas at 625°C for 2 hours. The Ni strips turned completely black from carbon deposition on the surface. Figure 6.4c provides a higher magnification of some of the coked strips. A Raman map of the area shown in Figure 5.4c was collected for the carbon D-band (Figure 5.4d). The D-band intensity was much higher along the Ni strips, indicating that carbon preferentially deposited on Ni and that the YSZ surface experienced little or no coking. This finding supports the notion that a heightened susceptibility of Ni to coking is the main cause of related degradation problems.

While the information gleaned from the *ex situ* experiments is certainly interesting, similar findings have been reported by others in previous studies[96, 101]. Furthermore, one could have reached the same information by more conventional surface methods like electron spectroscopies. The true advantage of Raman spectroscopy and mapping lies in the possibility of *in situ* analysis of SOFC anodes; specifically, the technique can be used to probe and map anode surfaces under cell operating conditions.

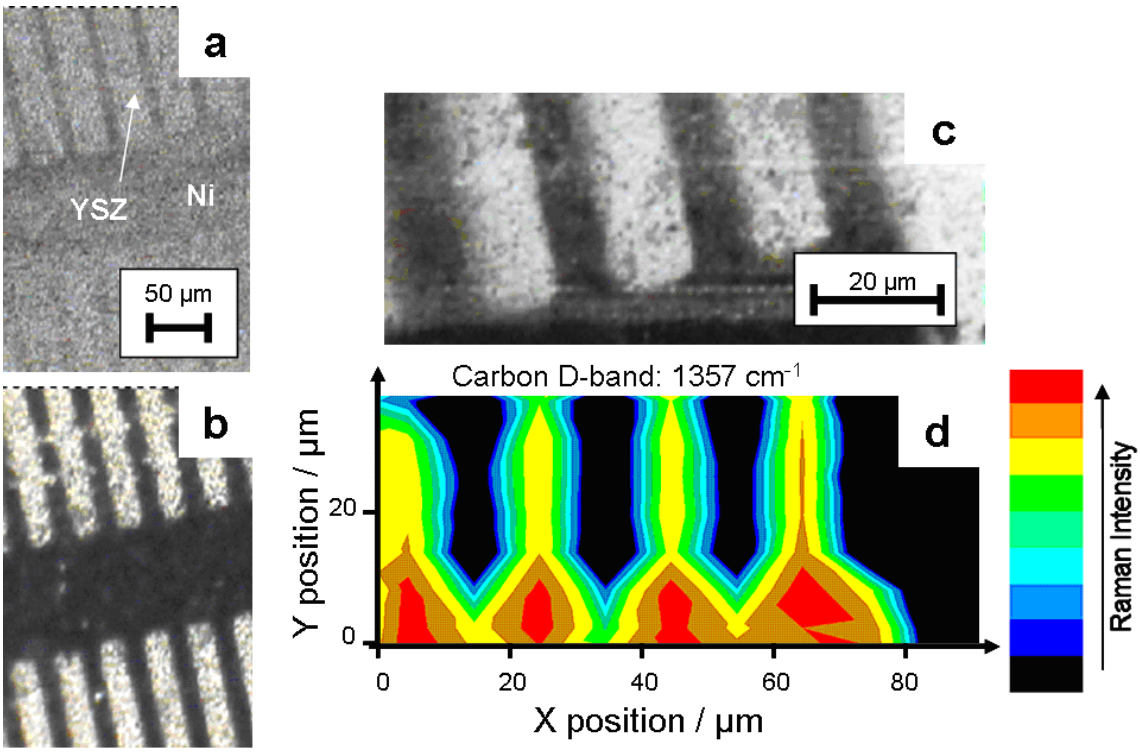

Figure 5.4. (a) Optical micrograph of strip-patterned Ni electrode deposited on YSZ substrate; the same Ni electrode is shown in (b) following severe coking caused by exposure to C_3H_8 at 750°C for 2 hours. (c) Higher magnification of coked Ni electrode, with (d) showing a Raman map of the same area for the carbon D-band.

5.5. *In situ* Raman mapping of carbon deposition

For the current *in situ* Raman work, the Ni and Cu electrodes were directly analyzed *during* exposure to typical CH_4 or C_3H_8 fuel gases at high temperature in an environmental chamber. To demonstrate the Raman spectroscopy's ability to spatially map carbon deposition under *in situ* conditions, a strip-patterned Ni electrode was analyzed while exposed to CH_4 at 625°C in the environmental chamber. After 12 hours of exposure, a map of the integrated intensity in the 1200-1700 cm^{-1} range was collected from the area marked in Figure 5.5a. The integrated intensity from this range includes the D-band, G-band, and D'-band. Comparing the spectrum in Figure 5.1 with its analog in

Figure 5.5b, the high analysis temperature led to notable broadening of the Raman features, reduction in intensity, and increased background noise from more thermal vibrations. These spectral changes limited the amount of available Raman signal, so the entire range was used instead of a single Raman mode in order to maximize success in detecting total amount of carbon. In addition, these factors also reduced the image resolution as compared to *ex situ* experiments. Fortunately, as can be seen in these spectra, the YSZ band near 1600 cm^{-1} was not so prominent at high temperature; the suppression of this band makes the deconvolution of the carbon signal into its constituent bands, and therefore identification of the forms of carbon present, an easier task.

Moreover, as Figure 5.5b shows, relevant signal was detected almost exclusively from the Ni surface, indicating that coking preferentially occurs there. This observation is supported by SEM imaging over the same area that was performed after cooling down and removing the sample from the chamber. As shown in Figure 5.5c, nodule-shaped particles were only visible on the Ni surface. These particles were not present on the Ni surface before exposure to CH_4 and were thus likely related to carbon deposition. The particle deposition pattern appeared to be discontinuous, and the particles themselves were only 10-100 nm in size.

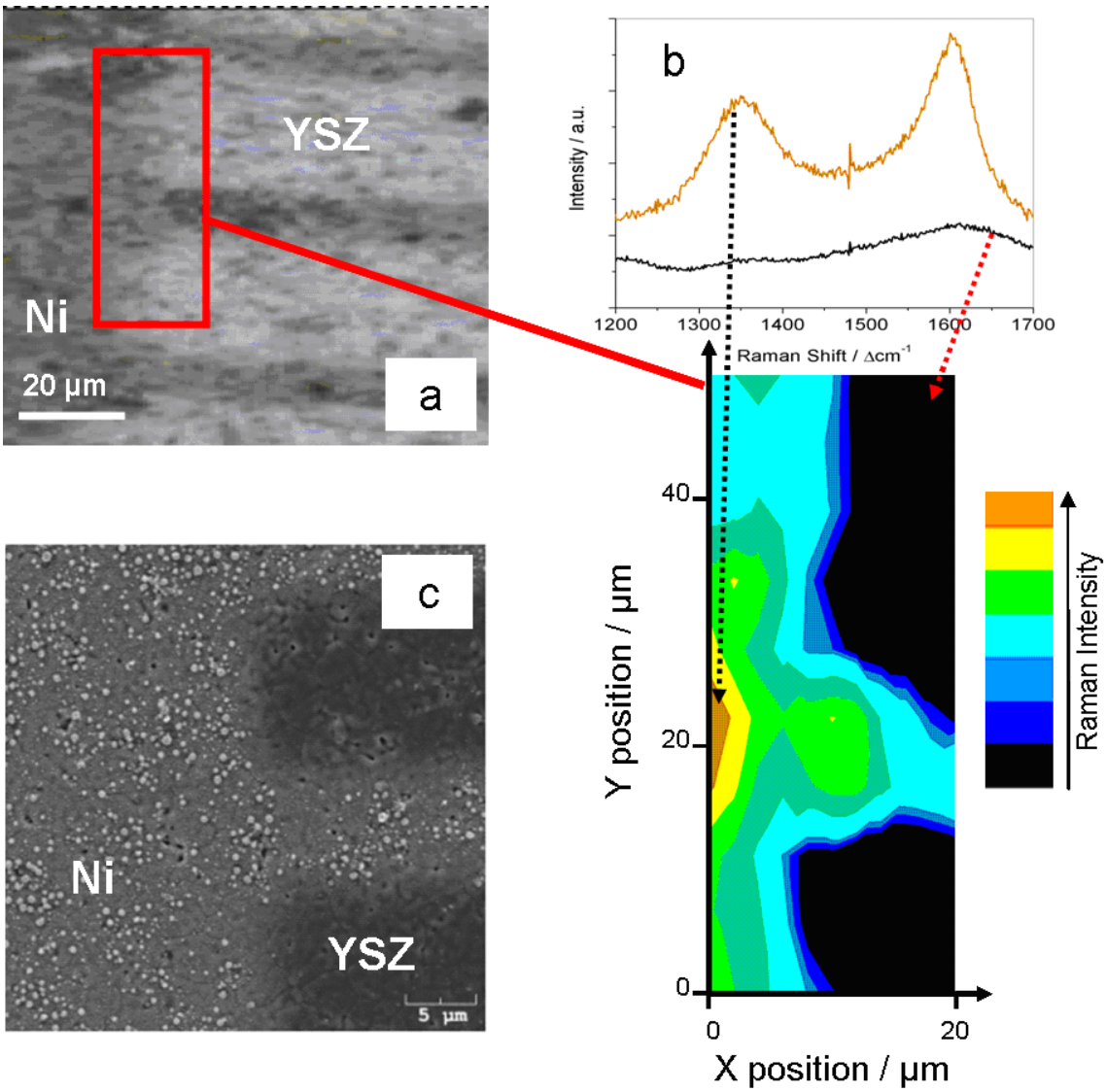

Figure 5.5 (a) Optical micrograph of strip-patterned electrode exposed to CH_4 gas at 625ºC. (b) Raman spectra and intensity map of total carbon signal collected *in situ* from the area marked in (a) at the 12-hour mark during CH_4 exposure. (c) SEM image of the patterned electrode following CH_4 treatment.[105]

The same atmosphere and temperature treatment was also applied to YSZ pellets with Cu electrodes, and Raman spectra were collected *in situ* from the Cu surface (Figure 5.6). Cu was chosen for comparison due to its lack of strong catalytic activity towards carbon formation. No distinct features above the background can be observed in the spectrum obtained right before CH_4 exposure, and the one taken at the 12-hour mark during exposure shows only the slightest amount of carbon signal. As expected, the acquired spectra confirmed that carbon formation does not occur on Cu as aggressively as it does on Ni under the same conditions.

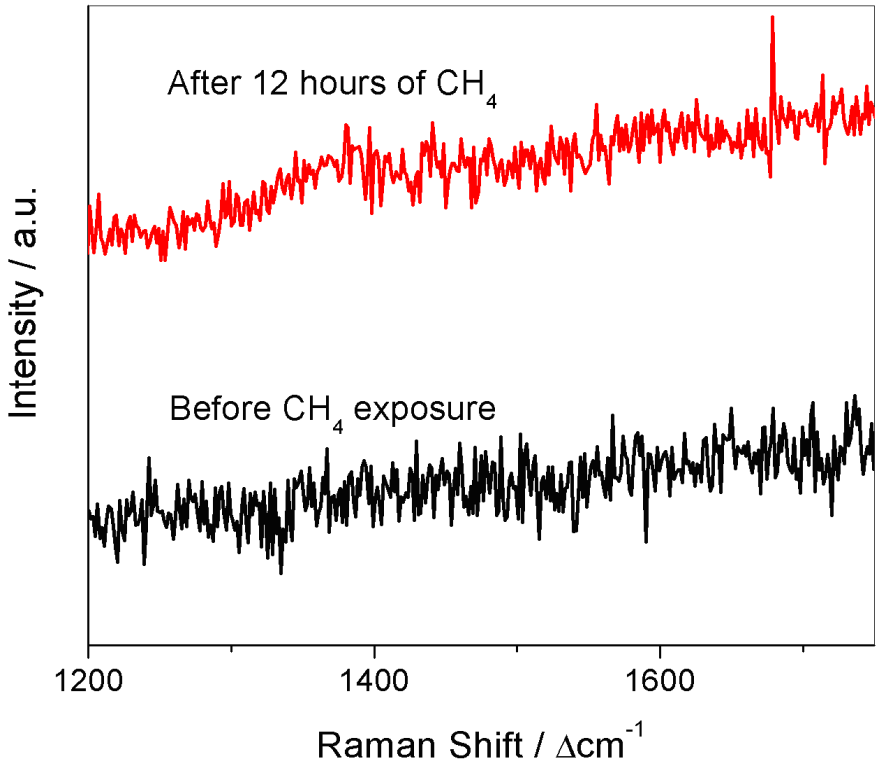

Figure 5.6. Raman spectra collected from the surface of a Cu electrode while heated at 625°C before and after exposure to CH_4.

5.6. *In situ* Raman monitoring of carbon deposition

For subsequent demonstrations of the capability of Raman spectroscopy for *in situ* monitoring of carbon deposition at specific microscale electrode sites over time, Ni mesh electrodes embedded in YSZ were used in lieu of the strip-patterned electrodes. While the strip-patterned electrodes served as an ideal test bed for an initial fundamental demonstration of the ability to map deposited carbon on anode surfaces, the mesh electrodes would ultimately be more suitable for serving as functional anodes that could be simultaneously characterized by Raman spectroscopy methods and electrochemical testing; the mesh samples are easier to fabricate by conventional ceramic processing and would allow for more efficient current collection. Efforts towards coupling electrochemical SOFC tests with the Raman techniques outlined here, while not covered in this work, are ongoing.

For *in situ* experiments involving the monitoring of carbon deposition on Ni mesh electrodes, C_3H_8-containing gas was used instead of CH_4 to provide a more aggressive test of coking resistance. The gas was bubbled through water before entering the chamber in lieu of electrochemically producing the water at the electrode. Finally, the Ni mesh was modified with BaO using methods very similar to those described in Yang *et al.*[6] in order to promote water adsorption of the anode and directly evaluate its effect on coking tolerance.

Figure 5.7a displays an optical micrograph of an unmodified Ni mesh electrode at 625°C in reducing atmosphere (to prevent undesired Ni oxidation) directly before introduction of C_3H_8. After C_3H_8 began flowing into the chamber, spectra were collected periodically from a spot on the surface of a sample of Ni mesh. This spot is marked by

the green dot in Figure 5.7b, which shows the mesh after 15 hours of wet C_3H_8 exposure at 625°C. Some extent of the damage to the mesh caused by coking can be seen in the micrograph by itself. Nonetheless, Raman spectra collected from the Ni mesh and YSZ substrate (Figure 5.7c) once again demonstrated that a carbon signal was only detectable on the Ni surface; the spectrum from the substrate showed only YSZ features.

A plot of the change in relative carbon signal intensity over the first few hours of exposure time is shown in Figure 5.8. The intensity of the carbon signal increased as carbon built up on the surface of the Ni from coking. The amount of detectable carbon signal eventually leveled off after a few hours, which was likely due to the thickness of the deposited carbon on the Ni exceeding the penetration depth of the Raman excitation.

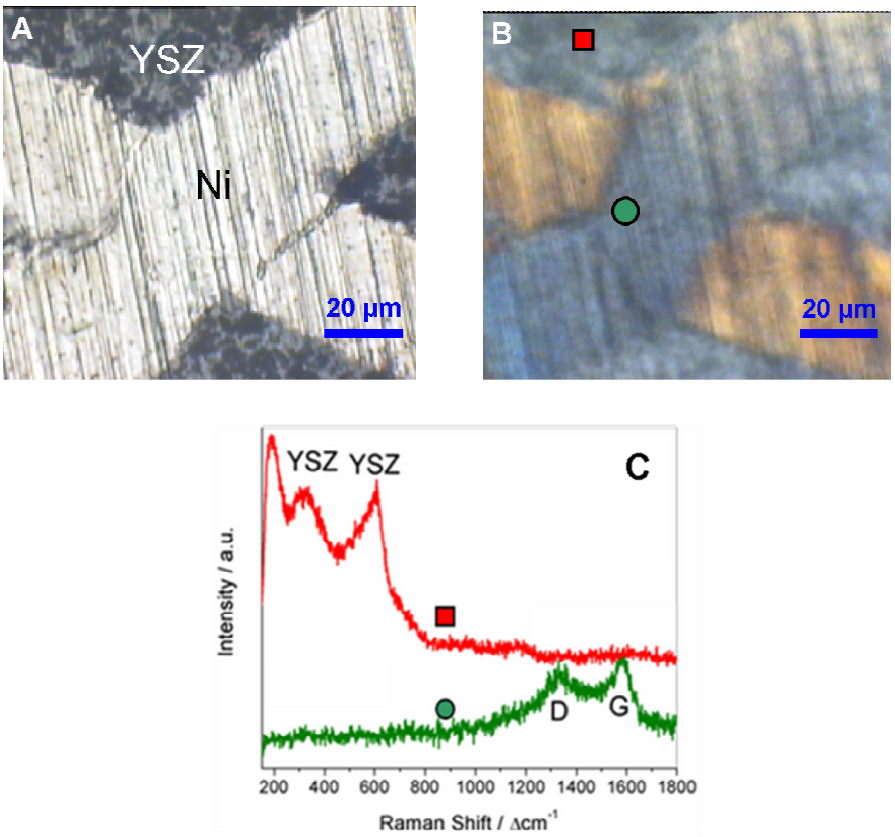

Figure 5.7. (a) Optical micrograph of Ni mesh embedded in YSZ. (b) Same embedded Ni mesh after exposure to C_3H_8-containing gas at 625ºC for 15 hours. (c) Raman spectra collected i*n situ* from the spots marked in (b) at the 15-hour mark of C_3H_8-containing gas exposure.

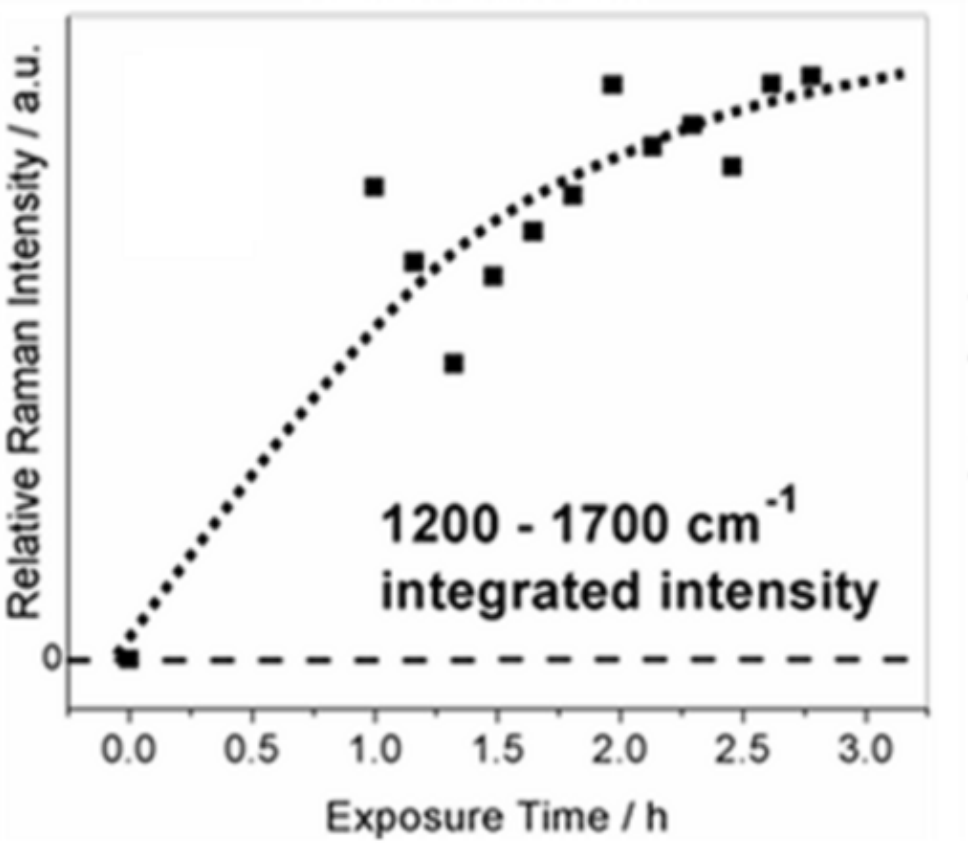

Figure 5.8. Plot of change in carbon Raman signal intensity collected over time from Ni mesh exposed to C_3H_8-containing gas flow at 625ºC.

A Ni mesh sample modified by BaO was subjected to the same experimental conditions. A micrograph of the surface of the modified Ni sample during wet C_3H_8 exposure at 625°C is shown in Figure 5.9. The micrograph was captured at the 15-hour mark near the Ni/YSZ interface. The spots that can be observed on the Ni surface were caused by modification treatment, since they were present on the modified Ni prior to any exposure to C_3H_8 and did not change afterward. The Raman spectra displayed in Figure 5.9 were collected from the marked spots on the modified sample. Carbon signal was not detectable even on the Ni surface in this case. In contrast, spectra collected from both unmodified and modified Ni that were simultaneously exposed to dry C_3H_8 at high

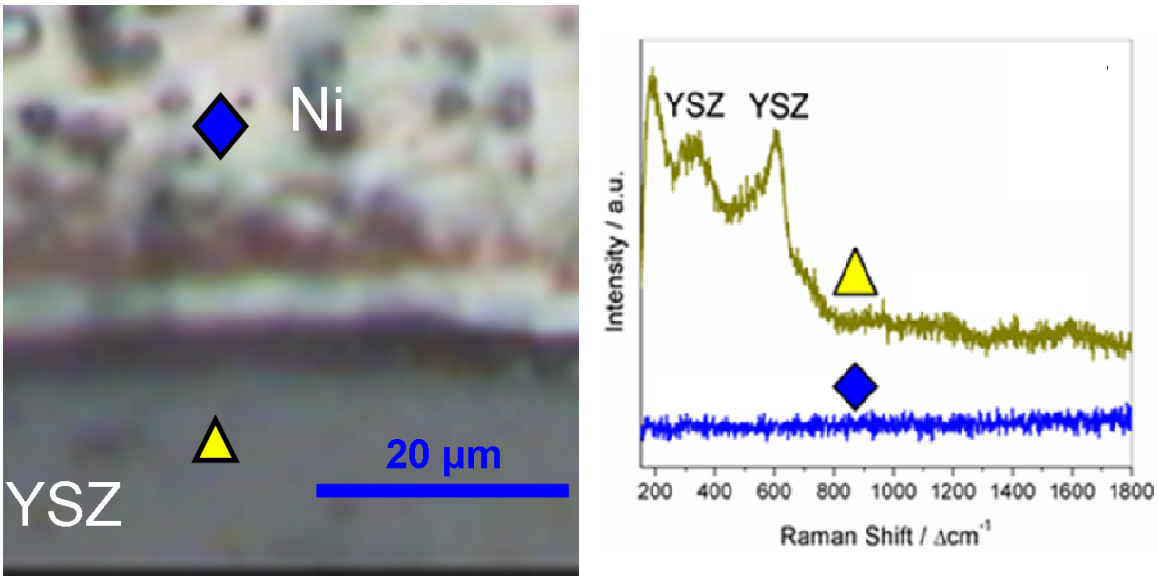

Figure 5.9. Optical micrograph near interface of BaO-modified Ni mesh and YSZ during C_3H_8 treatment (left) and Raman spectra collected *in situ* at the 15-hour mark from marked spots (right).

temperature (Figure 5.10) demonstrated similar amounts of coking, indicating that the BaO surface modification conveyed significant coking resistance to the Ni only in the presence of water. This information supports the hypothesis that the surface particles help utilize water to stave off carbon deposition.

The notion of that the modification particles used in these experiments were in BaO phase might be a surprise at first glance, as they were exposed to ambient air between treatment and testing. Conventional wisdom would indicate that these nanoparticles would convert to BaO_2 and/or $BaCO_3$ as these compounds are more stable than BaO in air. On the other hand, these experiments were performed at elevated temperatures under reducing conditions. BaO_2 is known to decompose to BaO above 500ºC when a negligible amount of O_2 is present.[106] Furthermore, both BaO_2 and $BaCO_3$

are Raman active materials[70, 107], and no peaks indicating either phase were observed in spectra collected from the Ni surface even at room temperature. Given the presence of water and the relatively high thermodynamic favorability for forming $Ba(OH)_2$ from BaO and water, the only likely phases present on the Ni surface were BaO and $Ba(OH)_2$.

5.7. Raman mapping of sulfur species on YSZ-embedded Ni mesh

Shown in Figure 5.11 is the typical poisoning and recovery behavior of the Ni mesh anode at 767°C under 20 ppm H_2S. Both the poisoning and recovery processes seem to finish and reach steady state within a few minutes, which is very different behavior from thick Ni-YSZ anodes that are traditional for such studies, where a much longer timeframe was needed especially for the recovery process.[18, 25] Recent studies have suggested that sulfur poisoning is a surface or interfacial phenomenon rather than one that affects the bulk of the material.[20] Specifically, the quick poisoning of the Ni mesh electrode might

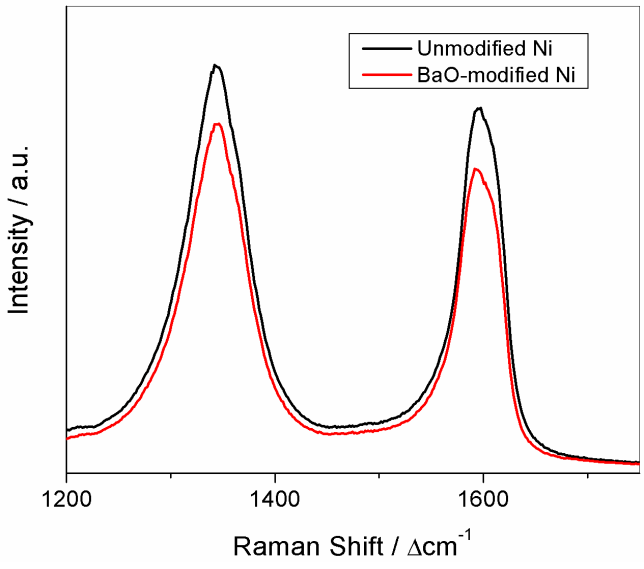

Figure 5.10. Raman spectra collected from Ni samples at room temperature following exposure to dry C_3H_8 at 625°C.

result from the direct exposure of Ni electrode to the fuel gas and subsequent sulfur adsorption; gas diffusion would not limit the rate of this process as much as in the case of a thick porous Ni/YSZ anode. Thus, the type of behavior observed here makes sense given that the all of the Ni surface and Ni-YSZ interfaces are directly exposed to the primary gas flow for the mesh anode in contrast with a conventional anode where the gas undergoes a tortuous path to reach the reaction sites.

Strongly adsorbed sulfur at or near the triple phase boundary (TPB) between Ni, YSZ, and fuel would likely block the active sites for electrochemical oxidation of H_2 at the TPB, resulting in quick performance loss. On the other hand, during the recovery process, the current passing through the cell can help the electrochemical oxidation of the sulfur adsorbed on anode surface to SO_2, especially at or near the TPB. Once sulfur is oxidized to SO_2, it will quickly desorb from anode surface, leading to the re-exposure of the Ni/YSZ interface to the gas phase (regeneration of TPBs) and virtually full recovery of the performance.[18] However, the current might not be efficient enough to fully remove the adsorbed sulfur far away from the TPB regions, which may remain on the surface even after full recovery of the performance. Therefore, Raman intensity mapping was used to gain more chemical information about how the electrode surface interacts with sulfur in fuel gas and explore this hypothesis.

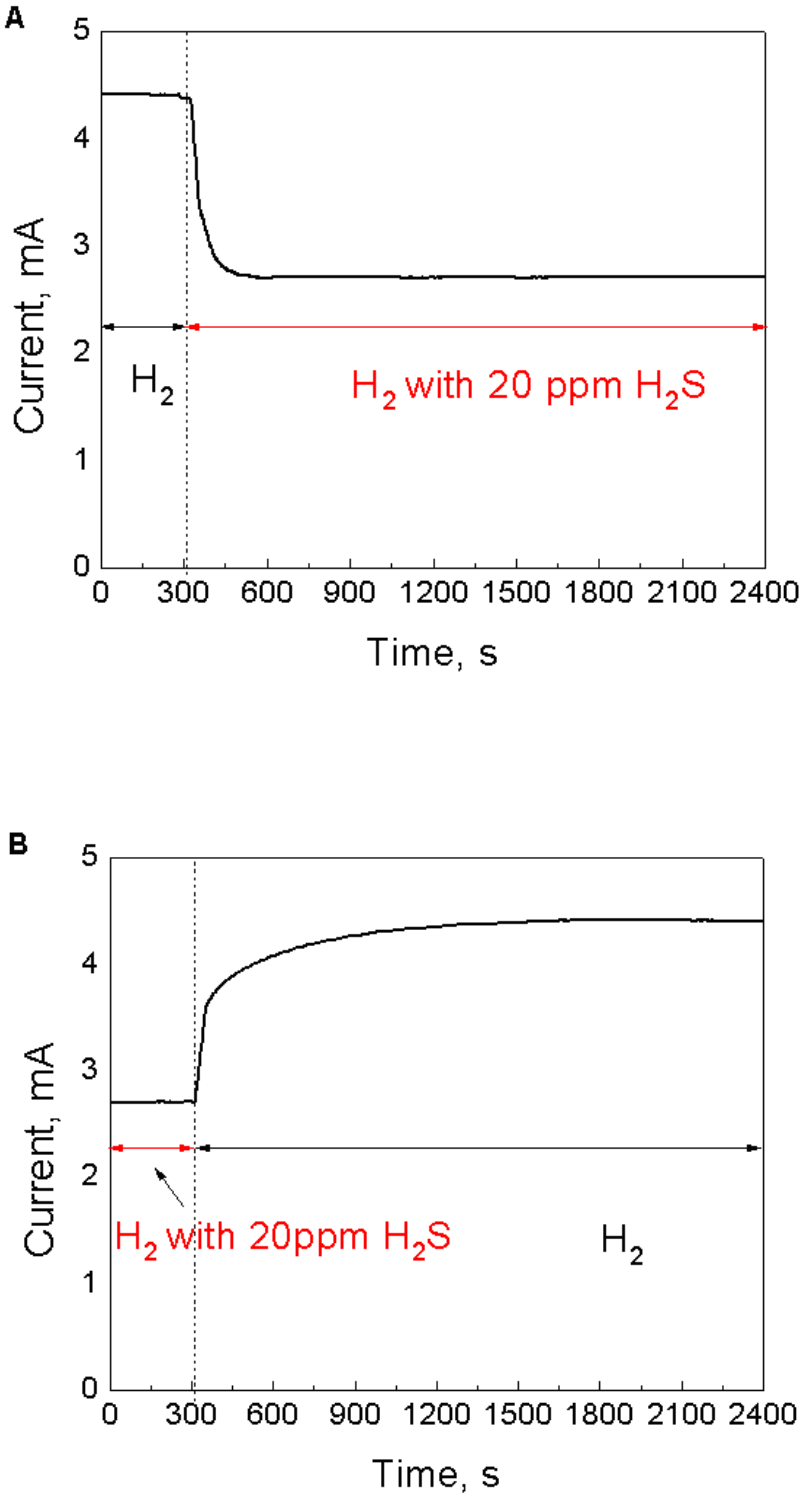

Figure 5.11. Typical (A) poisoning and (B) recovery behavior of the cell in H_2 with 20 ppm H_2S at 767°C operated at 0.75 V.

In order to work around the dearth of sensitivity that Raman spectroscopy possesses for elemental sulfur species, the electrodes were aged in air to form SO_x groups that can be more easily detected. Figure 5.12 displays the evolution of the Raman spectrum obtained from a spot on the surface of the Ni away from the TPB over the aging period. The peak at 980 cm^{-1}, which corresponds to SO_x groups[108] (most likely a SO_4^{2-} ion[70]), could only be seen after about 10 days.

Figure 5.13 displays an optical micrograph of the Ni/YSZ interface along with a Raman map of the same area plotting the intensity of the band associated with SO_x species (integrated intensity between 960-1000 cm^{-1}). The species were exclusively observed on the Ni surface and were generally concentrated more away from the TPBs. In addition, no other Ni-S phases could be detected by Raman spectroscopy, which supports the notion that the poisoning process at the studied temperature does not involve new bulk sulfide phase formation.

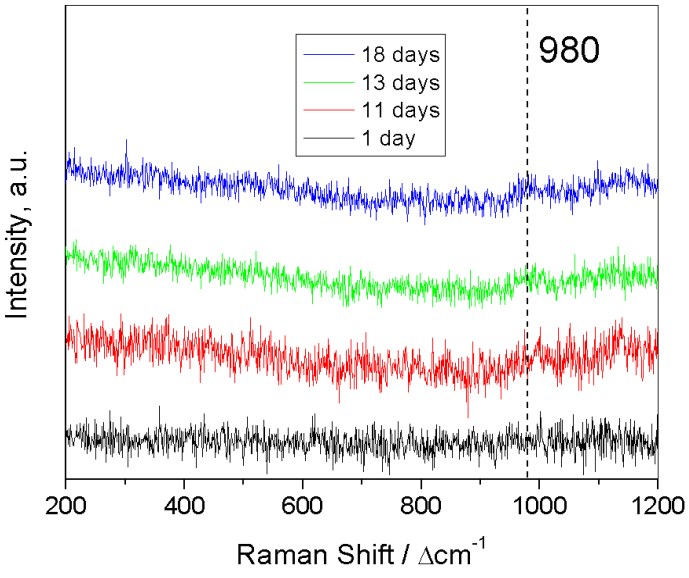

Figure 5.12. Raman spectra collected from Ni mesh cell surface post-operation in H_2S-containing fuel after various times of "aging" in air.

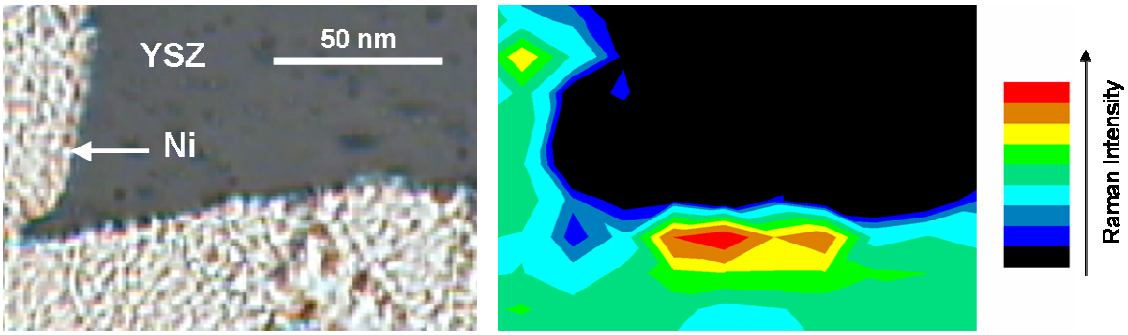

Figure 5.13. Optical micrograph of corner of patterned Ni mesh electrode in YSZ that was operated in H_2S-containing fuel and aged in air for 18 days (left) along with a Raman map of the SO_x band in the same area (right).

5.8. Summary of findings and future considerations

Raman spectroscopy has demonstrated great applicability in mapping and monitoring carbon on Ni-based SOFC anodes under *ex situ* as well as *in situ* conditions. Direct evidence of preferential coking on the Ni surface with little to no coking YSZ was provided, and the growth of carbon on the Ni surface was successfully monitored over time at high temperature. In addition, this technique provided additional evidence of the roles that water and BaO modification play in coking resistance on the Ni anode, which is useful information for further improving anode design.

The electrodes with well-defined boundaries used in this work facilitated the mapping and monitoring experiments. These types of electrodes, particularly the mesh design, can be readily applied to Raman experiments involving the application of both chemical and electrochemical stimuli. Current efforts are focused on coupling electrochemical measurements with the Raman techniques described herein to gain additional insight into the mechanisms of coking and its prevention on the SOFC anode.

For plain Ni anodes, the Raman mapping of sulfates shown above helps support the hypothesis that sulfur adsorption is the cause of sulfur poisoning rather than sulfide formation. For more complex systems, however, sulfur poisoning was shown to present a trickier in problem in general. While materials like BZCYYb can effectively stave off this type of degradation, BaO modification has been found to not afford the same protection to the electrode from sulfur as it does from coking. In fact, initial studies indicate that some types of Ba-containing oxide modification may exacerbate sulfur poisoning. Hence, detailed results on Raman analysis of sulfur poisoning for modified Ni mesh electrodes were not presented in this chapter, although Figure B.2 in Appendix B shows some more information. In addition, Chapter 7 presents results on investigations of sulfur poisoning in more realistic anodes modified by Ba-containing oxides that represent a similar situation. As for using *in situ* Raman spectroscopy to characterize sulfur poisoning and resistance, lack of signal obviously presents an obstacle that would only be heightened by high analysis temperatures. Thus, in order to be successful in such characterization, a suitable methodology for increasing Raman signal is necessary. The following chapter addresses this issue.

CHAPTER 6: SURFACE ENHANCED RAMAN SPECTROSCOPY FOR SOFCS

6.1. Surface Enhanced Raman Scattering (SERS)

The principal difficulty with using Raman spectroscopy for surface analysis is that in many cases, insufficient molecules of interest are available to impart enough Raman cross section to satisfy the sensitivity limits of Raman signal detection. While surfaces may have no shortage of molecules in general, some of these species may be of no interest to the investigator and would only serve to dilute the Raman spectra. Thus, rigorous cleaning of the surface of unwanted molecules might be required for successful analysis. In any event, using normal Raman analysis for high-temperature *in situ* catalysis studies (i.e. SOFC surface analysis) makes conditions even less ideal, as a high temperature environment does not compel species of interest that are weakly bonded to the surface to stay adsorbed for very long. Thus, enhancement of the Raman signal becomes compulsory for investigation of the electrode processes on electrode material surfaces.

In 1974, Fleischmann et al. discovered that a roughened silver electrode substrate enhanced the Raman signal of adsorbed pyridine molecules.[109] At the time, they attributed the augmentation to the increased surface area of the substrate. Later in the 1970s, two other research groups separately found that the signal increase was the result of other phenomena[110, 111], and the concept behind this enhancement came to be known as surface-enhanced Raman scattering (SERS). Recent reports on studied of SERS have claimed signal enhancement factors of up to 14 orders of magnitude for single molecules.[112]

The dominant mechanism that causes the Raman signal enhancement has been the subject of much scientific debate since its inception.[113] Two of the possible mechanisms contributing to the enhancement factor are chemical enhancement and electromagnetic enhancement. In the former, electrons are excited by incident photons into the lowest unoccupied molecular orbital of the molecules of interest from the conduction band of the rough metal substrate atoms, which results in a vibrational shift of the molecule, and the photon leaving the molecule and metal substrate will have the corresponding characteristic Raman shift. The other type of enhancement entails the electromagnetic resonances caused by the collective excitation of conductive electrons in the metal substrate due to the incident photons. These resonances are known as surface plasmons. This effect is thought to be greatest near very small contact points between metal nanoparticles that create signal enhancement "hot spots." The electromagnetic mechanism is generally thought to be more dominant than the chemical mechanism[54, 113, 114], particularly because the enhancement entails a fourth-power relation to the electric field functions involved as with normal Raman scattering. This relationship is shown in the following equation from work performed by Moskovits *et al.*[114]:

$$G_{loc} = | E_{loc}(\lambda) / E_0(\lambda) |^4 \qquad (6\text{-}1)$$

G_{loc} is the local signal enhancement factor, $E_{loc}(\lambda)$ is the local electric field determined by the surface structure as a function of the wavelength of the incident light, and $E_0(\lambda)$ is the electric field .

From its inception until today, SERS has been used for a wide variety of studies, and many methods for achieving the effect have been developed. Roughened silver and gold substrates have been shown as staple methods for obtaining SERS signals from

surface adsorbates [115, 116]. In addition, gold and silver colloids containing nanoparticles produce a SERS effect when scattered on or among materials to be measured [117, 118]. No one methodology exists that is applicable to measuring all materials systems. Fortunately, the various ways that SERS can be achieved allows for adapting a particular SERS route to an application for which it is suited.

6.2. SERS for detecting oxygen species on cathodes using sputtered Ag

SSC and LSC, which are SOFC cathode materials, were previously studied by Abernathy and colleagues using SERS techniques[105]. SERS was achieved using silver and gold colloids deposited on SSC as well as by synthesizing LSC-silver composites by combustion chemical vapor deposition (CCVD). Both sets of experiments showed promising results, but these methods displayed some inherent limitations. The preliminary spectra displayed many peaks that were not readily identifiable, which helps demonstrate that SERS may indicate surface species that are not expected to be present. Further complex theoretical calculations would be needed to resolve what these peaks represent. In addition, the results were difficult to reproduce, as it is a non-trivial task to control where the plasmon fields and hot spots appear on the surface. Development of an alternate signal enhancement methodology is likely necessary to mitigate these issues.

A potentially cleaner, more reproducible route for achieving a proper metal nanoparticle substrate for signal enhancement lies in the employment of DC magnetron sputtering. While this technique is normally used to deposit continuous metal thin films on surfaces, when a sufficiently short sputtering time and low power are used, highly discontinuous “island” structures can be produced. A schematic of this methodology is

shown in Figure 6.1a along with a micrograph of a typical surface sputtered with Ag in this manner (Figure 6.1b). Systematic studies on the influence of sputtering power and time on the structure of the Ag nanoparticles and the enhancement factor is the subject of work led by Xiaxi Li and Yingcui Fang, both who are colleagues of the author.[100, 119] The scope of this chapter is limited to the application of sputtered Ag to enhancing the signal from oxygen species.

Figure 6.2 shows the results of Raman analysis performed on LSM and LSCF samples on which highly discontinuous Ag thin films were deposited by DC sputtering. The short-term sputtering could presumably deposited island-like features less than 100 nm in size similar to those shown in Figure 6.1 in order to create the SERS enhancement. The spectra show indication of signal enhancement, although the enhancement is not as strong as that seen in previous work with colloids. That being said, a larger percentage (~10%) of the sample points collected from the sputtered samples showed signs of SERS than those collected from colloidal samples (~1%). The enhanced adsorbed molecular oxygen peak was usually present with the sputtered samples, as well. As can be seen above, the same features in general can be found in spectra from LSCF and LSM samples, but with slight shifts and varying degrees of enhancement.

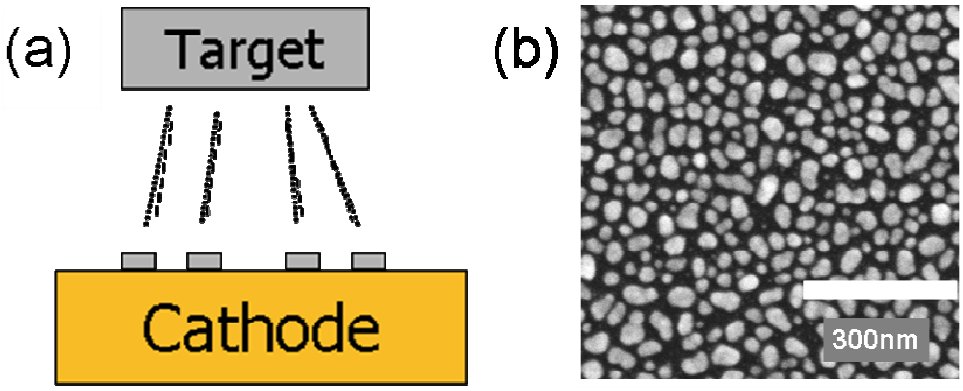

Figure 6.1. (a) Schematic of sputtering silver on a cathode material surface for inducing SERS effect. (b) SEM image of a typical surface after sputtering treatment.

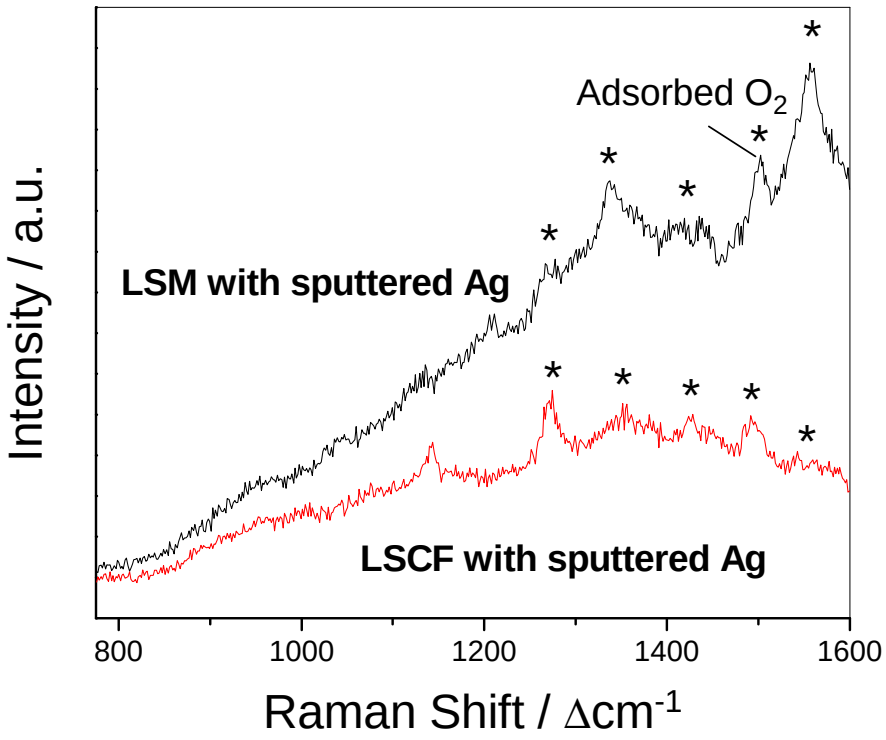

Figure 6.2. Raman spectra collected from LSM and LSCF pellets in air after DC sputtering of Ag.

For another set of experiments, three types of samples were analyzed. An untreated sintered pellet of LSM was used as a baseline sample. A pellet of LSM with Ag "nanoislands" deposited on the surface by sputtering at a power of 4 W for 30 s and a Si wafer piece sputtered with Ag at 10 W for 180 s were analyzed to evaluate the SERS effect. A lighter treatment was used in the case of LSM due to its inherently rougher surface texture.

Figure 6.3 displays a comparison between Raman spectra collected from the surface of each of the samples while they were held in a flowing O_2 atmosphere at room temperature in the Raman environmental chamber. Both of the spectra collected from each of the LSM samples contain the broad band between 250 and 800 cm^{-1} associated

with LSM, but the one from the sputtered sample contains additional peaks between 800 and 1700 cm^{-1} that emerged as a result of the Ag treatment. The treated Si sample spectrum contains similar peaks along with the characteristic peak for Si at 520 cm^{-1}.

A number of the new peaks were associated with the presence of oxygen. Spectra (a) and (b) in Figure 6.4 were collected from the Ag-treated Si sample under flowing Ar and O_2, respectively. Some of the peaks were only observed under oxygen. In particular, the 855-cm^{-1} and 1115-cm^{-1} peaks were respectively assigned to peroxo- and superoxo-like species[71] while the peak at 1598 cm^{-1} was assigned to neutral adsorbed oxygen.[72] In addition, these peaks decreased in intensity under continued exposure to the laser as can be seen from spectrum (c) in Figure 6.4. The heat from the laser may have had a "photobleaching" effect that changed the surface oxygen adsorption properties or the SERS substrate itself in a way that decreased the oxygen signal. Finally, heating the chamber to 400°C, which is closer to typical SOFC operating temperatures, resulted in the disappearance of most of the peaks from the Raman spectrum. One possible reason for this is that metal nanoparticles tend to start flowing at lower temperatures than particles of larger size, which may negate the rough nano-sized features needed to induce the hot spots that cause signal enhancement.

These results reveal that some issues with performing *in situ* Raman spectroscopy with the aid of silver nanoparticles under fuel cell operating conditions must be addressed to make this type of analysis effective. Evidently, heating treated samples deactivates the enhancement effect. In fact, few researchers have been able to study similar elevated-temperature systems successfully to date.[120] Itoh et al. were able to achieve in-situ SERS for studying oxygen reduction for molten carbonate fuel cells, and they observed oxide

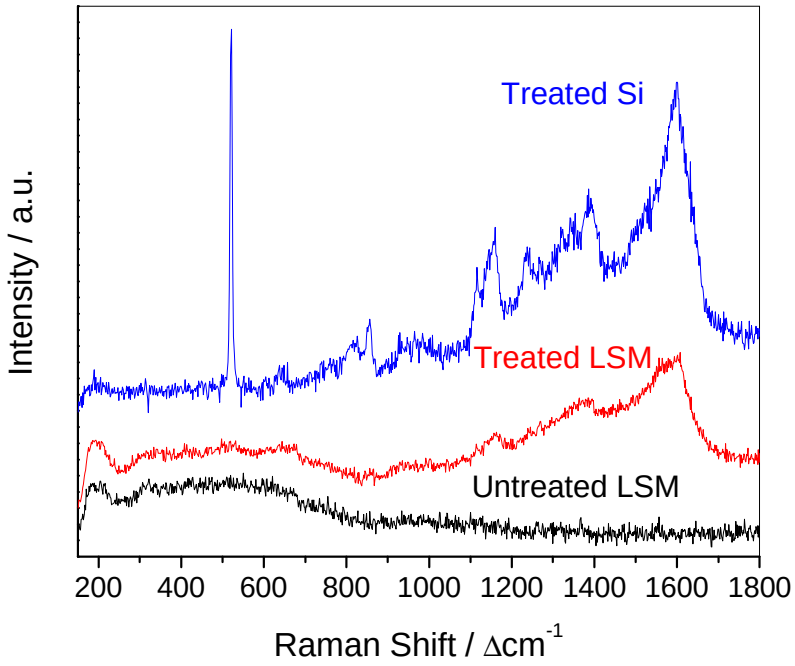

Figure 6.3. Raman spectra collected at room temperature under pure flowing O_2 from LSM and Si samples treated by Ag sputtering.

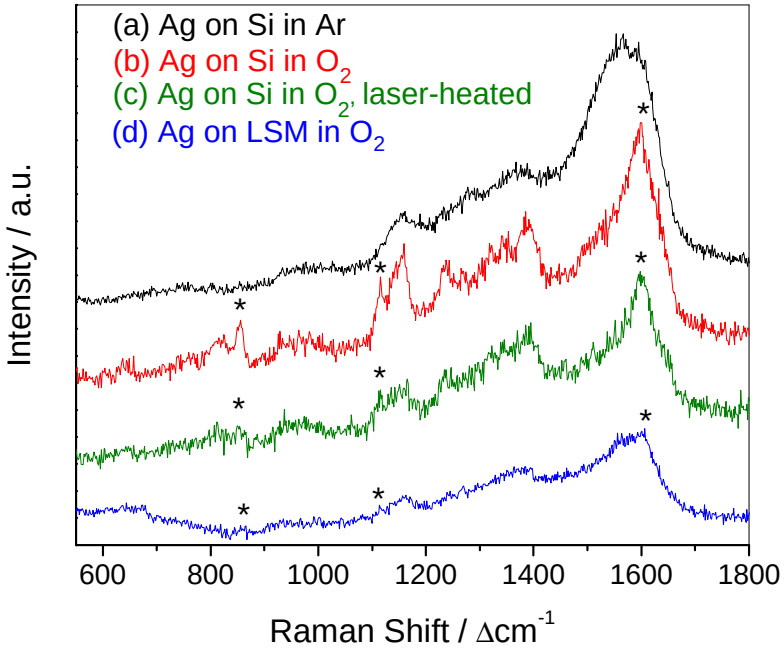

Figure 6.4. Raman spectra collected at room temperature under pure flowing O_2 or Ar from LSM and Si samples treated by Ag sputtering with varied conditions.

and superoxide species on silver electrodes[121] with results only somewhat improved from those in previous work.[122]

The question also remains whether the Ag nanoparticles themselves comprised the source of the oxygen signal in the experiments shown above. Ag is known to be catalytically active and adsorb O_2 quite well, and as both Figures 6.3 and 6.4 show, the intensity of these peaks is greater on the Si sample than the LSM sample, where the Ag sputtering treatment was lighter. When analyzing cathode surfaces by *in situ* Raman spectroscopy, if bare Ag surfaces are present as part of a SERS treatment, the spectra might be skewed in terms of indicating which oxygen species are in abundance on the electrode surface. Therefore, Ag nanoparticles alone may not serve as a suitable SERS treatment for this type of study. Au nanoparticles provide a possible alternative since they are more thermally robust and less catalytically active, but they require that the incident light have a longer wavelength, which would lower the overall Raman scattering signal.

6.3. Core-shell nanoparticle SERS ("SHINERS") of SOFC anodes

An ideal method for performing SERS-assisted *in situ* Raman spectroscopy in SOFC systems would consist of the signal-boosting advantages of Ag nanoparticles with none of their drawbacks. Thankfully, this scenario is potentially feasible using core-shell nanoparticles. Tian *et al*. recently developed a methodology in which they coated Au nanoparticles about 55 nm in size with a ~2 nm SiO_2 shell (i.e. Au@SiO_2 nanoparticles). The shell prevented the nanoparticles from agglomerating but was thin enough such that the plasmonic effects of the nano-sized Au would still work on analytes in close proximity to the nanoparticles and produce the SERS effect. The researchers coined the

name “shell-isolated nanoparticle-enhanced Raman spectroscopy,” or “SHINERS,” for this technique.[123] Using these core-shell nanoparticles, they were able to boost the signal for a variety of systems, including hydrogen species adsorbed on Pt and pesticide residues on citrus fruits. Others have such as Thomas *et al*. have successfully employed SHINERS for their own efforts and studied the methodology itself more systematically.[124]

Some initial experiments have been performed in the application of $Ag@SiO_2$ core-shell nanoparticles to *in situ* studies of SOFC electrodes. The SiO_2 shell theoretically provides thermal robustness to the Ag nanoparticles to prevent them from aggregating at high temperatures. In addition, as SiO_2 has less catalytic activity than Ag, it has less chance of skewing the data on which species are present during fuel cell reactions.

First, $Ag@SiO_2$ nanoparticles were prepared and characterized by transmission electron microscopy (TEM). Figure 6.5 shows a set of images depicting typical nanoparticles; as the images show, the nanoparticles have a ~40-80 nm size range. In the higher-magnification inset, a ~1-3 nm shell is visible on the nanoparticle.

While experimental work involving the use of these nanoparticles is still in its preliminary stage and has only been applied to the anode side of the cell thus far, the results acquired so far are quite promising. For instance, using the $Ag@SiO_2$ nanoparticles, hydrocarbon gas species were successfully detected on a Ni surface at an elevated temperature. Figure 6.6 displays Raman spectra obtained at 400ºC from a Ni coupon treated with $Ag@SiO_2$ nanoparticles under 4% H_2 / 96% Ar gas flows with and without C_3H_8. The large features seen in both spectra are from residual carbon on the Ni

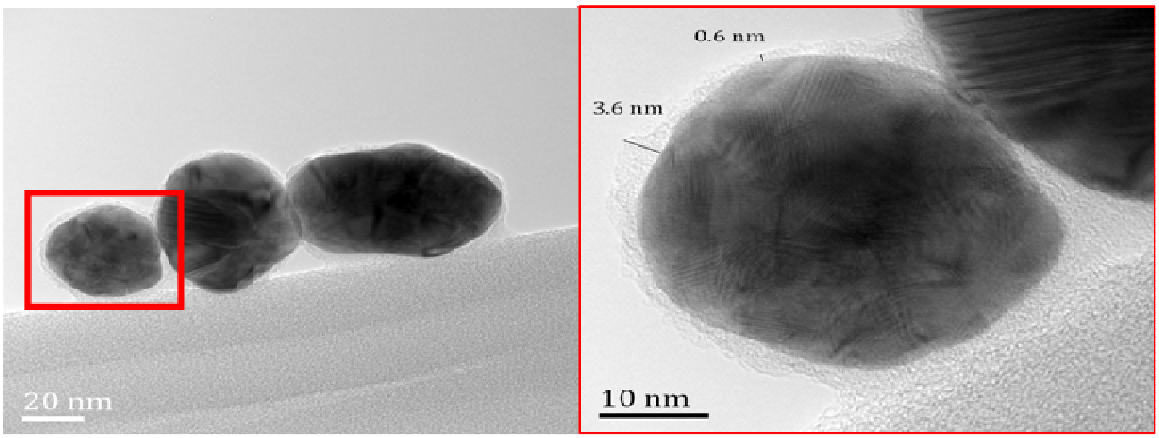

Figure 6.5. TEM images of $Ag@SiO_2$ nanoparticles (courtesy of Dr. Wentao Qin).

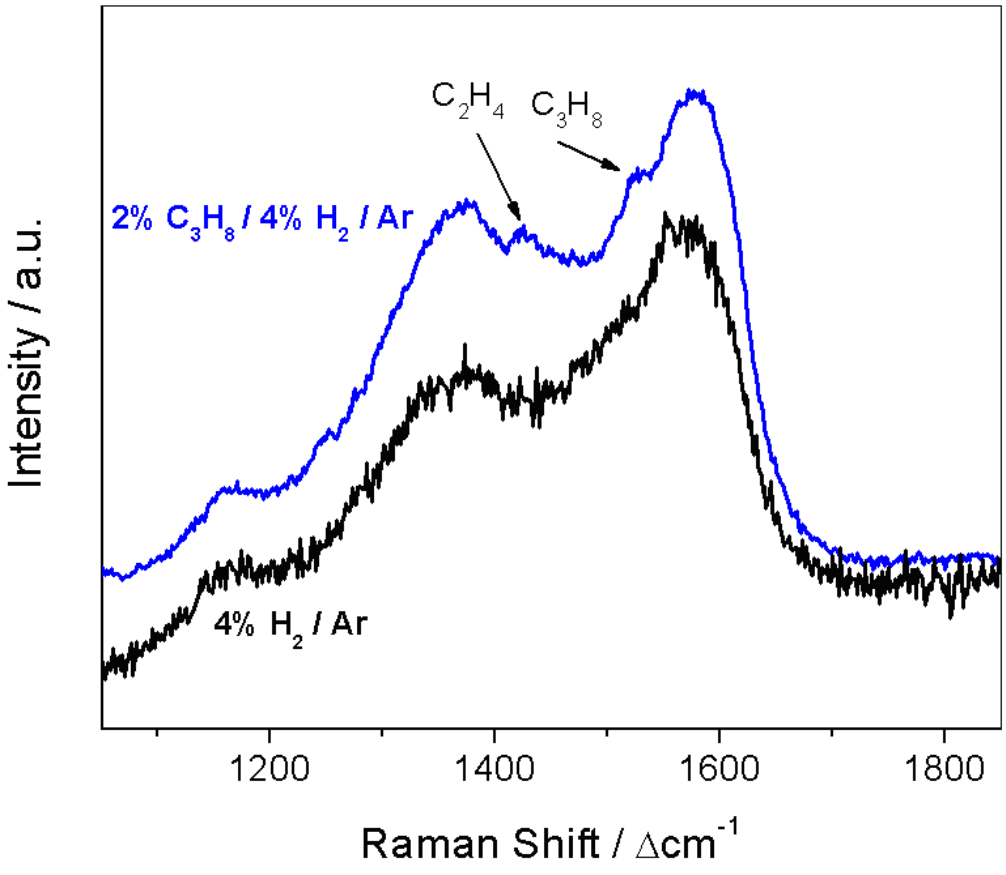

Figure 6.6. Raman spectra obtained at 400ºC in different flowing gas atmospheres from a Ni coupon surface treated with $Ag@SiO_2$ nanoparticles.

coupon; the signal is large due to the SERS treatment. When 2% C_3H_8 was introduced into the gas flow, two extra peaks at 1425 cm^{-1} and 1528 cm^{-1} became visible in the Raman spectrum after a few minutes. These peaks were assigned to C_2H_4 and C_3H_8 species, respectively.[125, 126] These results suggest that at fuel cell operating temperatures, a Ni-containing anode may catalyze the cracking of propane and higher-order hydrocarbons into lower-order hydrocarbons. A more systematic study might reveal the role this cracking plays in coking. Finally, to put the results further in context, without this SERS treatment, regardless of gas atmosphere, Raman spectra collected in the same cm^{-1} range from the Ni surface at 400ºC appeared as a flat noise line (not unlike the bottom trace of Figure 6.1 in Chapter 6).

6.4. Summary of findings and future considerations

From the results of the experiments outlined above, SERS methodologies have shown significant promise in assisting in Raman-based characterization of the surface chemistry in SOFCs by enhancing Raman signal. Preliminary *in situ* experiments with controlled atmospheres demonstrated the potential to yield pertinent information on key surface species for SOFC processes. Reduced oxygen and hydrocarbon species at the cathode and anode were successfully detected at high temperature, which was not possible before these treatments.

While "conventional" SERS substrates consisting of bare Ag nanoparticles may not be appropriate for more systematic investigations due to lack of thermal robustness and potentially misleading catalytic activity, $Ag@SiO_2$ core-shell nanoparticles present a route for working around those issues. Possible future work along this direction includes

analyzing electrodes with $Ag@SiO_2$ nanoparticles under various applied electrochemical conditions and environments closer to actual SOFC operating temperatures. The data collected in this investigation might also be supplemented by simulations, such as quantum chemical calculations, in order to predict the species and intermediates that might be observed.

CHAPTER 7: BI-ELECTRODE SUPPORTED SOLID OXIDE FUEL CELLS

7.1. The NASA bi-electrode supported cell (BSC) architecture

One important characteristic of SOFCs that requires improvement in order to make the technology more attractive for wide commercial application is specific power density. High specific power densities open up the possibility for SOFCs to be implemented in aeronautical applications including auxiliary power units (APUs) that provide electrical power to secondary systems on commercial aircraft as well as powering unmanned aerial vehicles (UAVs). In the case of APUs, the systems would ideally be supplied by jet fuel and efficiently convert the fuel to electricity for use on board the aircraft. In the case of UAVs, NASA has studied the potential use of regenerative SOFCs (RSOFCs), which are cells that can perform electrolysis as well as fuel-energy conversion.[127] Such UAVs would contain solar panels that power aircraft's systems as well as the electrolytic conversion of the SOFC water byproduct to H_2 fuel by day. At night, the RSOFC system would operate in "fuel cell" mode and power the aircraft in the absence of the sun. While this "fuel cycle" seems ideal due to solar energy being virtually limitless and providing constant replenishment of fuel, this kind of system would still benefit from the additional ability to convert logistics fuels for shorter range UAV missions and in a situation where the solar power systems were to fail during operation on longer missions.

Engineers at the NASA Glenn Research Center recently developed a novel SOFC architectural design that dramatically improves specific power density known as the bi-electrode supported cell (BSC).[78, 127] The basic architecture consists of two porous YSZ

scaffolds acting as electrode supports that are connected by a dense layer of YSZ as the solid electrolyte. The electrode scaffolds have thin layers of functional materials that are ideally porous, interconnected, and firmly adhered to the YSZ in order to make them electrochemically active. These layers are applied using solution infiltration techniques. The porosity of the scaffolds is functionally graded in order to maximize gas flow and diffusion as well as triple phase boundaries (TPBs) for electrochemical activity. The shrinking size and directionality of the pores towards the electrolyte also create capillary forces that pull infiltrated solution towards the electrolyte and assist in maximizing the coverage of the scaffold by the electrode layer.

This architecture allows for high specific power density (e.g. >1 kW/kg) by addressing multiple technical obstacles at once. Since current collection occurs throughout most of the cell, due to the infiltrated electrodes, the interconnect used for cell stacks need not be very thick. Therefore, a thin layer can be used to separate the cells, which makes using traditional interconnect materials like Ca-doped $LaCrO_3$ (LCC) more economically viable. A ceramic interconnect would convey several advantages: lower system weight, prevention of cathode chromium poisoning from cell interconnects made of steel alloys[52, 128, 129], and optimized operation temperatures around 800-850°C that would allow for high power output. In addition, an all-oxide "unitized" stack system improves sealing and eliminates losses from interfacial resistance between metals and oxides. Shown in Figure 7.1 is a cross-sectional micrograph of a typical stack that demonstrates its "unitized" attribute.

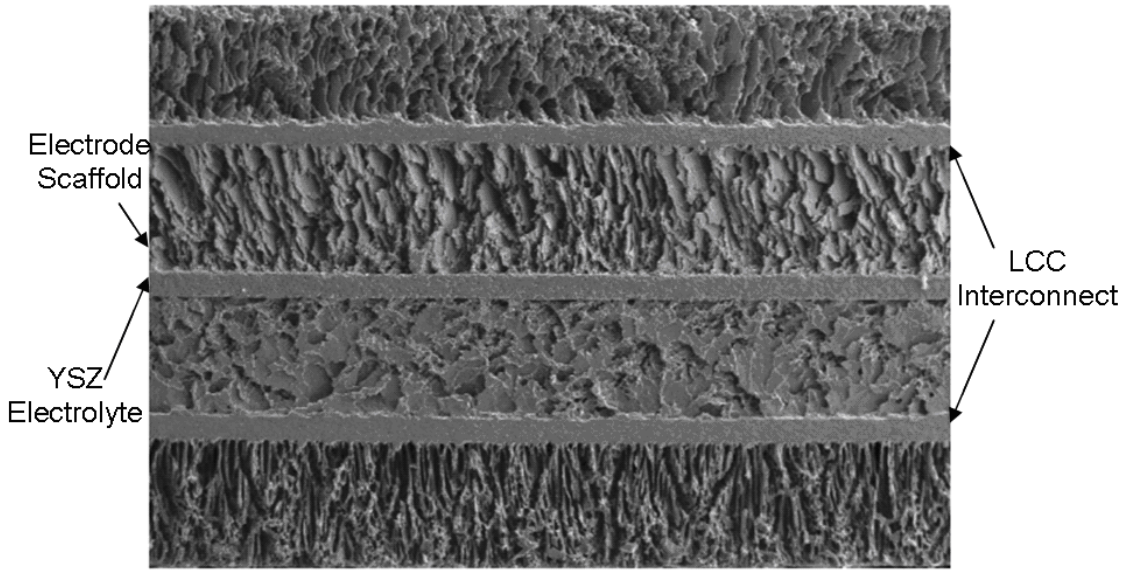

Figure 7.1. SEM micrograph showing a portion of a BSC stack. One cell unit is represented by the five layers in the middle. Reproduced from previous work by Cable et al.[78]

The current BSC specifications include state-of-the-art electrode materials such as LSCF cathodes and Ni anodes. Unfortunately, Ni anodes limit the types of fuels with which the cell may operate. Supplying the anode in the BSC with the hydrocarbons, especially the high-order aromatic ones contained in jet fuel, would likely result in very aggressive coking and quick anode degradation. In addition, such anodes are susceptible to deactivation by sulfur contaminants in the fuel stream. Jet fuels, even when desulfurized by the most modern techniques, still contain 10 ppm of sulfur species or more[130], and a more conventional fuel treatment will produce a fuel with sulfur content that has only been reduced to the 100 ppm range[131]. These levels of sulfur content in the fuel stream would be sufficient to cripple a Ni-anode cell's performance within a short time.[132]

In order to make BSC-type SOFCs fully fuel-flexible and an ideal power system for aeronautical applications, the issues of anode tolerance to coking and sulfur poisoning need to be addressed. One possible route for overcoming these problems is modification of the Ni anode layers with oxide nanoparticles. A schematic for such modification is presented in Figure 7.2 below. Results of previous research as well as the information gained from the Raman spectroscopic studies in the current work have demonstrated that oxides containing Ba and Yb with an affinity for water can play a role in staving off coking and sulfur poisoning respectively. Thus, several oxide compositions were surveyed and evaluated for their effect on performance and the resistance to fuel-induced degradation that they convey.

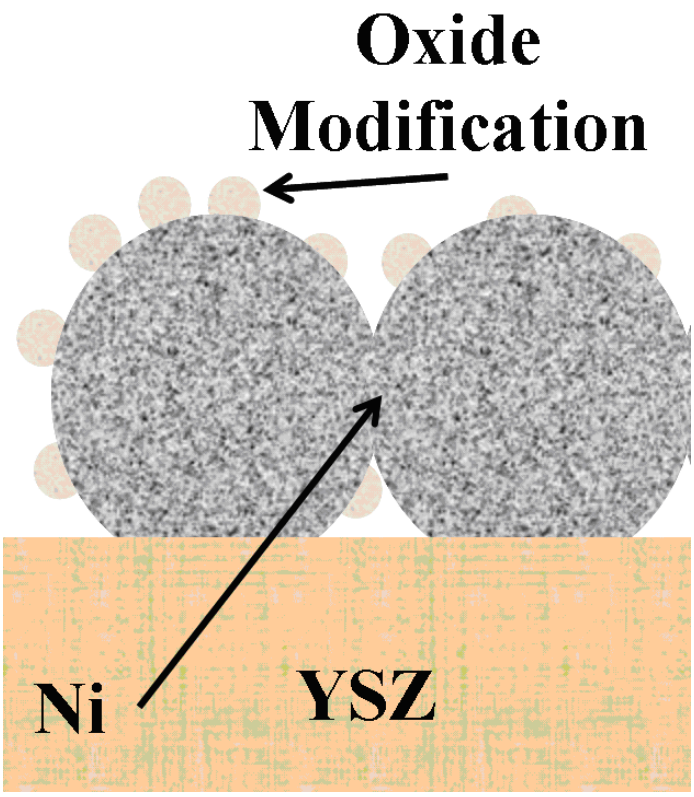

Figure 7.2. Basic schematic for oxide modification of anode layer in BSCs.

7.2. $BaO\text{-}Yb_2O_3$-modified BSC anodes

The 3Ba-4Yb modification composition was chosen because $Ba_3Yb_4O_9$ would theoretically be the eventual phase formed as indicated by phase diagrams derived from previous work.[133, 134] $Ba_3Yb_4O_9$ is a simpler two-component oxide which has R3 perovskite structure[135] in contrast to the more complex material BZCYYb that has five metal components. Ba and Yb oxides also tend to have an affinity for water, which seems to be the key to resistance to coking. Finally, given the success of BZCYYb in preventing sulfur poisoning over other $BaCeO_3$-based materials[5], the inclusion of Yb in the modifying oxide potentially plays a role that is yet to be elucidated.

Displayed below in Figure 7.3 (a) and (b) are typical current-voltage and power density curves at 750°C and 800°C for BSC-type cells operating in wet (3 vol. % H_2O) H_2 (40 sccm flow rate) with unmodified Ni and Ni infiltrated with $BaO\text{-}Yb_2O_3$ modification. This modification decreases the cell's performance in H_2 fuel by roughly 45%; the unmodified cell reached a peak power density (PPD) of 0.62 W/cm^2 at 800ºC while the modified cell's PPD was only 0.35 W/cm^2. On the other hand, Figure 7.4 shows a comparison of operation stability in wet dilute C_3H_8-containing fuel (~5 vol. % balanced by Ar) between unmodified and $BaO\text{-}Yb_2O_3$-modified cells over 24 hours. The unmodified cell displayed gradual degradation behavior followed by a sharp drop-off, losing 20-30% of performance within 24 hours. The $BaO\text{-}Yb_2O_3$-infiltrated cell, however, remained relatively stable over one day of operation. Raman spectra were also collected from the anode surface following operation; these spectra are presented in Figure 7.5. The modes centered at 1350 and 1585 cm^{-1} are respectively assigned to the D and G bands of carbon. As the spectra show, the carbon peaks on the modified anode are

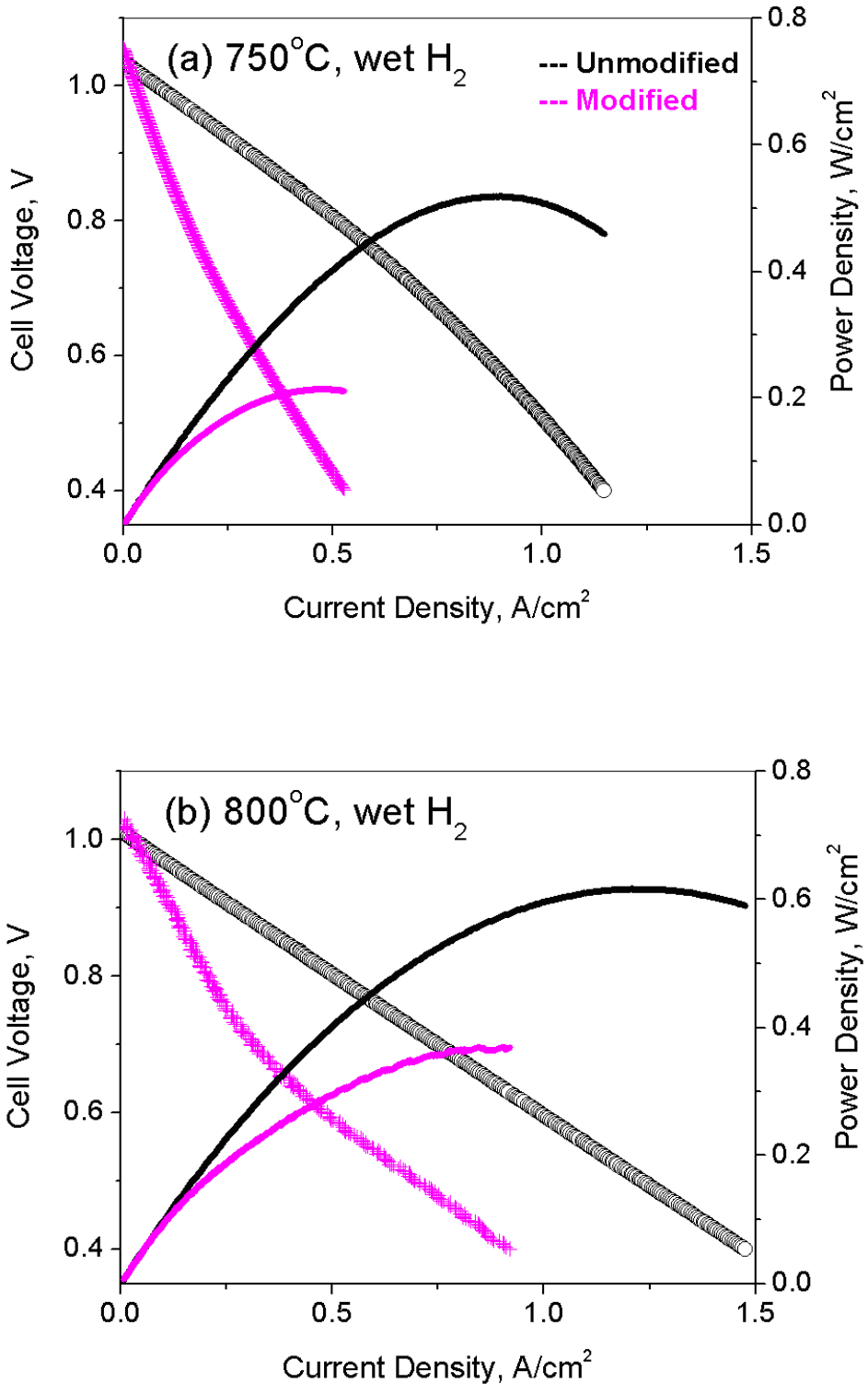

Figure 7.3. Current-voltage and power density curves for unmodified and 3Ba-4Yb-modified cells operating in wet H_2 at (a) 750ºC and (b) 800ºC.

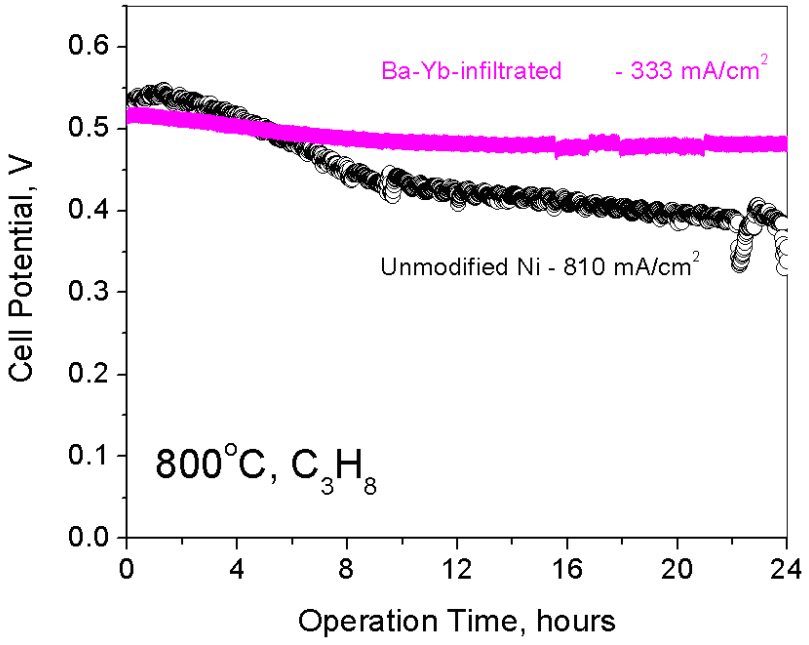

Figure 7.4. Stability over time of unmodified and 3Ba-4Yb-modified cells operating in wet C_3H_8-containing fuel at 800ºC.

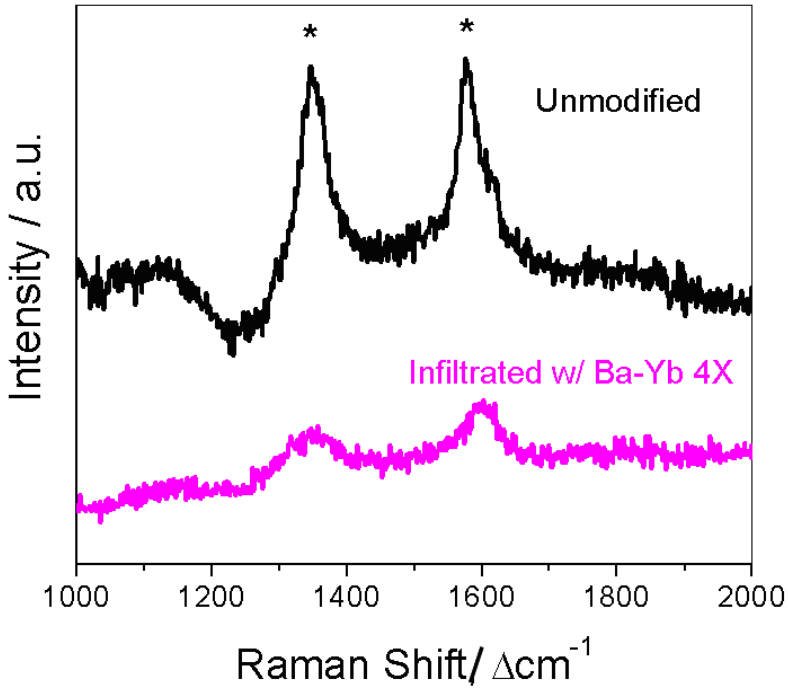

Figure 7.5. Raman spectra collected from unmodified and 3Ba-4Yb-modified cells following operation in wet C_3H_8-containing fuel at 800ºC.

considerably less intense (~70% reduction) than on the unmodified anode. Thus, the oxide on the anode surface of this cell likely provided some coking resistance despite having lower overall performance.

Despite the coking tolerance that the Ba-Yb oxides conveyed to the BSC anode, they appeared to be detrimental to overall performance. One possible reason is that too much oxide might have been applied to the anode, greatly increasing the system's resistance. A related and possibly larger issue potentially manifested in the form of incomplete phase formation. X-ray diffraction (XRD) analysis of powder calcined from the 3Ba-4Yb infiltration solution at 1000ºC shows evidence of such (Figure 7.6). While the XRD pattern shows evidence of high water content in the powder by virtue of the broad hump at low 2θ, peaks corresponding to $BaCO_3$[136] and Yb_2O_3[137] but not $Ba_3Yb_4O_9$ can be observed, indicating that the desired reaction and phase were not achieved under the conditions of the infiltration treatment process. This finding concurs with the low overall cell performance, as $BaCO_3$ and Yb_2O_3 are not highly conductive phases. From the results of these experiments, one can conclude that a less concentrated and more reliably stable oxide would be a more suitable modification for the BSC anode.

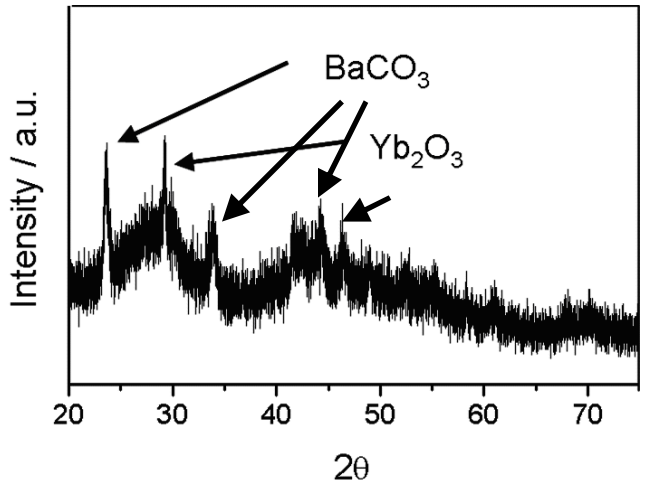

Figure 7.6. XRD pattern acquired from powder calcined from 3Ba-4Yb solution.

7.3. BZCYYb-modified BSC anodes

The main reason for choosing BZCYYb as one composition is its proven coking and sulfur poisoning resistances. In this case, however, a more dilute infiltration solution (~0.02 *M*) was used in order to prevent conductivity problems in the anodes caused by excessive oxide. A higher concentration (~0.4 *M*) was initially attempted with one set of cells, but their performance was unacceptably low (Figure B.2 in Appendix B).

Figure 7.7 presents a comparison between the overall cell performance of unmodified Ni and BZCYYb-modified Ni anodes in BSCs. Over the 600-800ºC operating temperature range, performance improvement ranging from ~40% to over 100% was observed for the BZCYYb-modified anodes over the unmodified cells. The peak power density achieved for the BZCYYb was ~0.9 W/cm^2 at 800ºC, although relative performance enhancement was higher at lower temperatures. In addition, the modified cells had more linear V-I curves, indicating less interfacial resistance.

A more noteworthy improvement given by the BZCYYb modification, however, is stability in hydrocarbon fuel. Shown in Figure 7.8 is a comparison between the stability of the unmodified and BZCYYb-modified cells operating in CH_4 fuel at 700°C; while the cell with the plain Ni anode displayed a sudden sharp drop-off in voltage associated with critical carbon buildup after 2 days of operation, the cell with the modified anode remained relatively stable over several hundred hours. In fact, under these conditions, the testing lifetime of the modified cells under these conditions was determined by the cathode's current collector that was comprised of Ag paste and wire, which would fail after ~500 hours. Figure 7.9 displays Raman spectra obtained from both anode types after

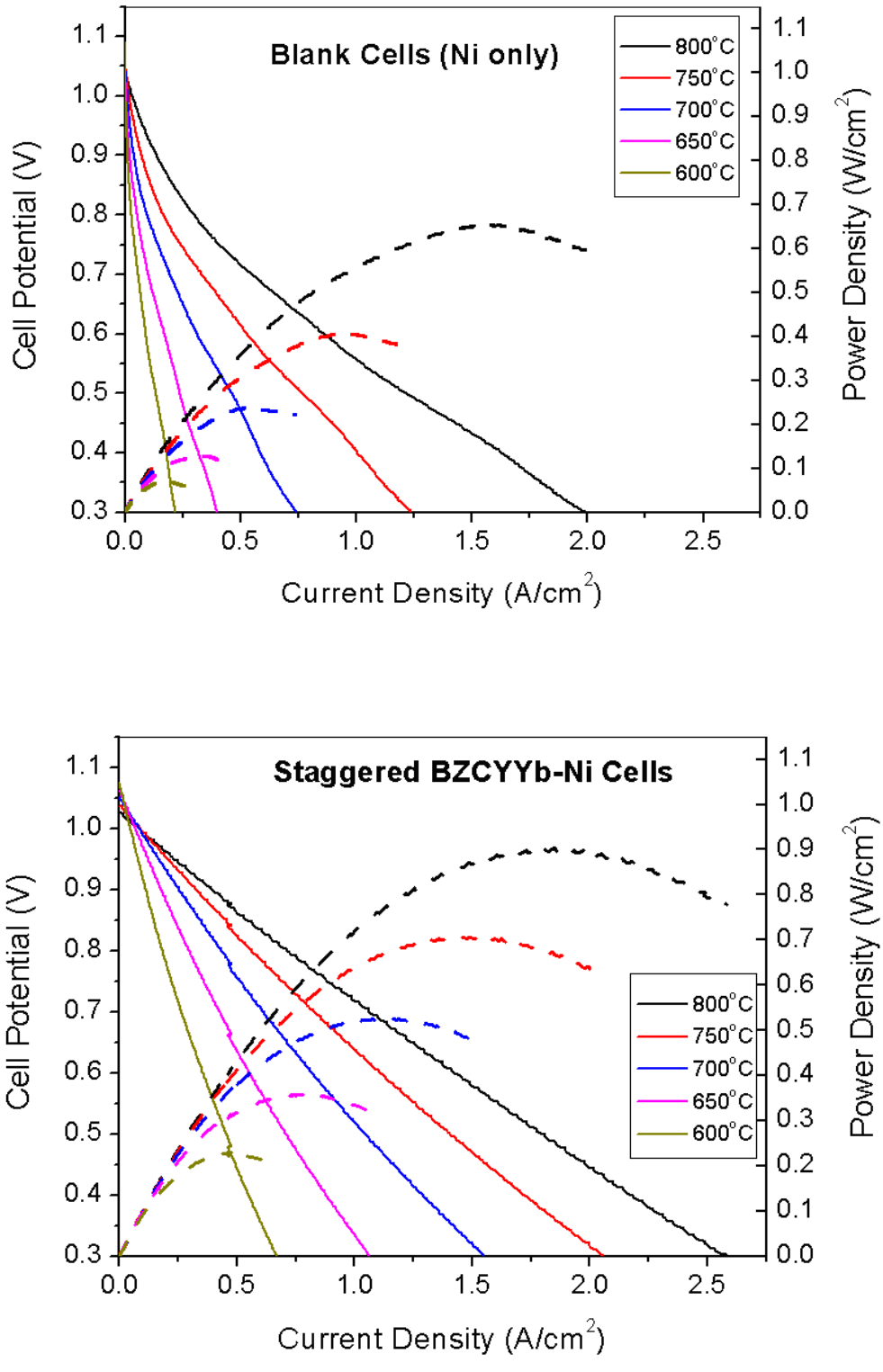

Figure 7.7. Current-voltage and power density curves for unmodified (top) and BZCYYb-modified cells (bottom) operating in wet H_2 at various temperatures.

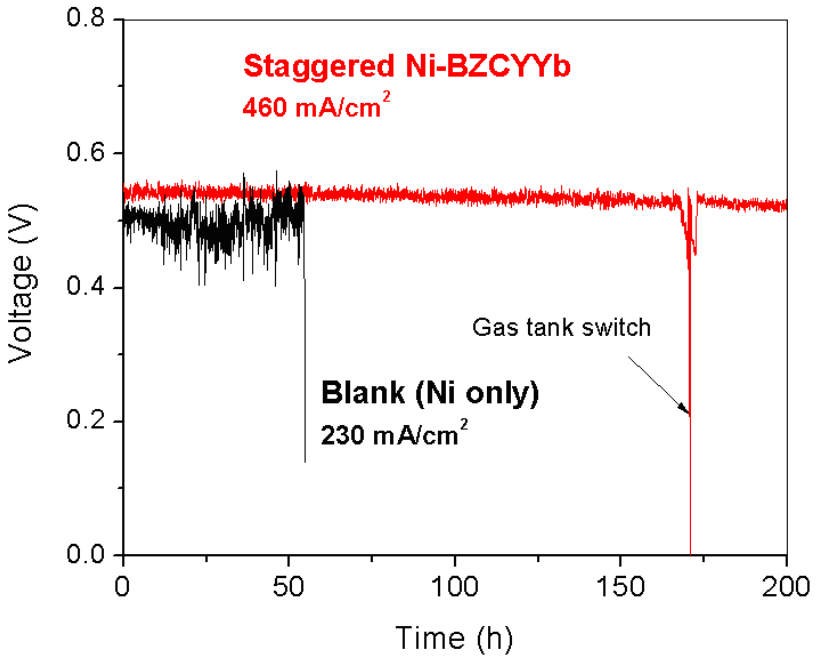

Figure 7.8. Stability over time of unmodified and BZCYYb-modified cells operating in wet CH_4 fuel at 700ºC.

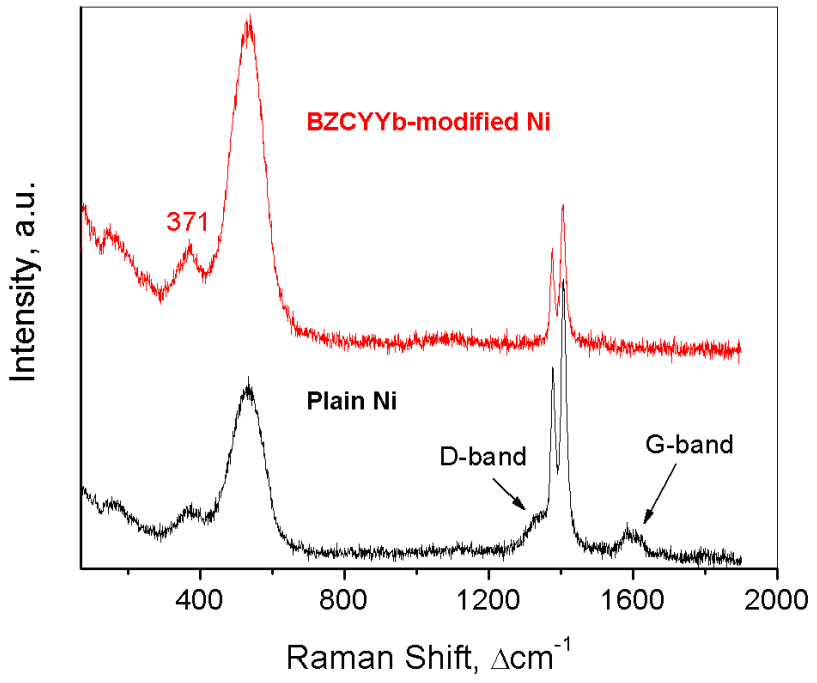

Figure 7.9. Raman spectra collected from unmodified and BZCYYb-modified cells following operation in wet CH_4 fuel at 700ºC.

operation in CH_4 fuel; the carbon D and G band are again quite apparent in the spectrum from the blank Ni anode but not in the modified anodes. The other sharp peaks in that range (1380 cm^{-1} and 1410 cm^{-1}) are assigned to Raman modes from the YSZ that occur under the 633 nm excitation that was used to collect these spectra. Finally, the feature at 371 cm^{-1} is much sharper in the modified anode spectrum, possibly corresponding to the BZCYYb coating itself on the anode.

The phase of the oxide formed by the modification was confirmed by calcining a sample of the BZCYYb solution at 1000ºC and analyzing the resulting powder using XRD. The powder's XRD pattern (Figure 7.10) showed peaks corresponding to the BZCYYb perovskite phase.[5]

In order to better understand the improvement in performance and stability of the modified cell over the blank cell, the anodes were characterized by scanning electron microscopy (SEM). Micrographs of the unmodified anodes before reduction and operation are displayed in Figure 7.11. The micrograph of the edge-on cross-section of the scaffold wall shows that the thickness of the anode layer is about 1-2 µm. Meanwhile, the top view of the anode layer's surface demonstrates its porous structure. In comparison, the surface of the modified anode (Figure 7.12) displays smaller grain size.

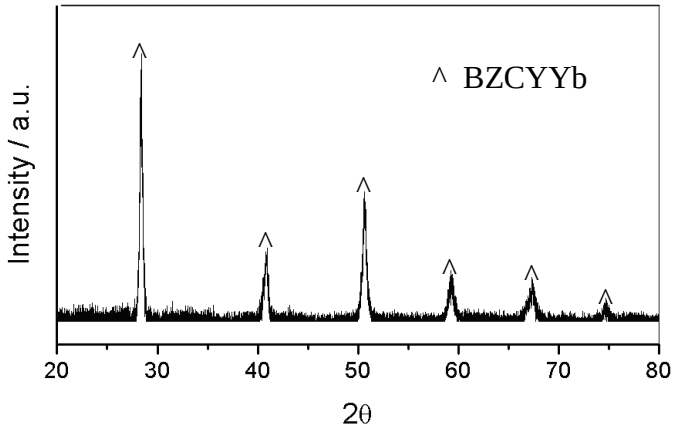

Figure 7.10. XRD pattern acquired from powder calcined from BZCYYb solution.

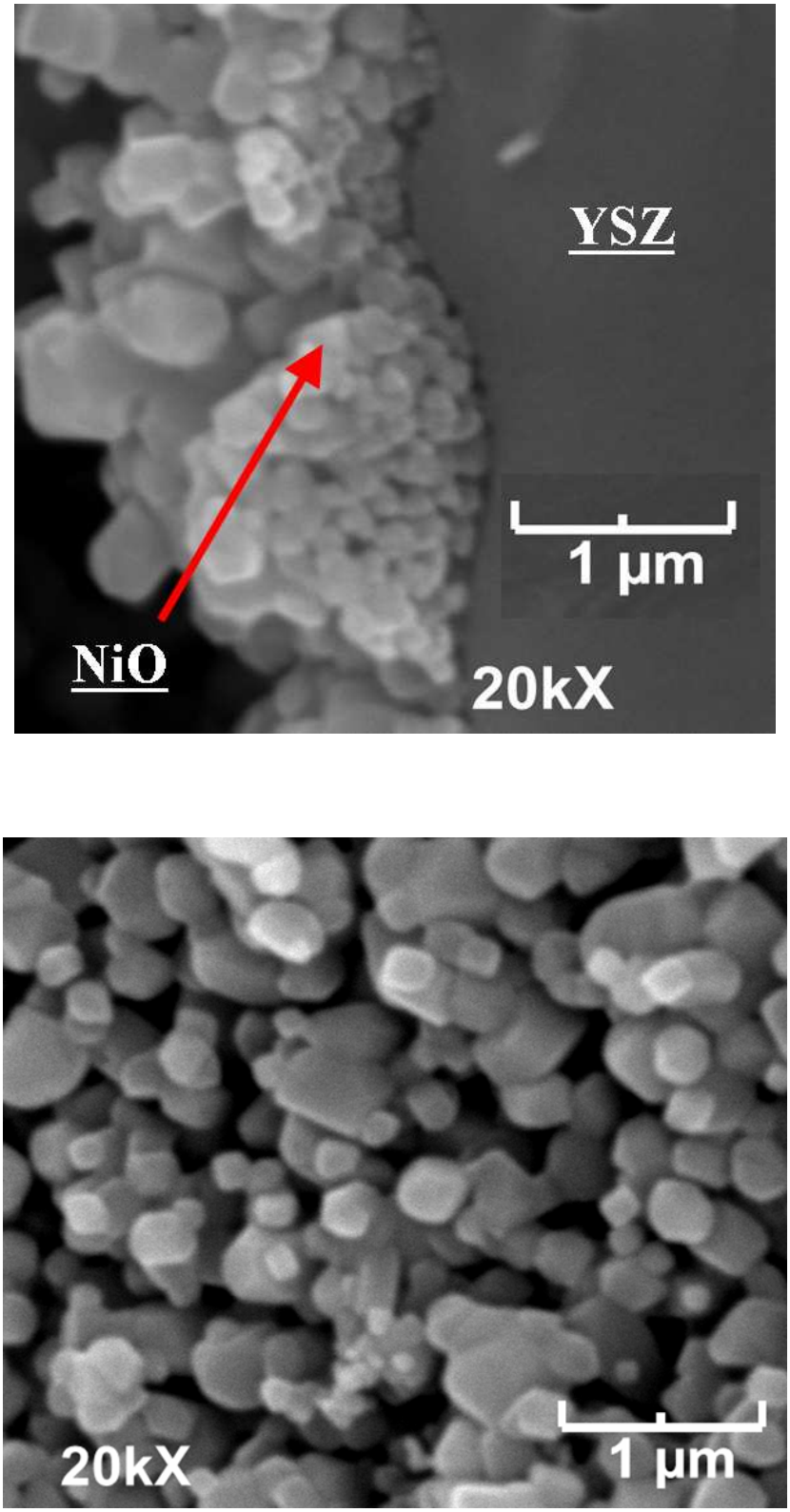

Figure 7.11. SEM images of the edge-on cross section (top) and the top surface (bottom) of the unmodified BSC anode scaffold wall prior to reduction or operation.

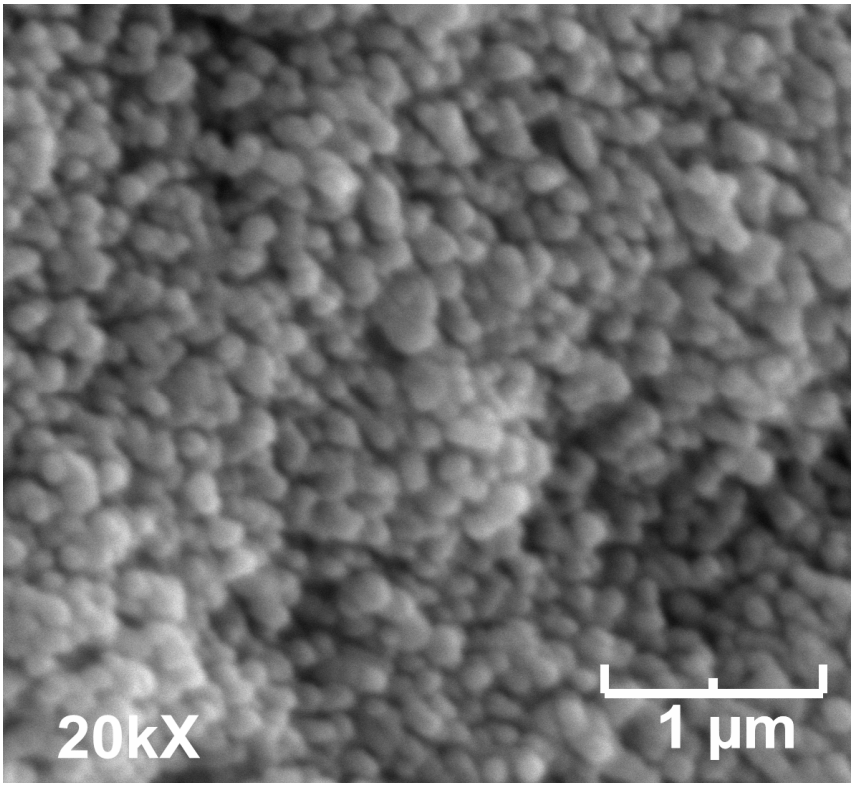

Figure 7.12. SEM image of the top surface of the BZCYYb-modified BSC anode scaffold wall prior to reduction or operation.

lower porosity, and higher "interconnectedness" than its unmodified counterpart, indicating that the BZCYYb modification affected the sintering characteristics of the overall anode layer. The modified anode's improvement in overall performance could be attributed to these aspects, particularly smaller grain size, as the number of interfaces between the anode layer and underlying YSZ scaffold would be increased. If the fuel gas molecules could reach these extra interfaces, the number of TPBs is effectively increased.

Figure 7.13 presents a comparison between the BZCYYb-modified and blank Ni anode surfaces after operation in CH_4 fuel. The modified anode was relatively clean following operation. In the micrograph, small discrete particles can be seen covering the surface of the porous, interconnected Ni layer; these particles are likely BZCYYb, which

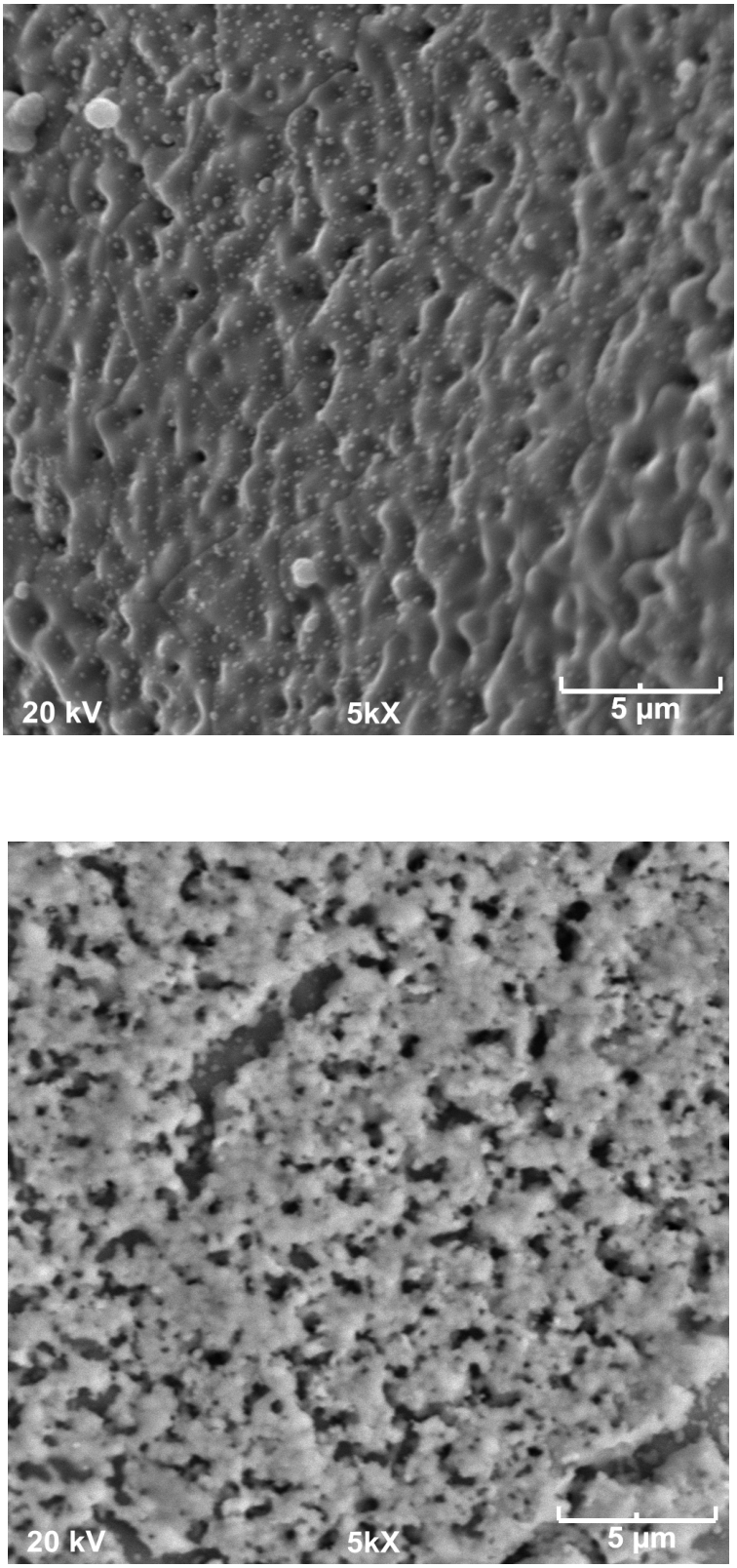

Figure 7.13. SEM images of the top surface of BZCYYb-modified Ni anode (top) and unmodified Ni anode (bottom) following operation in CH_4 at 700ºC.

helped prevent anode degradation by coking. Meanwhile, the unmodified Ni anode displayed a microstructure that appeared more disintegrated, suggesting coking-related anode degradation by a dissolution-reprecipitation mechanism[26].

In addition to the above investigations, the sulfur poisoning tolerance of each type of anode was tested by monitoring the stability of each cell's current over time while operating in wet H_2S-containing H_2 fuel. Figure 7.14 summarizes the results of the sulfur poisoning and recovery tests for the blank and BZCYYb-modified Ni anodes. The performance of the cell with the plain Ni anode decreased by 10% upon exposure to 10 ppm H_2S and 20% in 20 ppm H_2S. Increasing the H_2S concentration beyond 20 ppm did not yield much more performance loss. When H_2S was removed from the H_2 gas flow,

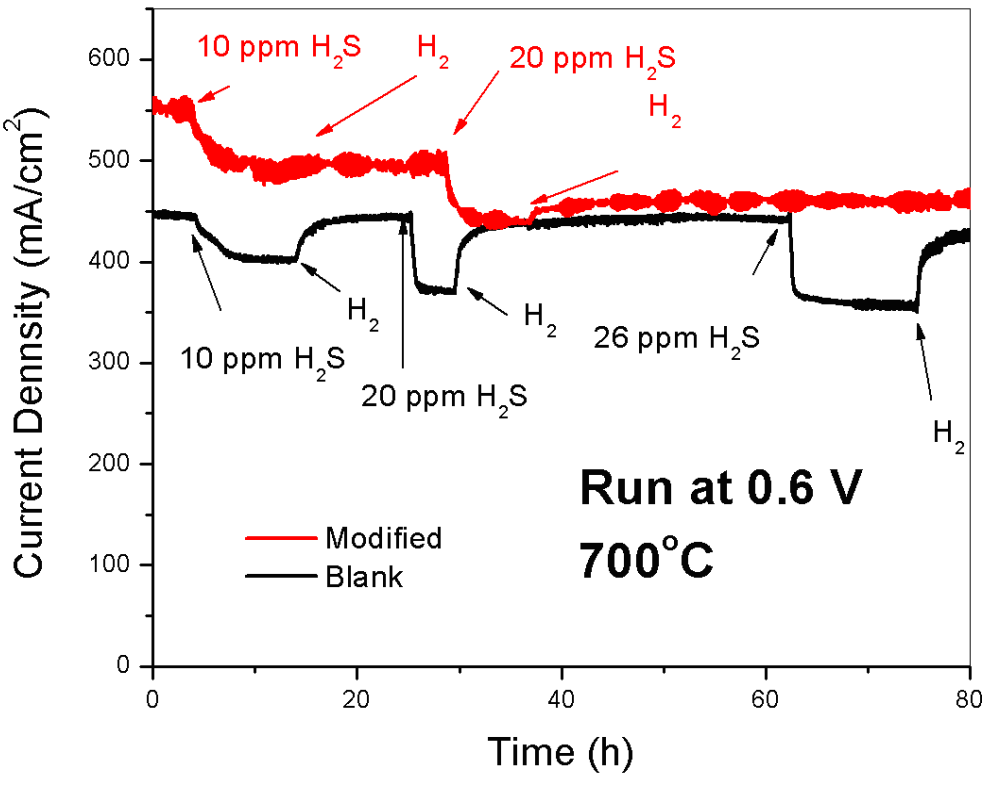

Figure 7.14. Operation stability over time of cells containing BZCYYb-modified Ni and Ni anodes cycled in H_2 with and without ppm-level H_2S content.

the blank cell's performance typically recovered almost fully within ~5 hours. The recovery period was slightly faster than is average for typical cells with thick anodes. This phenomenon was likely due to the relative openness and lack of tortuosity in the pore structure of the BSC electrode, which would allow for faster gas diffusion and subsequent elimination of sulfur species from the system.

Unfortunately, the BZCYYb modification did not add sulfur tolerance to the system as was originally hoped. In fact, while the performance loss for the BZCYYb-modified cell was similar to the blank anode case, the modified cell showed little to no recovery upon removal of the H_2S gas. The lack of recovery suggests that the BZCYYb or some impurity within the modification reacts with the H_2S and forms a secondary phase that permanently poisons the electrode. Contrast between Raman spectra collected from each type of anode's surface following operation (Figure 7.15) supports this notion; while no considerable Raman signal can be discerned from the blank anode's spectrum, a broad band between 300 and 600 cm^{-1} is observable on the modified anode's spectrum, possibly corresponding to some sulfide phases.

The exacerbation of sulfur poisoning on the Ni BSC anode by the BZCYYb starkly contrasts with the precedent for excellent sulfur tolerance modification by Ni-BZCYYb anodes. This finding raises the possibility that while the BZCYYb phase formed under the modification treatment conditions, the conversion from the precursors may not have been complete, leaving behind excess oxides like BaO that could easily react with H_2S in the fuel. Given the number of components and that the material is more similar to the less stable barium cerate than barium zirconate, a higher temperature might be needed to achieve a stable, complete BZCYYb phase. Meanwhile, the BSC

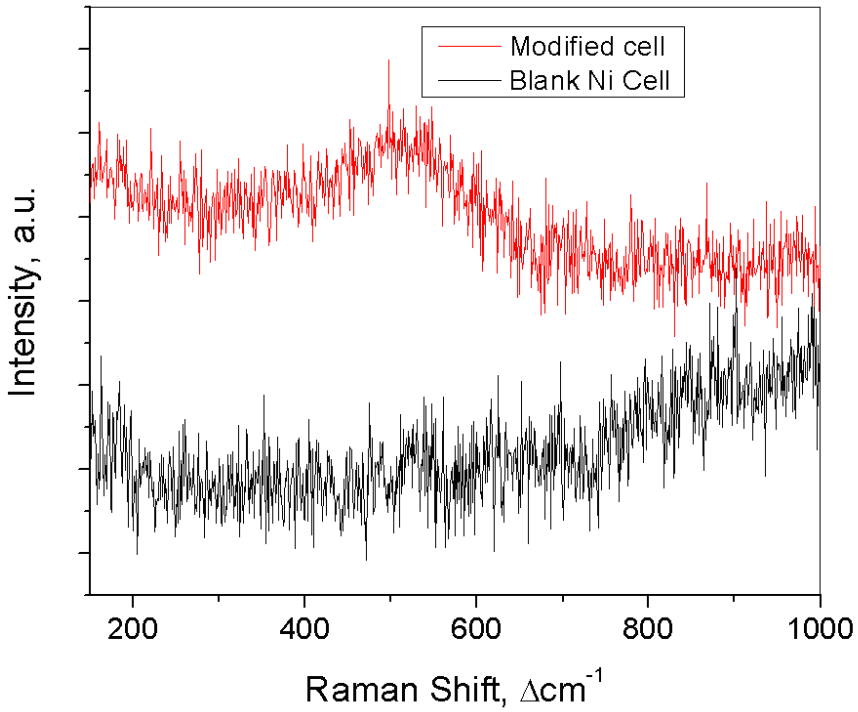

Figure 7.15. Raman spectra collected from unmodified and BZCYYb-modified cells following operation in wet H_2S-containing H_2 fuel at 700ºC.

architecture is limited in terms of allowable firing temperature. Heating the scaffold too far above 1000°C could lead to over-sintering of the anode layer. Therefore, selection of a different material for sulfur tolerance might be warranted.

7.4. BZYb-modified BSC anodes

In previous research, the use of Yb-doped barium zirconates has been generally limited to proton-conducting electrolytes.[138-140] For this work, BZYb was chosen as one modifying material for the anode due to the relative stability and simplicity of $BaZrO_3$, the utility of the similar Y-doped $BaZrO_3$ as a coking-tolerant material[7], and the inclusion of the Yb element. Again, the latter characteristic might be the key to high sulfur

poisoning tolerance. Like the BZCYYb case, a relatively dilute solution (0.03 *M*) was used to prevent detriment to the overall conductivity of the electrode.

Figure 7.16 shows a Raman spectrum and XRD pattern obtained from BZYb powder calcined at 1000ºC from the modification solution. The XRD pattern matches the one found by Ahmed and co-workers in their study of $BaZr_{0.9}Yb_{0.1}O_{3-\delta}$ and confirms that the material's overall structure matches the space group $Pm\bar{3}m$.[140] Again, though no Raman lattice phonon modes are predicted by group theory for this material, the doping-induced defects likely produce the broad features that are visible in the spectra. These features occupy similar positions to those seen in spectra from BZY (Figure 5.10 in Chapter 5). Thus, the desired phase was achieved from the modification solution.

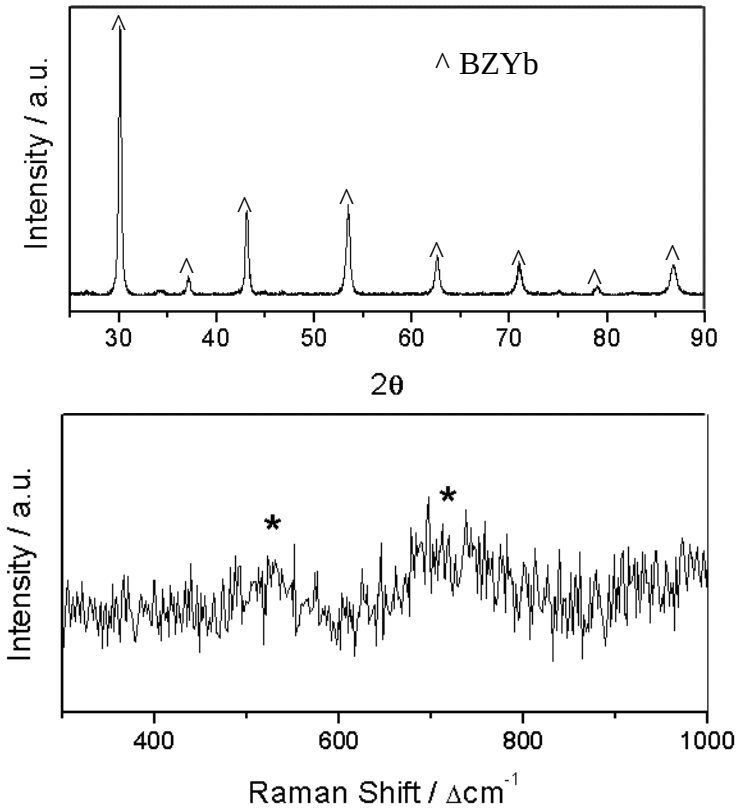

Figure 7.16. XRD pattern (top) and Raman spectrum (bottom) collected from BZYB powder calcined from solution.

As with the other modified cells, BZYb-infiltrated cells exhibited stable operation in low-order hydrocarbon fuel at high temperatures. The performance of these cells was also superior. As such, larger "full-slab" cells with this modification were tested using NASA's methodology. Figure 7.17 presents a comparison of the performances in H_2 and CH_4 fuels between large cells with unmodified and BZYb-modified anodes. The modified cells showed nearly 100% improvement in both cases. The BZYb-modified cell also showed good stability over time when operated in wet CH_4 at 800ºC compared to the blank cell, which displayed a sharp performance decrease after less than one hour of testing (Figure 7.18).

The absolute power density values seen here are lower than those observed for the BZCYYb button cells (Figure 7.7), but this result was expected; measured power density tends to decrease with increase in active electrode area. A better metric for this case might be fuel utilization, which can be calculated as follows:

$$U_{fuel} = 2.24*10^4 * \frac{jA}{0.97*nF\dot{V}} \qquad (7\text{-}1)$$

A is the active electrode area of the cell in cm^2, $\dot{V}$ is the flow rate of the fuel in cm^3/s, F is Faraday's constant, j is current density expressed in A/cm^2, and n is the number of charges required to completely oxidize a molecule of fuel (2 for H_2 and 8 for CH_4). The factor $2.24*10^4$ accounts for the assumption that the fuel flow behaves like a room-temperature ideal gas, and the 0.97 factor corresponds to 3% H_2O already in the wet fuel stream. This equation also carries the assumptions that the fuel gas pressure is near atmospheric level and the oxidant flow cannot limit the cell reaction. Since the cathode is flooded with air in NASA's testing method, the latter is a fair assumption. Finally, in the

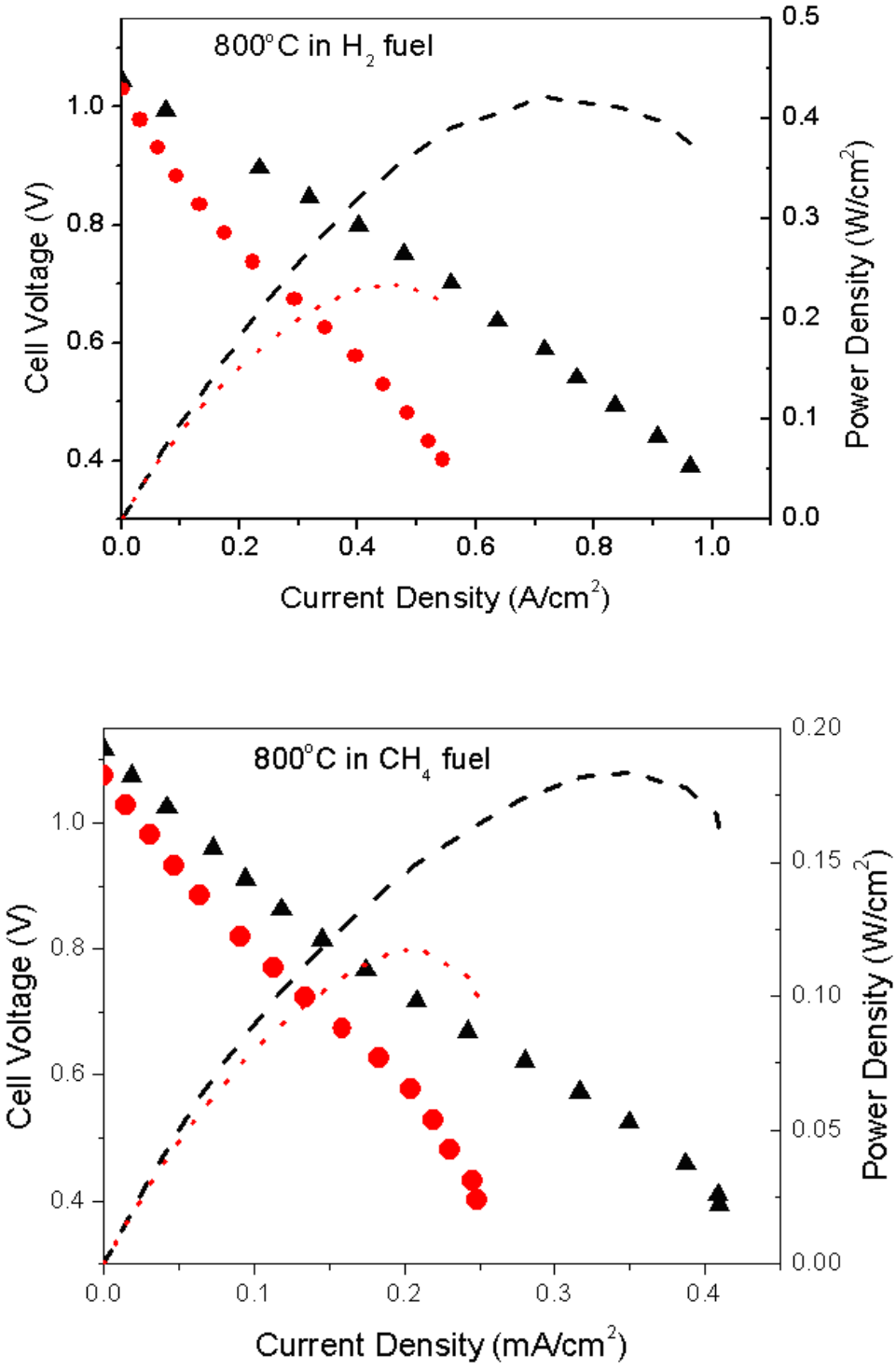

Figure 7.17. Current-voltage and power density curves for unmodified (red trace) and BZCYYb-modified (black trace) large cells operating in wet H_2 (top) and CH_4 (bottom) fuels at 800ºC.

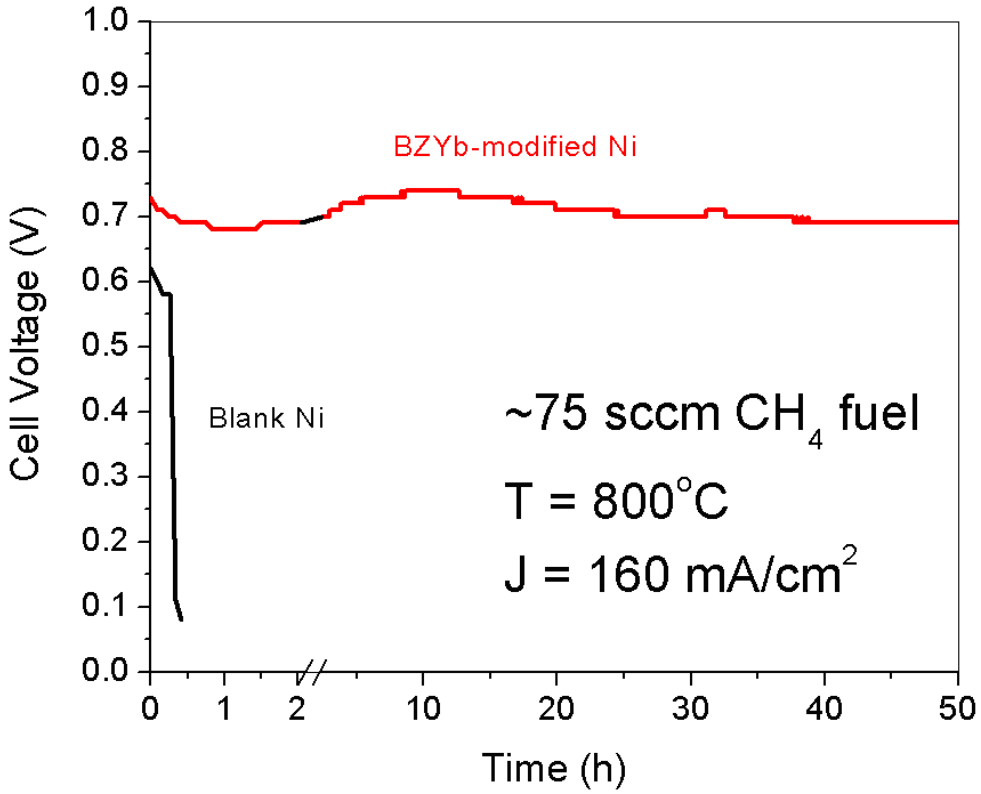

Figure 7.18. Stability over time of unmodified and BZYb-modified large cells operating in wet CH_4 fuel at 800ºC.

case of CH_4 oxidation, a direct oxidation assumption is not too far from reality as the eventual products are water and oxides of carbon. Fuel utilization calculated at peak power density for the BZYb-modified large cell operating at 800ºC was ~23% and ~11% for H_2 and CH_4, respectively. The CH_4 fuel utilization value, in particular, was relatively high compared to those found in contemporary literature for similar Ni-YSZ systems operated at 800ºC, which were anywhere between <1% and 6%.[141, 142]

After electrochemical testing, the large cells' anodes were characterized by SEM. Figure 7.19 displays SEM images collected from the surface of the scaffold walls of each type of anode after operation in CH_4. Again, the unmodified anode's structure degraded considerably as a result of aggressive coking; the porous Ni anode layer disintegrated into

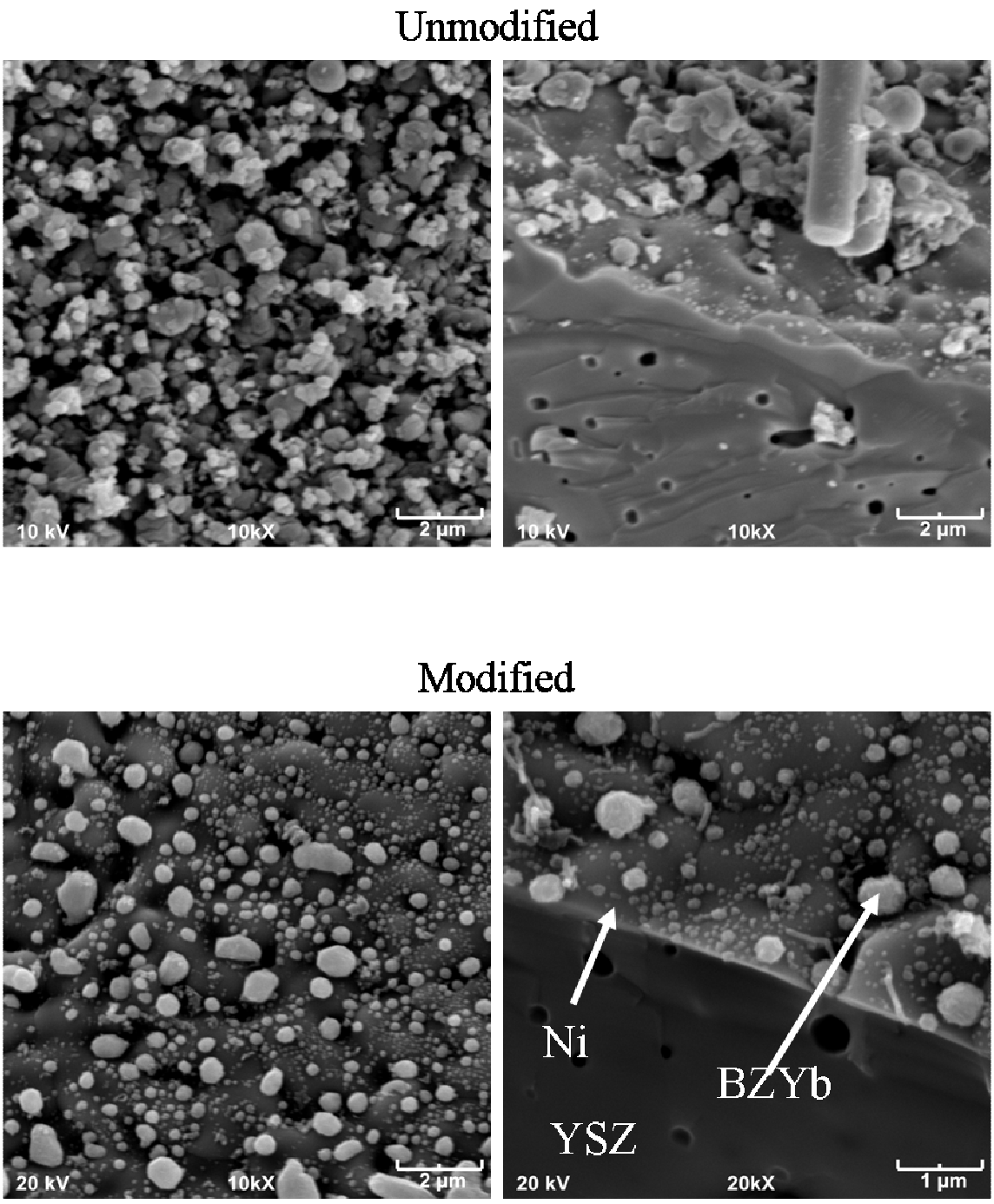

Figure 7.19. SEM images of the top surface of unmodified Ni anode (top) and BZYb-modified Ni anode (bottom) following operation of large cells in CH_4 at 800ºC.

relatively isolated granules. In addition, the fiber that can be seen in the upper-right micrograph is likely fibrous carbon. In contrast, for the BZYb-modified anode, the porous Ni layer was left intact. Spheroid-shaped particles decorate the top of the anode layer; these particles are likely BZYb.

Raman spectroscopy was used to probe for the presence of carbon on the anodes after CH_4 operation. Figure 7.20 shows Raman spectra obtained from each anode. In the unmodified anode, sharp D-band and G-band carbon peaks superimposed over the YSZ bands clearly indicate carbon deposition. These peaks are not visible in the spectrum from the modified sample. Meanwhile, the shoulder near 700 cm^{-1} protrudes more for the modified sample spectrum, indicating the presence of the same weak band at 720 cm^{-1} seen in Figure 7.16. This feature therefore can be assigned to the BZYb modification.

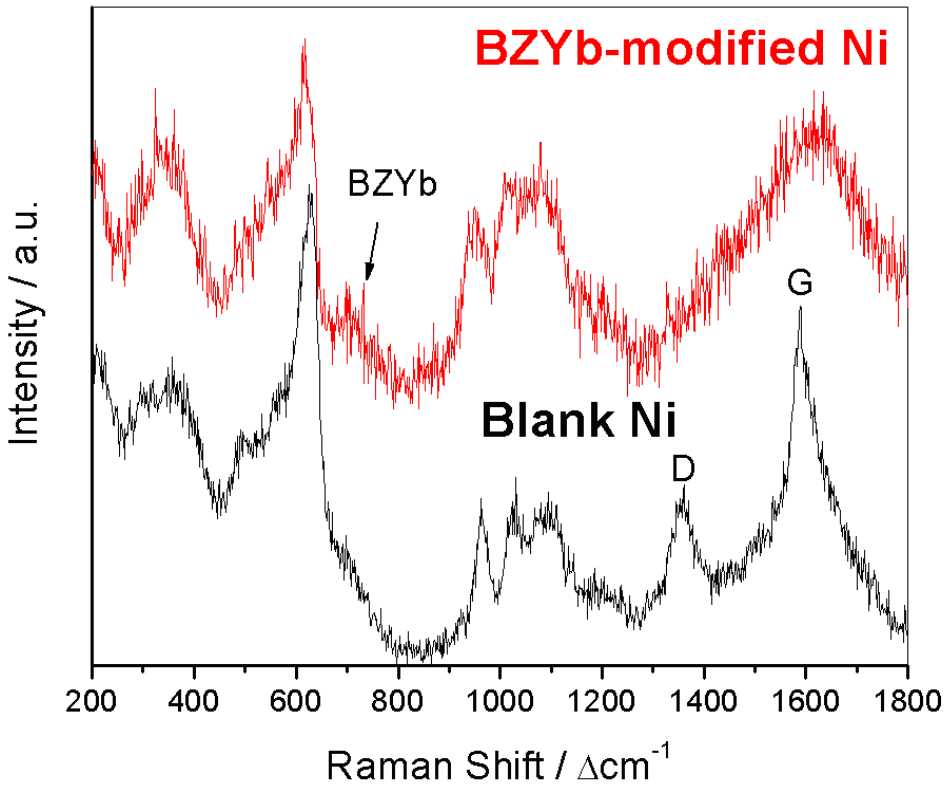

Figure 7.20. Raman spectra collected from unmodified and BZYb-modified large cells following operation in CH_4 fuel at 800ºC.

Sulfur tolerance tests were performed on the BZYb-modified anode using button-sized cells. Figure 7.21 displays the results of a typical poisoning and recovery test with 20 ppm H_2S in the gas feed. The performance only dropped by 10%, which is a better result compared with the blank and BZCYYb-modified anodes, which each had a performance drop of 20%. In addition, unlike the BZCYYb-modified cell, the BZYb-modified cell almost fully recovered its performance after removal of the H_2S from the fuel stream.

Since the BZYb modification gave the best results overall out of the three types described here, a BZYb-modified cell was briefly tested under a fuel that was closer to the condition of what one might expect for jet fuel. The initial fuel composition for the test was 70% CH_4 / 30% H_2. 30 ppm H_2S was added to the fuel stream after the first hour of testing. The results are shown in Figure 7.22; again, only a 10% drop in performance was seen with the introduction of H_2S, and the output was otherwise relatively stable.

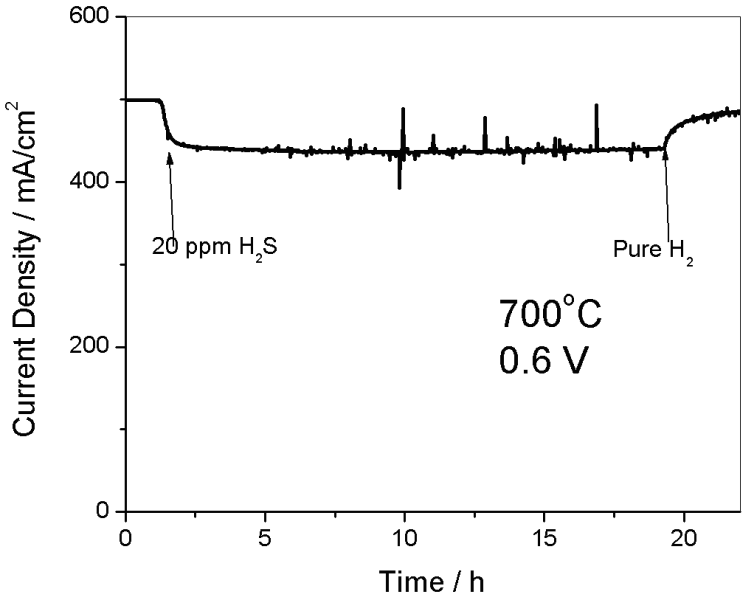

Figure 7.21. Operation stability over time of a cell containing a BZYb-modified Ni in H_2 with and without 20 ppm H_2S content.

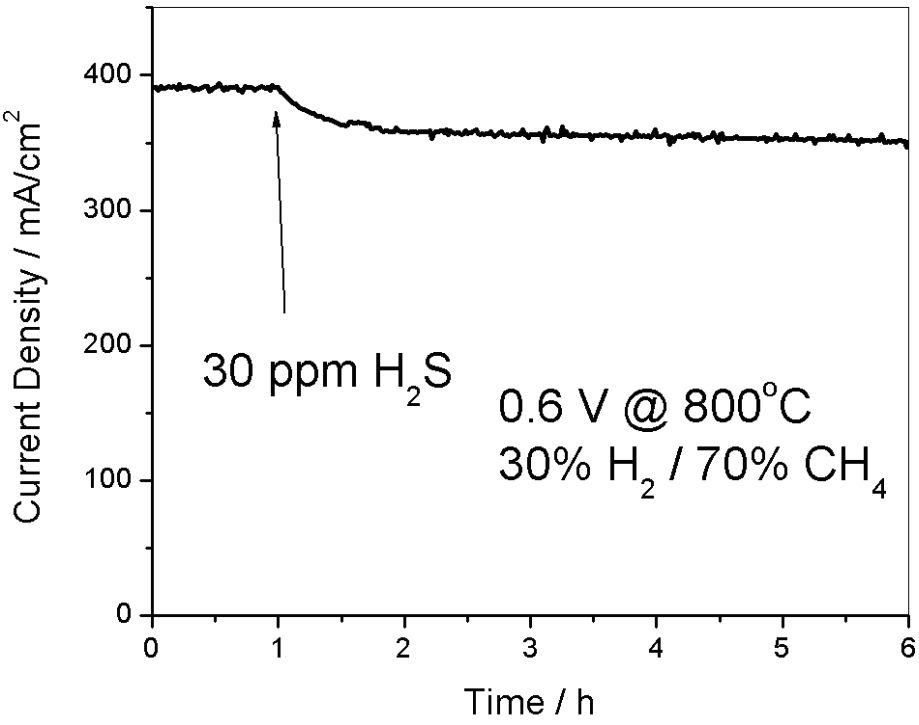

Figure 7.22. Stability of a cell containing a BZYb-modified Ni in H_2 with and without 20 ppm H_2S content.

Finally, the cell that was tested in the H_2S-containing CH_4 / H_2 fuel was analyzed by Raman spectroscopy, and the results are shown in Figure 7.23. This cell was aged in the same manner as the mesh cells tested for sulfur poisoning in Chapter 5 in order to form sulfate groups from any adsorbed sulfur before testing. The features in the spectrum are largely the same as the BZYb-modified anode spectrum shown in Figure 7.20 with no indication of carbon deposition. On the other hand, formation of sulfate groups was inconclusive since the 900-1200 cm^{-1} region of the spectrum is swamped by strong higher-order Raman peaks originating from the underlying YSZ.

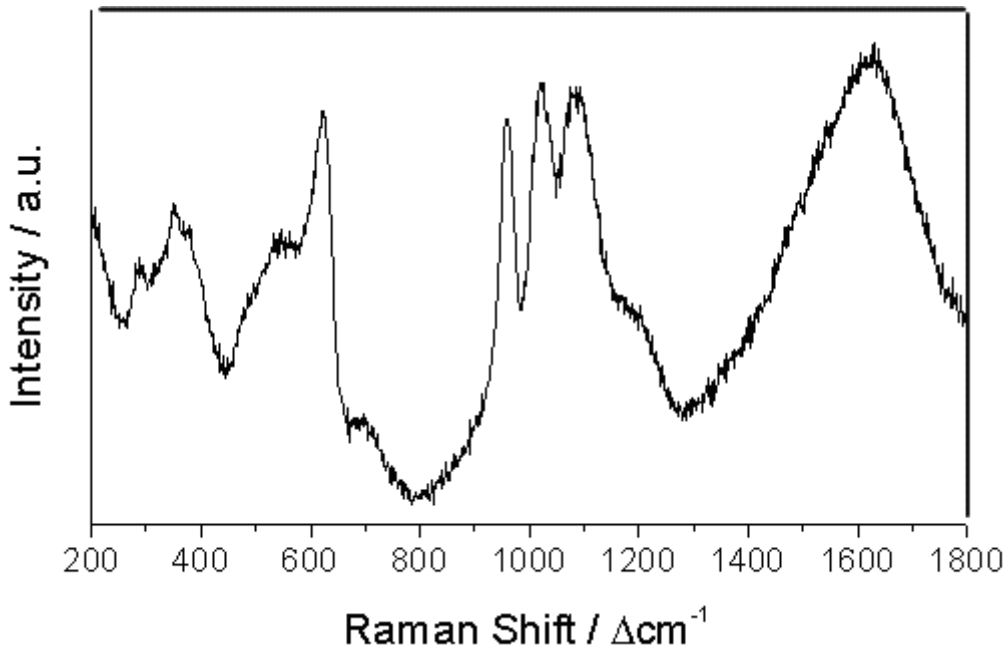

Figure 7.23. Raman spectrum collected from a BZYb-modified anode following operation in 70% CH_4 / 30% H_2 / 30 ppm H_2S fuel at 800ºC and aging for ~3 weeks in air at room temperature.

7.5. Summary of findings and future considerations

This work has demonstrated that oxides containing Ba and Yb can be successfully infiltrated into BSC-structured cell anodes, and all of these oxides provide considerable coking resistance. On the other hand, the BZCYYb did not provide the expected sulfur poisoning resistance. The calcination temperature was likely not high enough to form a stable BZCYYb modification, and unconverted oxide likely reacted with the H_2S to form undesired phases. Unfortunately, increasing the calcination temperature too much would compromise the overall cell architecture from oversintering of the anode layer. Meanwhile, the 4Ba-3Yb modification was not explored for sulfur tolerance properties for similar reasons, since the modification formed was found to be a mix of $BaCO_3$ and Yb_2O_3. The $BaCO_3$ in particular suggests the presence of BaO, which was found to

potentially form $BaSO_4$ when exposed to H_2S. Hence, permanent sulfur poisoning would likely be observed for that system as well. In contrast, a BZYb-based modification proved to be a viable option. BZYb, which has not heretofore been used as an anode modification material, gave the best overall cell performance improvement, conveyed some additional sulfur tolerance to the system, and did not cause the anode to suffer permanent sulfur poisoning. Further, this modification allowed for H_2 and CH_4 fuel utilization values of about 23% and 11%, respectively. Therefore, this material system might provide a good avenue for future study.

CHAPTER 8: CONCLUSIONS AND RECOMMENDATIONS

The first overall objective was the further development and demonstration of Raman spectroscopy as a tool for characterizing SOFC electrode surfaces beyond the preliminary work that has been performed along this route. Indeed, some new advances were made along this direction. First, water and OH groups were successfully detected on Ba-containing oxides under different temperature and electrochemical conditions. In addition, carbon deposition on Ni anodes as a result of operating under hydrocarbon fuels was mapped and monitored in real time while the role of water in coking resistance conveyed by Ba-containing oxides was confirmed. Further, Raman mapping helped support the hypothesis that sulfur poisoning of plain Ni anodes occurs by minute amounts of adsorbed sulfur species on the surface rather than by sulfide conversion. On the other hand, Raman spectroscopy suggested that when Ba-containing oxides are used in anodes operated in sulfur-containing fuels, the poisoning mechanism is different and can become permanent due to sulfide or sulfate formation. Finally, SERS methodologies were explored for boosting signal from surface species on both the cathode and anode. Sputtered Ag nanoparticles applied to cathode materials resulted in the emergence of peaks associated with adsorbed oxygen species that could not be seen before. This particular result is not without a caveat, however; due to the catalytic activity of Ag, the actual source of the adsorbed oxygen remains in question. $Ag@SiO_2$ core-shell nanoparticles provide a possible alternative. On the anode side, adsorbed hydrocarbons were successfully detected at high temperature when they couldn't be before, showing

this methodology's utility towards further investigating coking and sulfur poisoning mechanisms.

The second major objective was to use the knowledge gained about materials resistant to coking and sulfur poisoning and apply it to the development of NASA BSC-type cells. The rationale was to combine the architecture's overall performance potential with fuel flexibility. This aim was achieved by modifying the existing anode solution infiltration process with the incorporation of oxides containing Ba and Yb, and the results were mixed. The 3Ba-4Yb modification gave decent coking tolerance, but hampered overall performance. Further, the desired phase was not achieved for this case. The BZCYYb modification provided reasonable performance enhancement and coking resistance, but surprisingly exacerbated the sulfur poisoning problem. In contrast, the BZYb modification enhanced sulfur poisoning tolerance, gave great performance gains (almost 100% at 800ºC), and stability while operating under a fuel containing both hydrocarbons and H_2S that simulated jet fuel conditions. For large cell tests, the BZYb-modified cells showed peak fuel utilizations of ~23% and ~11% for H_2 and CH_4 fuels respectively, which were higher values than achieved for Ni-YSZ anodes reported by others. The BZYb system, which to the author's knowledge had not been incorporated into SOFC anodes before this work, is a good candidate for future explorations in modifying anodes that have BSC or even other architectures; for example, BZYb-modified anodes with varying Yb content could be tested for performance, coking resistance, and sulfur poisoning tolerance. In addition, the connection between intrinsic material properties (i.e. water adsorption capability, mass transport), structure, and

tolerance characteristics of such modifications might be investigated in order to find the optimal conditions.

For future work along the Raman spectroscopy direction, *in situ* SERS-assisted Raman investigations by $Ag@SiO_2$ or other suitable core-shell nanoparticles are definitely worth exploring further. To frame one example, the coking resistance mechanism proposed in Yang *et al.*[6] contains one theoretical reaction that forms a carboxyl group (COH) which helps eliminate the carbon from the surface. If this reaction truly happens, the amount of carboxyls present at any given time is likely under the detection limit of normal Raman, especially at high temperatures. Thus, probing for these under fuel cell operating conditions might normally be a fruitless endeavor. With $Ag@SiO_2$ nanoparticles present on the surface, however, detecting these intermediates becomes a possibility. In the case of sulfur poisoning, with these nanoparticles, aging samples in order to form species that are just barely detectable by *ex situ* Raman spectroscopy might no longer be necessary. Rather, one would be able to directly detect the sulfur *in situ* as it becomes adsorbed by the Ni. Of course, in order for these experiments to be effective, SERS treatment reproducibility and proper calibration to eliminate the contribution of surface species directly adsorbed on treatment nanoparticles would be essential.

More experiments under realistic electrochemical conditions are also recommended for ongoing work. The Ni mesh electrode design described in Chapter 6 would likely facilitate the success of such experiments.

In terms of interpreting Raman spectra in future work, group theory is useful for predicting where Raman peaks are expected to appear. Unfortunately, as some of the

results in this dissertation demonstrated, group theory does not help with complete interpretation, especially when dealing with defective materials. In addition, surface species may have a slightly different Raman shift from their “free-space” vibrational modes based on the type of surface they are attached. In these cases, proper quantum chemical calculations like those referred to in Chapter 5 used to predict the Raman modes of water on BaO are warranted.

In short, the main scientific contributions of this work to the field include:

- Further elucidation of how and where carbon and sulfur deposits during anode degradation
- Confirmation of the role of water in coking and sulfur poisoning mechanisms
- A promising SERS methodology for boosting signal from trace amounts of species that is applicable to both fuel cell electrodes as well as other high-temperature catalysis systems
- A new material system with promising applications in anode coking and sulfur poisoning tolerance

Overall, the results presented in this dissertation have also demonstrated that with properly designed experiments, Raman spectroscopy is a useful tool for gaining some of the insights needed for a rational approach to designing better SOFC electrode materials.

APPENDIX A: RAMAN MODES OF INTEREST TO SOFC STUDY

Table A.1. Raman-active lattice phonon and vibrational modes for various species and phases of interest to SOFCs.

Phase / Species	Group	Raman Modes	Main Peak(s)*
YSZ	O_h^6	F_{2g}	620
SDC	O_h^6	F_{2g}	460
LSM (La/Sr: 0.85/0.15)	D_{2h}^{16}	$7A_g + 5B_{1g} + 7B_{2g} + 5B_{3g}$	535
LSM (La/Sr: 0.8/0.2)	D_{3d}^6	$A_g + 4\ E_g$	697, 520
LSCF	D_{3d}^6	$A_g + 4\ E_g$	646, 525
BZCYYb	D_{2h}^{16}	$7A_g + 5B_{1g} + 7B_{2g} + 5B_{3g}$	335
BZY	O_h^2	None	720**
BZYb	O_h^2	None	725**
C (Graphite)	D_{6h}^5	E_{2g}	1585
H_2O	C_2	$2A_1 + B_2$	3716, 3368, 1594
O_2	D_2	A_g	1598
SO_4^{2-}	T_d	$A_1 + E + 2F_2$	980
CO_3^{2-}	D_{3h}	$A_{1g} + 2E$	1059
C_3H_8	C_{2v}	$xA_1 + yB_2$	1528
C_2H_4	D_{2h}	$3A_g + B_{1g} + 2B_{3g}$	1425
COH	C_s	$2A_1 + A_2$	2483***
BaO_2	D_{4h}^{17}	$A_{1g} + E_g$	240, 800***

*Approximate positions of experimentally observed peaks

**Peaks were observed but not predicted by group theory; bands are likely defect-induced

***Not experimentally observed; cited from references[58, 107]

APPENDIX B: SUPPLEMENTARY RESULTS

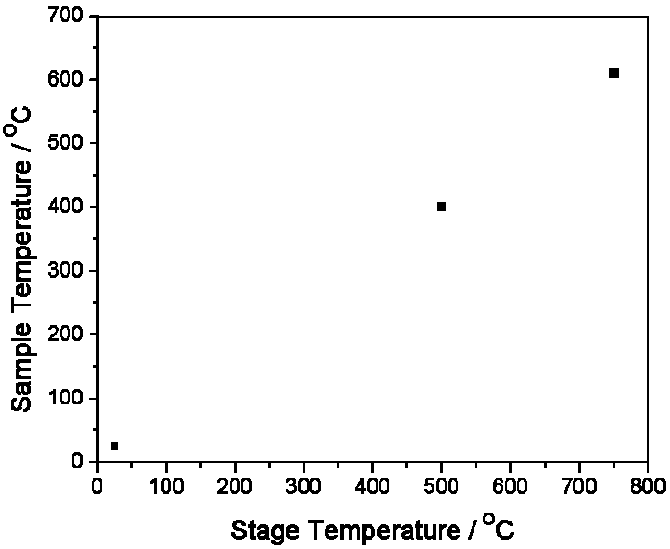

Figure B.1. Sample calibration data showing the temperature difference between the temperature measured by the Raman chamber's thermocouple and the actual sample surface temperature.

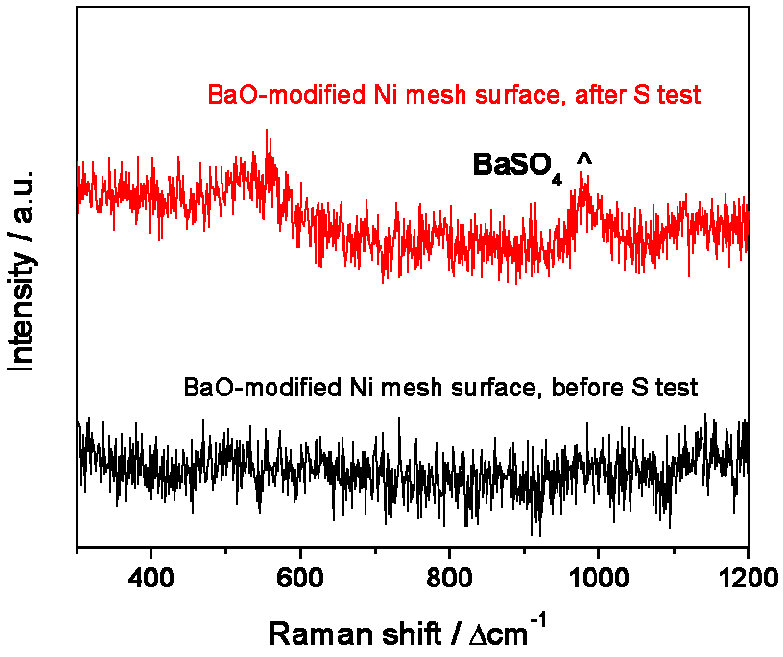

Figure B.2. Raman spectra collected from BaO-modified Ni mesh cell surface before and after operation in H_2S-containing fuel.

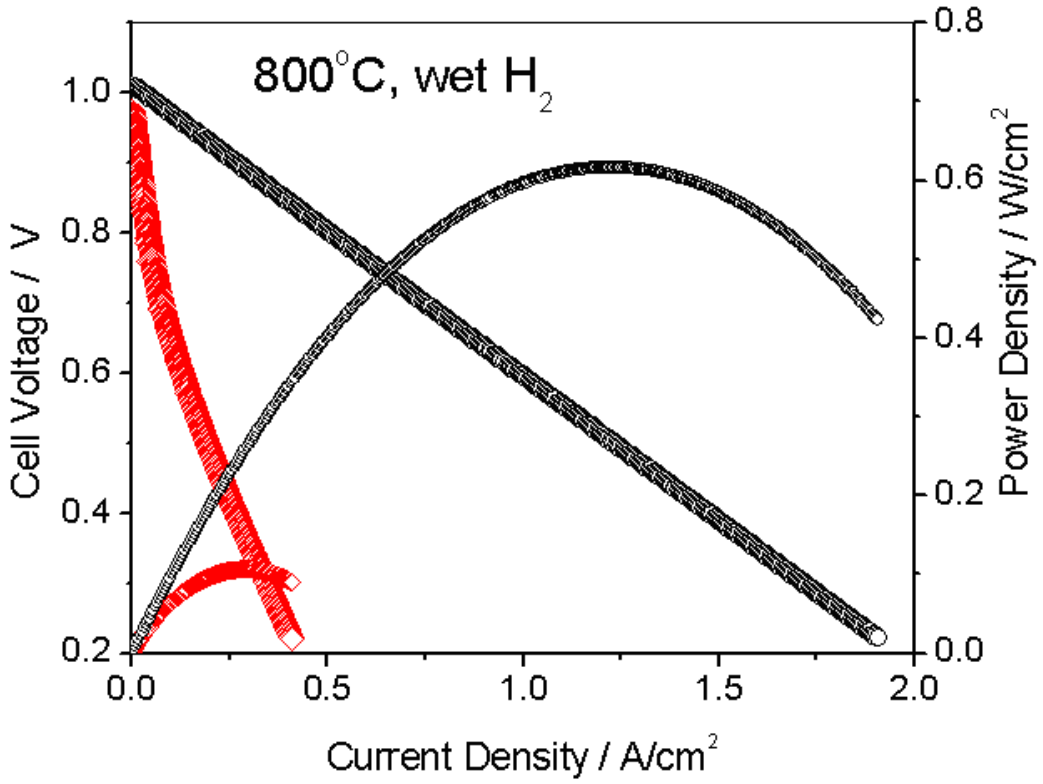

Figure B.3. Current-voltage and power density curves for unmodified (black trace) and cells modified with heavily concentrated BZCYYb (red trace) operating in wet H_2 at various temperatures.

REFERENCES

1. "Annual Energy Review," *U.S. Department of Energy* (2010).

2. Liu, M., Lynch, M. E., Blinn, K., Alamgir, F., & Choi, Y., "Rational SOFC material design: new advances and tools," *Materialstoday* **14** (11), 534-546 (2011).

3. Minh, N. Q., "Solid oxide fuel cell technology-features and applications," *Solid State Ionics* **174** (1-4), 271-277 (2004).

4. Singhal, S. C., "Solid oxide fuel cells for stationary, mobile, and military applications," *Solid State Ionics* **152** 405-410 (2002).

5. Yang, L., Wang, S., Blinn, K., Liu, M., Liu, Z., Cheng, Z., & Liu, M., "Enhanced Sulfur and Coking Tolerance of a Mixed Ion Conductor for SOFCs: $BaZr_{0.1}Ce_{0.7}Y_{0.2-x}Yb_xO_{3-d}$," *Science* **326** 126-129 (2009).

6. Yang, L., Choi, Y., Qin, W., Chen, H., Blinn, K., Liu, M., Liu, P., Bai, J., Tyson, T. A., & Liu, M., "Promotion of water-mediated carbon removal by nanostructured barium oxide/nickel interfaces in solid oxide fuel cells," *Nature Communications* **2** 357 (2011).

7. Liu, M. F., Choi, Y. M., Yang, L., Blinn, K., Qin, W., Liu, P., & Liu, M. L., "Direct octane fuel cells: A promising power for transportation," *Nano Energy* **1** 448-455 (2012).

8. Lin, Y., Zhan, Z., Liu, J., & Barnett, S. A., "Direct operation of solid oxide fuel cells with methane fuel," *Solid State Ionics* **176** (23-24), 1827-1835 (2005).

9. McIntosh, S. & Gorte, R., "Direct Hydrocarbon Solid Oxide Fuel Cells," *Chemical Reviews* **104** (10), 4845-4865 (2004).

10. Gur, T. M., Homel, M., & Virkar, A. V., "High performance solid oxide fuel cell operating on dry gasified coal," *Journal of Power Sources* **195** (4), 1085-1090 (2010).

11. Homel, M., Gur, T. M., Koh, J. H., & Virkar, A. V., "Carbon monoxide-fueled solid oxide fuel cell," *Journal of Power Sources* **195** (19), 6367-6372 (2010).

12. Minh, N. Q. & Takahashi, T., Science and Technology of Fuel Cells, Amsterdam: Elsevier, 1995.

13. Huijsmans, J. P. P., Berkel, F. P. F. v., & Christie, G. M., "Intermediate temperature SOFC - a promise of the 21st century," *Journal of Power Sources* **71** (1), 107-110 (1998).

14. Will, J., Mitterdorfer, A., Kleinlogel, C., Perednis, D., & Gauckler, L. J., "Fabrication of thin electrolytes for second-generation solid oxide fuel cells," *Solid State Ionics* **131** (1-2), 79-96 (2000).

15. Liu, M. L., "Equivalent circuit approximation to porous mixed-conducting oxygen electrodes in solid-state cells," *Journal of The Electrochemical Society* **145** (1), 142-154 (1998).

16. Bard, A. J. & Faulkner, L. R., Electrochemical Methods: Fundamentals and Applications, New York: Wiley, 2000.

17. Alzate-Restrepo, V. & Hill, J., "Effect of anodic polarization on carbon deposition on Ni/YSZ anodes exposed to methane," *Applied Catalysis A: General* **342** (1-2), 49-55 (2008).

18. Zha, S. W., Cheng, Z., & Liu, M. L., "Sulfur poisoning and regeneration of Ni-based anodes in solid oxide fuel cells," *Journal of The Electrochemical Society* **154** (2), B201-B206 (2007).

19. Su, C., Ran, R., Wang, W., & Shao, Z. P., "Coke formation and performance of an intermediate-temperature solid oxide fuel cell operating on dimethyl ether fuel," *Journal of Power Sources* **196** 1967-1974 (2011).

20. Cheng, Z., Wang, J.-H., Choi, Y. M., Yang, L., Lin, M. C., & Liu, M., "From Ni-YSZ to sulfur-tolerant anodes for SOFCs: electrochemical behavior, in situ characterization, modeling, and future perspectives," *Energy & Environmental Science* **4** (11), 4380-4409 (2011).

21. Cimenti, M. & Hill, J. M., "Direct utilization of liquid fuels in SOFC for portable applications: challenges for the selection of alternative anodes," *Energies* **2** (2), 377-410 (2009).

22. Galea, N. M., Knapp, D., & Ziegler, T., "Density functional theory studies of methane dissociation on anode catalysts in solid-oxide fuel cells: Suggestions for coke reduction," *Journal of Catalysis* **247** (1), 20-33 (2007).

23. Kim, J.-S., Nair, V. V., Vohs, J. M., & Gorte, R. J., "A study of the methane tolerance of LSCM-YSZ composite anodes with Pt, Ni, Pd, and ceria catalysts," *Scripta Materiala* **65** 90-95 (2011).

24. Liu, J., Birss, V., & Hill, J., "Electrochemical Performance and Microstructure Characterization of Nickel Yttrium-Stabilized Zirconia Anode," *AIChE Journal* **56** (6), 1651-1658 (2010).

25. Rasmussen, J. F. B. & Hagen, A., "The effect of H_2S on the performance of Ni-YSZ anodes in solid oxide fuel cells," *Journal of Power Sources* **191** (2), 534-541 (2009).

26. Toebes, M. L., Bitter, J. H., Dillen, A. J. v., & Jong, K. P. d., "Impact of the structure and reactivity of nickel particles on the catalytic growth of carbon nanofibers," *Catalysis Today* **76** 33-42 (2002).

27. Wang, J. & Liu, M. L., "Computational study of sulfur-nickel interactions: a new S-Ni phase diagram," *Electrochemistry Communications* **9** (9), 2212-2217 (2007).

28. Sasaki, K., Susuki, K., Iyoshi, A., Uchimara, M., Imamura, N., Kusaba, H., Tereoka, Y., Fuchino, H., Tsujimoto, K., Uchida, Y., & Jingo, N., "H_2S poisoning of solid oxide fuel cells," *Journal of The Electrochemical Society* **153** A2023-A2029 (2006).

29. Yang, L., Wang, S. Z., Blinn, K., Liu, M. F., Liu, Z., Cheng, Z., & Liu, M. L., "Enhanced Sulfur and Coking Tolerance of a Mixed Ion Conductor for SOFCs: BaZr0.1Ce0.7Y0.2-xYbxO3-delta," *Science* **326** (5949), 126-129 (2009).

30. Zhen, Y. D., Li, J., & Jiang, S. P., "Oxygen reduction on strontium-doped $LaMnO_3$ cathodes in the absence and presence of an iron-chromium alloy interconnect," *Journal of Power Sources* **162** 1043-1052 (2006).

31. Deseure, J., Bultel, Y., Dessemond, L., Siebert, E., & Ozil, P., "Modelling the porous cathode of a SOFC: oxygen reduction mechanism effect," *Journal of Applied Electrochemistry* **37** 129-136 (2007).

32. Nicolella, C., Reverberl, A. P., Carpanese, P., Viviani, M., & Barbucci, A., "Influence of the Temperature on Oxygen Reduction on SOFC Electrodes: Theoretical and Experimental Analysis," *Journal of Fuel Cell Science and Technology* **5** 011011-011015 (2008).

33. Ringuedé, A. & Fouletier, J., "Oxygen reaction on strontium-doped lanthanum cobaltite dense electrodes at intermediate temperatures," *Solid State Ionics* **139** (3-4), 167-177 (2001).

34. Sharmin, S., Irulappan, S., & Ilias, S., "Synthesis of Novel Electro-catalysts for Proton Exchange Membrane Fuel Cells," *Separation Science and Technology* **38** 2963-2977 (2003).

35. Liu, M. & Winnick, J., "Fundamental issues in modeling of mixed ionic-electronic conductors (MIECs)," *Solid State Ionics* **118** (1,2), 11-21 (1999).

36. Zhang, H. & Yang, W., "Highly efficient electrocatalysts for oxygen reduction reaction," *Chemical Communications* **2007** (41), 4215-4217 (2007).

37. Xia, C., Rauch, W., Chen, F., & Liu, M., "$Sm_{0.5}Sr_{0.5}CoO_3$ cathodes for low-temperature SOFCs," *Solid State Ionics* **149** (1,2), 11-19 (2002).

38. Gupta, R. K., Kim, E. Y., Noh, H. S., & Whang, C. M., "Mechanical, electrical, and micro-structural properties of La0.6Sr0.4Co0.2Fe0.8O3 perovskite-based ceramic foams," *Journal of Physics D: Applied Physics* **41** 032003 (2008).

39. Jiang, S. P., Love, J. G., Zhang, J. P., Hoang, M., Ramprakash, Y., Hughes, A. E., & Badwal, S. P. S., "The electrochemical performance of LSM/zirconia-yttria interface as a function of a-site non-stoichiometry and cathodic current treatment," *Solid State Ionics* **121** (1-4), 1 (1999).

40. Kim, J.-S. & Pyun, S.-I., "Effects of Secondary Phase and Thickness on Mixed Controlled Oxygen Reduction at Dense Composite Electrode," *Journal of The Electrochemical Society* **155** (1), B8-B15 (2008).

41. Lynch, M., Yang, L., Qin, W., Choi, J. J., Liu, M. F., Blinn, K., & Liu, M., "Enhancement of $La_{0.6}Sr_{0.4}Co_{0.2}Fe_{0.8}O_{3-\delta}$ Durability & Surface Electro-catalytic Activity by $La_{0.85}Sr_{0.15}MnO_{3-\delta}$ Investigated using a New Test Electrode Platform," *Energy & Environmental Science* **4** 2249-2258 (2011).

42. Liu, M. F., Ding, D., Blinn, K., Li, X., Nie, L., & Liu, M., "Enhanced performance of LSCF cathode through surface modification," *International Journal of Hydrogen Energy* **30** 8613-8620 (2012).

43. Sun, C. W., Hui, R., & Roller, J., "Cathode materials for solid oxide fuel cells: a review," *Journal of Solid State Electrochemistry* **14** (7), 1125-1144 (2010).

44. Niu, Y. J., Sunarso, J., Liang, F. L., Zhou, W., Zhu, Z. H., & Shao, Z. P., "A Comparative Study of Oxygen Reduction Reaction on Bi- and La-Doped SrFeO(3-delta) Perovskite Cathodes," *Journal of The Electrochemical Society* **158** (2), B132-B138 (2011).

45. Chen, D. J., Huang, C., Ran, R., Kwak, C., Shao, Z. P., & Park, H. J., "New Ba(0.5)Sr(0.5)Co(0.8)Fe(0.2)O(3-delta) + Co(3)O(4) composite electrode for IT-SOFCs with improved electrical conductivity and catalytic activity," *Electrochemistry Communications* **13** (2), 197-199 (2011).

46. Ju, Y. W., Inagaki, T., Ida, S., & Ishihara, T., "Sm(Sr)CoO(3) Cone Cathode on LaGaO(3) Thin Film Electrolyte for IT-SOFC with High Power Density," *Journal of The Electrochemical Society* **158** (7), B825-B830 (2011).

47. Choi, Y. M., Mebane, D. S., Lin, M. C., & Liu, M., "Oxygen Reduction on $LaMnO_3$-Based Cathode Materials in Solid Oxide Fuel Cells," *Chemistry of Materials* **19** (7), 1690-1699 (2007).

48. Lynch, M. E., Mebane, D. S., Liu, Y., & Liu, M., "Triple phase boundary and surface transport in mixed conducting patterned electrodes," *Journal of the Electrochemical Society* (in press, 2008).

49. Lynch, M. E., Ding, D., Harris, W. M., Lombardo, J. J., Nelson, G. J., Chiu, W. K. S., & Liu, M. L., "Flexible multiphysics simulation of porous electrodes: Conformal to 3D reconstructed microstructures," *Nano Energy* in press (2012).

50. Maher, R. C. & Cohen, L. F., "Raman spectroscopy as a probe of temperature oxidation state for gadolinium-doped ceria used in solid oxide fuel cells," *Journal of Physical Chemistry A* **112** (7), 1497-1501 (2008).

51. Tiwari, B., Dixit, A., & Kothiyal, G. P., "Study of glasses/glass-ceramics in the SrO-ZnO-SiO_2 system as high temperature sealant for SOFC applications," *International Journal of Hydrogen Energy* **36** 15002-15008 (2011).

52. Abernathy, H., Koep, E., Compson, C., Cheng, Z., & Liu, M., "Monitoring Ag-Cr Interactions in SOFC Cathodes Using Raman Spectroscopy," *Journal of Physical Chemistry C* **112** (34), 13299-13303 (2008).

53. Weber, W. H. & Merlin, R., Raman Scattering in Materials Science, New York: Springer-Heidelberg, 2000.

54. Smith, E. & Dent, G., Modern Raman Spectroscopy: A Practical Approach, Hoboken, NJ: Wiley, 2005.

55. Banares, M. A., In Situ Spectroscopy of Catalysts, USA: American Scientific Publishers, 2004.

56. Raman, C. V. & Krishnan, K. S., "A New Type of Secondary Radiation," *Nature* **121** 501-502 (1928).

57. Nagasawa, H., Mourikis, S., & Schulke, W., "X-ray Raman spectrum of Li, Be, and graphite in a high resolution inelastic synchrotron x-ray-scattering experiment," *Journal of the Physical Society of Japan* **58** (2), 710-717 (1989).

58. Nakamoto, K., Infrared and Raman Spectra of Inorganic and Coordination Compounds, New York: John Wiley & Sons, Inc., 1997.

59. Hernandez, W. Y., Laguna, O. H., Centeno, M. A., & Odriozola, J. A., "Structural and catalytic properties of lanthanide (La, Eu, Gd) doped ceria," *Journal of Solid State Chemistry* **184** (11), 3014-3020 (2011).

60. Prasad, D. H., Kim, H.-R., Park, J.-S., Son, J.-W., Kim, B.-K., Lee, H.-W., & Lee, J.-H., "Superior sinterability of nano-crystalline gadolinium doped ceria powders synthesized by co-precipitation method," *Journal of Alloys and Compounds* **495** (1), 238-241 (2010).

61. Kostic, R., Miric, M., Radic, T., Radovic, M., Gajic, R., & Popovic, Z. V., "Optical Characterization of Graphene and Highly Oriented Pyrolytic Graphite," *Acta Physica Polinica A* **116** (4), 718-721 (2009).

62. Mitchell, J. F., Argyriou, D. N., Potter, C. D., Hinks, D. G., Jorgensen, J. D., & Bader, S. D., "Structural phase diagram of $La_{1-x}Sr_xMnO_{3+\delta}$: Relationship to magnetic and transport properties," *Physical Review B* **54** (9), 6172-6183 (1996).

63. Tai, L. W., Nasrallah, M. M., Anderson, H. U., Sparlin, D. M., & Sehlin, S. R., "Structural and electrical-properties of $La_{1-x}Sr_xCo_{1-y}Fe_yO_3$," *Solid State Ionics* **76** (3-4), 273-283 (1995).

64. Varshney, D., Kumar, A., & Verma, K., "Effect of A site and B site doping on structural, thermal, and dielectric properties of $BiFeO_3$ ceramics," *Journal of Alloys and Compounds* **509** (33), 8421-8426 (2011).

65. Dresselhaus, M. S., Jorio, A., Hofmann, M., Dresselhaus, G., & Saito, R., "Perspectives on Carbon Nanotubes and Graphene Raman Spectroscopy," *Nano Letters* **10** 751-758 (2010).

66. Blinn, K. S., Abernathy, H. W., Li, X., Liu, M. F., & Liu, M., "Raman spectroscopic monitoring of carbon deposition on hydrocarbon-fed solid oxide fuel cell anodes," *Energy & Environmental Science* **5** 7913-7917 (2012).

67. Yang, H. Z., Yang, Y. Q., & Zou, S. Z., "Surface-enhanced Raman spectroscopic evidence of methanol oxidation on ruthenium electrodes," *Journal of Physical Chemistry B* **110** (35), 17296-17301 (2006).

68. Cheng, Z., Abernathy, H., & Liu, M., "Raman Spectroscopy of Nickel Sulfide Ni_3S_2," *Journal of Physical Chemistry C* **111** (49), 17997-18000 (2007).

69. Dong, J., Cheng, Z., Zha, S. W., & Liu, M. L., "Identification of nickel sulfides on Ni–YSZ cermet exposed to H_2 fuel containing H_2S using Raman spectroscopy," *Journal of Power Sources* **156** (2), 461-465 (2006).

70. Kloprogge, J. T., Wharton, D., Hickey, L., & Frost, R. L., "Infrared and Raman study of interlayer anions CO_3^{2-}, NO_3^-, SO_4^{2-}, and ClO_4^- in Mg/Al-hydrotalcite," *American Mineralogist* **87** 623-629 (2002).

71. Choi, Y. M., Abernathy, H., Chen, H.-T., Lin, M. C., & Liu, M., "Characterization of O_2-CeO_2 interactions using in situ Raman spectroscopy and first-principle calculations," *ChemPhysChem* **7** (9), 1957-1963 (2006).

72. Pushkarev, V. V., Kovalchuk, V. I., & d'Itri, J. L., "Probing defect sites on the CeO2 surface with dioxygen," *Journal of Physical Chemistry B* **108** (17), 5341-5348 (2004).

73. Blinn, K. S., Abernathy, H. W., & Liu, M. L.," *Advances in Solid Oxide Fuel Cells V* **30** 65 (2010).

74. Mizusaki, J., Tagawa, H., Saito, T., Yamamura, T., Kamitani, K., Hirano, K., Ehara, S., Takagi, T., Hikita, T., Ippommatsu, M., Nakagawa, S., & Hashimoto,

K., "Kinetic-Studies of the reaction at the Nickel Pattern Electrode on YSZ in H_2-H_2O atmospheres," *Solid State Ionics* **70** 52-58 (1994).

75. Koep, E., Compson, C., Liu, M. L., & Zhou, Z. P., "A photolithographic process for investigation of electrode reaction sites in solid oxide fuel cells," *Solid State Ionics* **176** (1-2), 1-8 (2005).

76. Chen, Y., Guan, J.-G., & Xie, H.-Q., "An efficient way to prepare silver nanorods in high concentration without adding other metal or salt," *Materials Chemistry and Physics* **134** (2-3), 686-694 (2012).

77. Hu, Y., Zhang, Q., Goebl, J., Zhang, T., & Yin, Y., "Control over the permeation of silica nanoshells by surface-protected etching with water," *Physical Chemistry Chemical Physics* **12** 11836-11842 (2010).

78. Cable, T. L. & Sofie, S. W., "A symmetrical, planar SOFC design for NASA's high specific power density requirements," *Journal of Power Sources* **174** 221-227 (2007).

79. Scherban, T., Villenueve, R., & Abello, L., "Raman scattering study of phase transitions in undoped and rare earth ion-doped $BaCeO_3$ and $SrCeO_3$," *Journal of Raman Spectroscopy* **24** 805-814 (1993).

80. Andrault, D. & Poirier, J. P., "Evolution of the distortion of under pressure: an EXAFS of $BaZrO_3$, $SrZrO_3$, and $CaGeO_3$," *Physics and Chemistry of Minerals* **18** (2), 91-105 (1991).

81. Chopelas, A., "Single-crystal Raman spectra of $YAlO_3$ and $GdAlO_3$: comparison to several orthorhombic ABO_3 pervoskites," *Physics and Chemistry of Minerals* **38** (9), 709-726 (2011).

82. Anedda, A., Carbonaro, C. M., Clemente, F., Corpino, R., & Ricci, P. C., "Raman Investigation of Surface OH-species in Porous Silica," *Journal of Physical Chemistry B* **107** (49), 13661-13664 (2003).

83. Crupi, V., Majolino, D., Migliardo, P., & Venuti, V., "Diffusive Relaxations and Vibrational Properties of Water and H-bonded Systems in Confined State by Neutrons and Light Scattering: State of the Art," *Journal of Physical Chemistry A* **104** (47), 11000-11012 (2000).

84. Lutz, H. D., "Bonding and structure of water molecules in solid hydrates - correlation of spectroscopic and structural data," *Structure and Bonding* **69** 97-125 (1988).

85. Ratajska-Gadomska, B. & Gadomski, W., "Water structure in nanopores of agarose gel by Raman spectroscopy," *Journal of Chemical Physics* **121** 12583-12588 (2004).

86. Giannici, F., Shirpour, M., Longo, A., Martorina, A., Merkle, R., & Maier, J., "Long-Range and Short-Range Structure of Proton-Conducting Y:$BaZrO_3$," *Chemistry of Materials* **23** (11), 2994-3002 (2011).

87. Atkinson, A., Barnett, S., Gorte, R. J., Irvine, J. T. S., McEvoy, A. J., Mogensen, M., Singhal, S. C., & Vohs, J., "Advance anodes for high-temperature fuel cells," *Nature Materials* **3** (1), 17-27 (2004).

88. Marina, O. A., Canfield, N. L., & Stevenson, J. W., "Thermal, electrical, and electrocatalytical properties of lanthanum-doped strontium titanate," *Solid State Ionics* **149** (1-2), 21-28 (2002).

89. Ruiz-Morales, J. C., Canales-Vazquez, J., Savaniu, C., Marrero-Lopez, D., Zhou, W., & Irvine, J. T. S., "Disruption of extended defects in solid oxide fuel cell anodes for methane oxidation," *Nature* **439** 568-571 (2006).

90. Huang, Y. H., Dass, R. I., Xing, Z. L., & Goodenough, J. B., "Double perovskites as anode materials for solid oxide fuel cells," *Science* **312** 254-257 (2006).

91. McPhee, W. A. G., Bateman, L., Koslowske, M., Slaney, M., Uzep, Z., Bentley, J., & Tao, T., "Direct JP-8 Conversion Using a Liquid Tin Anode Solid Oxide Fuel Cell (LTA-SOFC) for Military Applications," *Journal of Fuel Cell Science and Technology* **8** (4), 041007 (2011).

92. Zha, S. W., Tsang, P., Cheng, Z., & Liu, M., "Electrical properties and sulfur tolerance of $La_{0.75}Sr_{0.25}Cr_{1-x}Mn_xO_3$ under anodic conditions," *Journal of Solid State Chemistry* **178** (6), 1844-1850 (2005).

93. Zha, S. W., Cheng, Z., & Liu, M. L., "A sulfur tolerant anode for SOFCs: $Gd_2Ti_{1.4}Mo_{0.6}O_7$," *Electrochemical and Solid State Letters* **8** (8), A406-A408 (2005).

94. Ferrari, A. C. & Robertson, J., "Resonant Raman spectroscopy of disordered, amorphous, and diamondlike carbon," *Physical Review B* **64** (7), 075414 (2001).

95. Zha, S., Moore, A., Abernathy, H., & Liu, M., "GDC-Based Low-Temperature SOFCs Powered by Hydrocarbon Fuels," *Journal of The Electrochemical Society* **151** (8), A1128-A1133 (2004).

96. Sumi, H., Puenggjinda, P., Muroyama, H., Matsui, T., & Eguchi, K., "Effects of crystal Structure of yttria- and scandia-stabilized zirconia in nickel-based SOFC anodes on carbon deposition and oxidation behavior," *Journal of Power Sources* **196** (15), 6048-6054 (2011).

97. Pomfret, M. B., Marda, J., Jackson, G. S., Eichhorn, B. W., Dean, A. M., & Walker, R. A., "Hydrocarbon fuels in solid oxide fuel cells: In situ Raman studies of graphite formation and oxidation," *Journal of Physical Chemistry C* **112** 5232 (2008).

98. Pomfret, M. B., Owrutsky, J. C., & Walker, R. A., "High-temperature Raman spectroscopy of solid oxide fuel cell materials and processes," *Journal of Physical Chemistry B* **110** (35), 17305-17308 (2006).

99. Eigenbrodt, B. C., Pomfret, M. B., Steinhurst, D. A., Owrutsky, J. C., & Walker, R. A., "Direct, In Situ Optical Studies of Ni-YSZ Anodes in Solid Oxide Fuel Cells Operating with Methanol and Methane," *Journal of Physical Chemistry C* **115** 2895 (2011).

100. Li, X., Blinn, K., Fang, Y., Liu, M., Mahmoud, M. A., Cheng, S., Bottomley, L. A., El-Sayed, M., & Liu, M., "Application of surface enhanced Raman spectroscopy to the study of SOFC electrode surfaces," *Physical Chemistry Chemical Physics* **14** 5919-5923 (2012).

101. Yoshinaga, M., Koshimoto, H., Yamaji, K., Xiong, Y.-P., Brito, M. E., Horita, T., & Yokokawa, H., "Deposited carbon distributions on nickel film/oxide substrate systems," *Solid State Ionics* **192** (1), 571-575 (2010).

102. Pomfret, M. B., Steinhurst, D. A., & Owrutsky, J. C., "Methanol and Ethanol Fuels in Solid Oxide Fuel Cells: A Thermal Imaging Study of Carbon Deposition," *Energy & Fuels* **25** (6), 2633-2642 (2011).

103. Cheng, Z. & Liu, M., "Characterization of sulfur poisoning of Ni-YSZ anodes for solid oxide fuel cells using in situ Raman microspectroscopy," *Solid State Ionics* **178** (13-14), 925-935 (2007).

104. Zhang, J., Kong, C., & Young, D. J., "Surface orientation effects on initial carbon deposition and metal dusting of nickel," *Materials At High Temperatures* **26** (1), 45-55 (2009).

105. Abernathy, H. W. *Investigations of Gas/Electrode Interactions in Solid Oxide Fuel Cells Using Vibrational Spectroscopy*. Ph. D Thesis, Georgia Institute of Technology.

106. Jensen, W. B., "The Origin of the Brin Process for the Manufacture of Oxygen," *Journal of Chemical Education* **86** (11), 1266-1267 (2009).

107. Efthimiopoulos, I., Kunc, K., Karmakar, S., Syassen, K., Hanfland, M., & Vajenine, G., "Structural transformation and vibrational properties of BaO_2 at high pressures," *Physical Review B* **82** 134125 (2010).

108. Uy, D., Dubkov, A., Graham, G. W., & Weber, W. H., "UV Raman spectroscopy of adsorbed SO_x on γ–alumina and Pt/γ–alumina catalysts," *Catalysis Letters* **68** 25-32 (2000).

109. Fleischmann, M., Hendra, P. J., & McQuilla, A. J., "Raman spectra of pyridine adsorbed at a silver electrode," *Chemical Physics Letters* **26** (2), 163-166 (1974).

110. Jeanmaire, D. L. & Duyne, R. P. V., "Surface Raman Spectroelectrochemistry: 1. Heterocyclic, Aromatic, and Aliphatic Amines Adsorbed on Anodized Silver Electrode," *Journal of Electroanalytical Chemistry* **84** 1-20 (1977).

111. Albrecht, M. G. & Creighton, J. A., "Anomalously intense Raman spectra of pyridine at a silver electrode," *Journal of the American Chemical Society* **99** 5215-5217 (1977).

112. Kneipp, K., Kneipp, H., Itzkan, I., Dasari, R. R., & Feld, M. S., "Ultrasensitive Chemical Analysis by Raman Spectroscopy," *Chemical Reviews* **99** 2957-2975 (1999).

113. Moskovits, M., "Surface-enhanced Raman spectroscopy: a brief retrospective," *Journal of Raman Spectroscopy* **36** 485-496 (2005).

114. Lee, S. J., Guan, Z., Xu, H., & Moskovits, M., "Surface-Enhanced Raman Spectrocopy and Nanogeometry: The Plasmonic Origin of SERS," *Journal of Physical Chemistry C* **111** (49), 17985-17988 (2007).

115. Liu, Y. C., Hwang, B. J., & Jian, W. J., "Effect of preparation conditions for roughening gold substrate by oxygen-reduction cycle on the surface-enhanced Raman spectroscopy of polypyrrole," *Materials Chemistry and Physics* **73** 129-134 (2002).

116. Prokoprec, V., Cejkova, J., Matekja, P., & Hasal, P., "Preparation of SERS-active substrates with large surface area for Raman spectral mapping and testing of their surface nanostructure," *Surface and Interface Analysis* **40** 601-607 (2008).

117. Emory, S. & Nie, S., "Screening and enrichment of metal nanoparticles with novel optical properties," *Journal of Physical Chemistry B* **102** 493-497 (1998).

118. Hou, X. M. & Fang, Y., "Surface-enhanced Raman scattering of single-walled carbon nanotubes on modified silver electrode," *Spectrochimica Act Part A - Molecular and Biomolecular Spectroscopy* **69** (4), 1140-1145 (2008).

119. Fang, Y., Li, X., Blinn, K., Mahmoud, M., & Liu, M. L., "Resonant surface enhancement of Raman scattering of Ag nanoparticles on silicon substrates fabricated by dc sputtering," *Journal of Vacuum Science and Technology A* **30** (5), 050606 (2012).

120. Williams, C., Chen, E., Takoudis, C., & Weaver, M., "Reduction kinetics of surface rhodium oxide by hydrogen and carbon monoxide at ambient gas pressures as probed by transient surface-enhanced Raman spectroscopy," *Journal of Physical Chemistry B* **102** 4785-4794 (1998).

121. Itoh, T., Maeda, T., & Kasuya, A., "In situ surface-enhanced Raman scattering spectroelectrochemistry of oxygen species," *Faraday Discussions* **132** (2006).

122. Itoh, T., Abe, K., Dokko, K., Mohamedi, M., Uchida, I., & Kasuya, A., "In situ Raman spectroelectrochemistry of oxygen species on gold electrodes in high temperature molten carbonate melts," *Journal of The Electrochemical Society* **151** A2042-A2046 (2004).

123. Li, J. F., Huang, Y. F., Ding, Y., Yang, Z. L., Li, S. B., Zhou, X. S., Fan, F. R., Zhang, W., Zhou, Z. Y., Wu, D. Y., Ren, B., Wang, Z. L., & Tian, Z. Q., "Shell-isolated nanoparticle-enhanced Raman spectroscopy," *Nature Chemistry* **464** 392-395 (2010).

124. Shantil, M., Thomas, R., Swathi, R. S., & Thomas, K. G., "Ag@SiO_2 Core-Shell Nanostructures: Distance-Dependent Plasmon Coupling and SERS Investigation," *Journal of Physical Chemistry Letters* **3** 1459-1464 (2012).

125. Krasser, W., Fadini, A., Rozemuller, E., & Renouprez, A. J., "Raman spectra from ethylene and deuterated ethylene chemisorbed on a silica-supported Ni catalyst," *Journal of Molecular Structure* **66** 135-148 (1980).

126. Atamas, N. A., Yaremko, A. M., Seeger, T., Leipertz, A., Bienko, A., Latajka, Z., Ratajczak, H., & Barnes, A. J., "A study of the Raman spectra of alkanes in the Fermi-resonance region," *Journal of Molecular Structure* **708** (1-3), 189-195 (2004).

127. Cable, T. L., Setlock, J. A., Farmer, S. C., & Eckel, A. J., "Regenerative Performance of the NASA Symmetrical Solid Oxidel Fuel Cell Design," *International Journal of Applied Ceramic Technology* **8** (1), 1-12 (2011).

128. Badwal, S. P. S., Deller, R., Foger, K., Ramprakash, Y., & Zhang, J. P., "Interaction between chromia forming alloy interconnects and air electrode of solid oxide fuel cells," *Solid State Ionics* **99** (3-4), 297-310 (1997).

129. Jiang, S. P., Zhang, J. P., & Zheng, X. G., "A comparative investigation of chromium deposition at air electrodes of solid oxide fuel cells," *Journal of the European Ceramic Society* **22** (3), 361-373 (2002).

130. Wang, Y., Latz, J., Dahl, R., Pasel, J., & Peters, R., "Liquid phase desulfurization of jet fuel by a combined pervaporation and adsorption process," *Fuel Processing Technology* **90** 458-464 (2009).

131. Latz, J., Peters, R., Pasel, J., Datsevich, L., & Jess, A., "Hydrodesulfurization of jet fuel by pre-saturated one-liquid-flow technology for mobile fuel cell applications," *Chemical Engineering Science* **64** (2), 288-293 (2008).

132. Flytzani-Stephanopoulos, M., Sakbodin, M., & Wang, Z., "Regenerative adsorption and removal of H_2S from hot fuel streams by rare earth oxides," *Science* **312** 1508-1510 (2006).

133. Oniyama, E., Wahlbeck, P. G., Peterson, D. E., Coulter, J. Y., & Peterson, E. J., "Phase diagram for 1/2 Yb_2O_3-BaO-CuO," *Physica C* **288** 151-157 (1997).

134. Wong-Ng, W., Yang, Z., & Cook, L. P., "Subsolidus phase relationships of the BaO-R_2O_3-CuO_z (R = Tm and Yb) systems under carbonate-free conditions at pO_2 = 100 kPa and T = 750^{O}C and 810^{O}C," *Journal of Alloys and Compounds* **437** (1-2), 58-63 (2007).

135. Mullerbuschbaum, M. & Schrandt, O., "Crystal-structure of $Ba_3Ln_4O_9$ (Ln-equivalent-to-Dy, Er, Y/Yb)," *Journal of Alloys and Compounds* **191** (1), 151-154 (1993).

136. Jiao, J., Liu, X., Gao, W., Wang, C., Feng, H., Zhao, X., & Chen, L., "Two-step synthesis of witherite and tuning of morphology," *Materials Research Bulletin* **45** (2), 181-185 (2010).

137. Hussein, G. A. M. & Balboul, B. A. A., "Ytterbium oxide from different precursors: formation and characterization: Thermoanalytical studies," *Powder Technology* **103** (2), 156-164 (1999).

138. Chen, C., Liu, M., Bai, Y., Yang, L., Xie, E., & Liu, M., "Anode-supported tubular SOFCs based on $BaZr_{0.1}Ce_{0.7}Y_{0.1}Yb_{0.1}O_{3-\delta}$ electrolyte fabricated by dip coating," *Electrochemistry Communications* **13** 615-618 (2011).

139. Osman, N., Jani, A. M., & Talib, I. A., "Synthesis of Yb-doped Ba(Ce,Zr)O-3 ceramic powders by sol-gel method," *Ionics* **12** (6), 379-384 (2006).

140. Ahmed, I., Eriksson, S.-G., Ahlberg, E., Knee, C. S., Gotlind, H., Johansson, L.-G., Karlsson, M., Matic, A., & Borjesson, L., "Structural study and proton conductivity of Yb-doped $BaZrO_3$," *Solid State Ionics* **178** (7-10), 515-520 (2007).

141. Singh, A. & Hill, J., "Carbon tolerance, electrochemical performance, and stability of solid oxide fuel cells with Ni/yttria stabilized zirconia anodes impregnated with Sn and operated with methane," *Journal of Power Sources* **214** 185-194 (2012).

142. Myung, J., Ko, H. J., Lee, J.-J., & Hyun, S.-H., "Optimization of Flow Rate for Improving Performance and Stability of Ni-YSZ based Solid Oxide Fuel Cell Using CH_4 Fuel," *International Journal of Electrochemical Science* **6** 1617-1629 (2011).